Estimates of Land Ice Changes from Sea Level and Gravity Observations

Estimates of Land Ice Changes from Sea Level and Gravity Observations

A dissertation presented

by

Eric Morrow

to

The Department of Earth and Planetary Sciences

in partial fulfillment of the requirements

for the degree of

Doctor of Philosophy

in the subject of

Earth and Planetary Sciences

Harvard University

Cambridge, Massachusetts

April 2014

Dissertation Advisor: Professor Jerry X. Mitrovica Eric Morrow

Estimates of Land Ice Changes from Sea Level and Gravity Observations

Abstract

Understanding how global ice volume on the Earth has changed is of significant importance to improving our understanding of the climate system. Fortunately, the geographically unique perturbations in sea level that result from rapid changes in the mass of, otherwise difficult to measure, land-ice reservoirs can be used to infer the sources and magnitude of melt water. We explore the history of land-ice mass changes through the effect that these mass fluxes have had on both global and regional gravity and sea-level fields.

We use the time-dependent response of the Earth's geopotential field to changes in mass distribution at the surface and within the Earth to identify an enigma in the generally assumed history of the planet's degree-2 zonal harmonic over the past 25 Myr. The solution to this problem will have implications for the timing of global ice volume changes as they are determined from isotopic analysis of sedimentary cores.

We describe the advantages of considering the degree-4 zonal harmonic of the geopotential, relative to the degree-2 harmonic, when deriving inferences of net polar ice mass change in the latter part of the 20th century. We then use the observed constraint on the degree-4 harmonic to provide an independent estimate of net polar ice-mass change over the past 20 years.

Estimates of mountain glacier and polar ice sheet mass changes have become more

tractable since the launch of the Gravity Recovery and Climate Experiment (GRACE). However, we demonstrate that estimates of ice mass changes using data from GRACE may be overestimating the mass flux by neglecting the impact of the sea-level response on the ice melt and its implications on the sampled gravity field.

Finally, we develop and apply a Gaussian Process regression methodology to estimate mass fluxes from meltwater sources over the 20th century using tide gauge records. By using the equivalent eustatic sea-level changes associated with melting events, rather than regional averages of tide gauge records, we infer a global mean sea-level rate that that is $\sim$24% lower than current estimates.

Contents

List of Figures

List of Tables

Acknowledgements

I would like to thank my advisor, Jerry Mitrovica, for his mentorship, support and encouragement. The years under his leadership and advisement have fostered personal growth within the best possible environment that I could have wanted. I would also like to thank my committee members, Rick O'Connell, Dave Johnston, and especially Peter Huybers, for many years of thoughtful discussion and guidance. I thank also the Mitrovica group and those associated (Carling Hay, Erik Chan, Natalya Gomez, Jacky Austermann, Harriet Lau, Ken Ferrier, Glenn Sterenborg and JC Creveling) for many years of a constructive and fun environment. And within that group I want to expressly thank Carling for being the best and brightest collaborator and friend for which one could ask. Thanks also to Bob Kopp who has provided invaluable guidance, support and feedback for significant elements of this work. And finally, I would like to thank my wife, Carolyn, and my friends and family for all of their support and encouragement.

Chapter 1

Introduction

Understanding how global ice volume on the Earth has changed and is continuing to change is of significant importance to improving our understanding of the greater climate system. However, estimating mass changes of the Earth's land-ice reservoirs is challenging. On modern time scales, the polar ice sheets and most mountain glaciers are both remote and large in areal extent, and changes in their volume are difficult to constrain through direct observation. Fortunately, perturbations in sea level can be used to infer ice mass changes (e.g. Mitrovica et al., 2001; Plag and Juttner, 2001; Hay et al., 2012). Indeed, the unique, and geographically-variable spatial patterns, or 'fingerprints', in sea level that result from rapid changes in the mass of the land-ice reservoirs provide a foundation for robust statistical estimations of the magnitude and sources of melt water. Moreover, even when not acting as a basis for the inference of ice mass changes, understanding the implications of the fingerprints in direct, local observations of ice mass change, such as those obtained from recent satellite programs like the Gravity Recovery and Climate Experiment (GRACE) (Tapley et al., 2004) is important for avoiding biases in the estimates.

On longer time scales of millions of years, the viscous isostatic adjustments associated

with the growth and melt of land-ice during the ice age cycles perturb select orbital frequencies of the planet and hence the timing of glaciation/deglaciation cycles. However, on such long time scales mantle convection is another geodynamic process that can alter select orbital frequencies of the planet and hence the timing estimates. Consequently, it is important to understand the implications that both of these processes have on inferences of either the timing of the glaciation cycles or on the rheological structure of the planet.

This thesis explores the history of land-ice mass changes through the effect that these mass fluxes have had on both global and regional gravity and relative sea-level fields. The forthcoming chapters are arranged such that they consider the Earth's response to loading changes from low-degree spherical harmonics (i.e. low spatial resolution) to increasingly higher-degree harmonics.

Chapter 2 presents an overview of the physics of the sea-level theory that underlies the subsequent chapters. The chapter follows the derivation of the general sea-level equation with a discussion of the physics that governs how sea level has changed on time scales that range from the past 100 years through the past millions of years.

Chapter 3 uses the time-dependent response of the Earth's geopotential field to changes in mass distribution at the surface and within the Earth to identify an enigma in the generally assumed history of the planet's spherical harmonic degree-2, order-0 shape. The solution to this problem will have implications for the timing of global ice volume changes as they are determined from isotopic analysis of sedimentary cores. This chapter was published as Morrow et al. (2012).

In addition to the usefulness of the degree-2 coefficient of the gravity field in specifying the

timing of ice volume changes over the past several millions of years, satellite-derived estimates of the same parameter have been used to estimate net polar ice-mass changes over the last 30 years. However, as described in Chapter 3, changes in the degree-2 harmonic can be driven by processes unrelated to ice-mass change. Chapter 4 describes the advantages of considering the degree-4 spherical harmonic of the geopotential relative to the degree-2 harmonic, then uses the observed constraint on the degree-4 harmonic to provide an independent estimate of net polar ice-mass change over the past 20 years. This chapter was published as Morrow et al. (2013).

With the higher spatial and temporal resolution provided by GRACE since 2002, estimates of mountain glacier and polar ice sheet mass changes have become more tractable. However, as demonstrated in Chapter 5, these estimates may be overestimating the mass flux as they neglect the impact of the sea-level response to the ice melt and its implications on the sampled gravity field. Much of this chapter was published in an alternate form in Sterenborg et al. (2013).

Chapter 6 develops and then uses a methodology based on Gaussian Process (GP) regression to estimate mass fluxes from meltwater sources over the 20th century using the tide gauge observations cataloged within the Permanent Service for Mean Sea Level (Holgate et al., 2013) (PSMSL) database. The GP approach possesses several characteristics that make it suited for estimates of sea-level budgets. Firstly, it is non-parametric, meaning that it does not require the assumption of an a priori function form for the mass change histories. Secondly, it is a Bayesian approach which naturally accommodates the incompleteness of the tide gauge record. In addition to estimates of melt contributions to 20th century sea-level

change, the approach also generates a new estimate of global mean sea level.

Finally, Chapter 7 presents an overview of the main conclusions of each of the preceding chapters and describes potential avenues of future research.

Chapter 2

Foundations of Sea-Level Theory

Abstract

In this section we provide a summary of 20th century sea-level change and describe the physics behind the unique spatial patterns of sea level that arise from melting land ice. This summary serves as a foundation for the remainder of this thesis.

2.1 Introduction

Sea-level changes occur due to either changes the volume of water in the oceans or changes in the volume of the ocean basins themselves. These changes occur on a continuum of time scales that spans seconds to hundreds of millions of years. On million-year time scales, ocean basin volume changes are a significant contributor to sea level variability. The motion of tectonic plates changes the geometry of the ocean basins in a few ways. Variability in sea floor spreading rates alter the topography of the ocean floor (e.g. Hays and Pitman, 1973). Variations in land erosion and its subsequent sedimentary transport into the oceans also change this topography (Dalca et al., 2013). On a comparable timescale, continental collisions can change the basin volume by compressing the areal extent of continents (e.g.

van Andel, 1994). Another significant contributor to sea level variability is the change in topography driven mantle convection, termed dynamic topography (e.g. Mitrovica et al., 1989; Gurnis, 1990; Moucha et al., 2008; Spasojevic and Gurnis, 2012), which occur on million-year time scales and have amplitudes of tens-of-meters (e.g. Rowley et al., 2013).

On intermediate timescales of thousands to hundreds of thousands of years, variability in the volume of land ice results in changes in sea level on the order of 100 meters. This change in mass distribution results in a viscoelastic response of the solid Earth and an associated change in the sea surface as the planet isostatically compensates the loading/unloading cycles. The glacial isostatic adjustment (GIA) of the planet in response to the Late Pleistocene produces a spatial pattern of sea-level change that varies systematically from the near-field to the far-field centers of ancient ice cover (e.g. Clark et al., 1978; Mitrovica and Peltier, 1991; Milne and Mitrovica, 2008).

At the shortest timescales of less than a few hundred years, a number of factors influence sea level. In addition to on-going GIA, one category of drivers are classified as so-called "dynamic effects", which include ocean-atmosphere interactions, tides, ocean currents and circulation changes, as well as the density variations due to salinity and temperature heterogeneity. Additionally, there are the "static equilibrium effects" which refer to sea-level changes due to ice mass changes and the associated gravitational, deformational and rotational effects on the solid Earth. One goal of this thesis is to use the unique spatial and temporal patterns of sea-level change associated with each of these processes, in combination with the outputs of global ocean models, to estimate the main contributors to global sea level over the 20th century.

For the last few centuries, an instrumental record of sea level has been established through the use of tide gauges, which are devices affixed to the solid Earth that measure the height of the sea level relative to the sea floor. The Proudman Laboratory at the University of Bristol maintains the Permanent Service for Mean Sea Level (PSMSL) (www.psmsl.org), a database of the temporal records for more than 2000 tide gauges. Observations from the tide gauges are divided into two subsets: the metric records contain the raw observations in their individual reference frames as provided to the PSMSL; and the revised local reference (RLR), a smaller subset than the complete database that includes records that have been reduced to a common height datum. For studies of global sea level, the latter RLR subset of 1166 tide gauge sites is most useful since the common reference frame allows for a direct comparison between the tide gauge records.

Figure 2.1 shows the spatial distribution of the 596 tide gauges represented in the PSMSL RLR database that have at least 20 years of data present in the last 50 years. The color of each site indicates the variance of the tide gauge data computed from the annual records using all available data from 1807 to 2000. The largest variability is found in the closed basins of the Baltic and Black Seas and along the Russian Arctic Ocean coast.

Figure 2.2 shows the annual availability of tide gauges divided into the five regions identified in Figure 2.1. There is a significant sampling bias, with most tide gauges located in the northern hemisphere. In addition to the spatial bias, there is a significant bias in the duration of the records with the majority of the longest records located within Region 2. Specifically, the bulk of the longest records are located along the coasts of Scandinavia; there are also exceptionally long records located at Brest, France, Liverpool, UK, New York, USA,

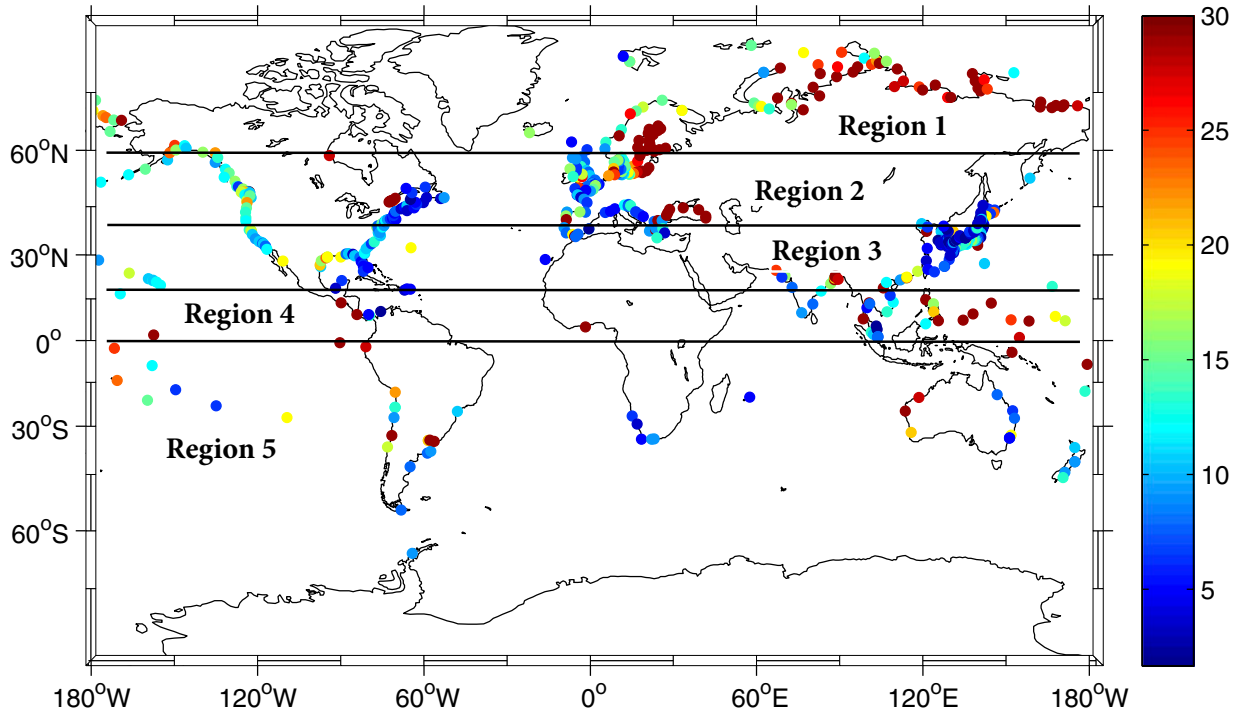

Figure 2.1: Variance of detrended heights at 596 tide gauge sites from the PSMSL RLR database (Hay et al., 2012).

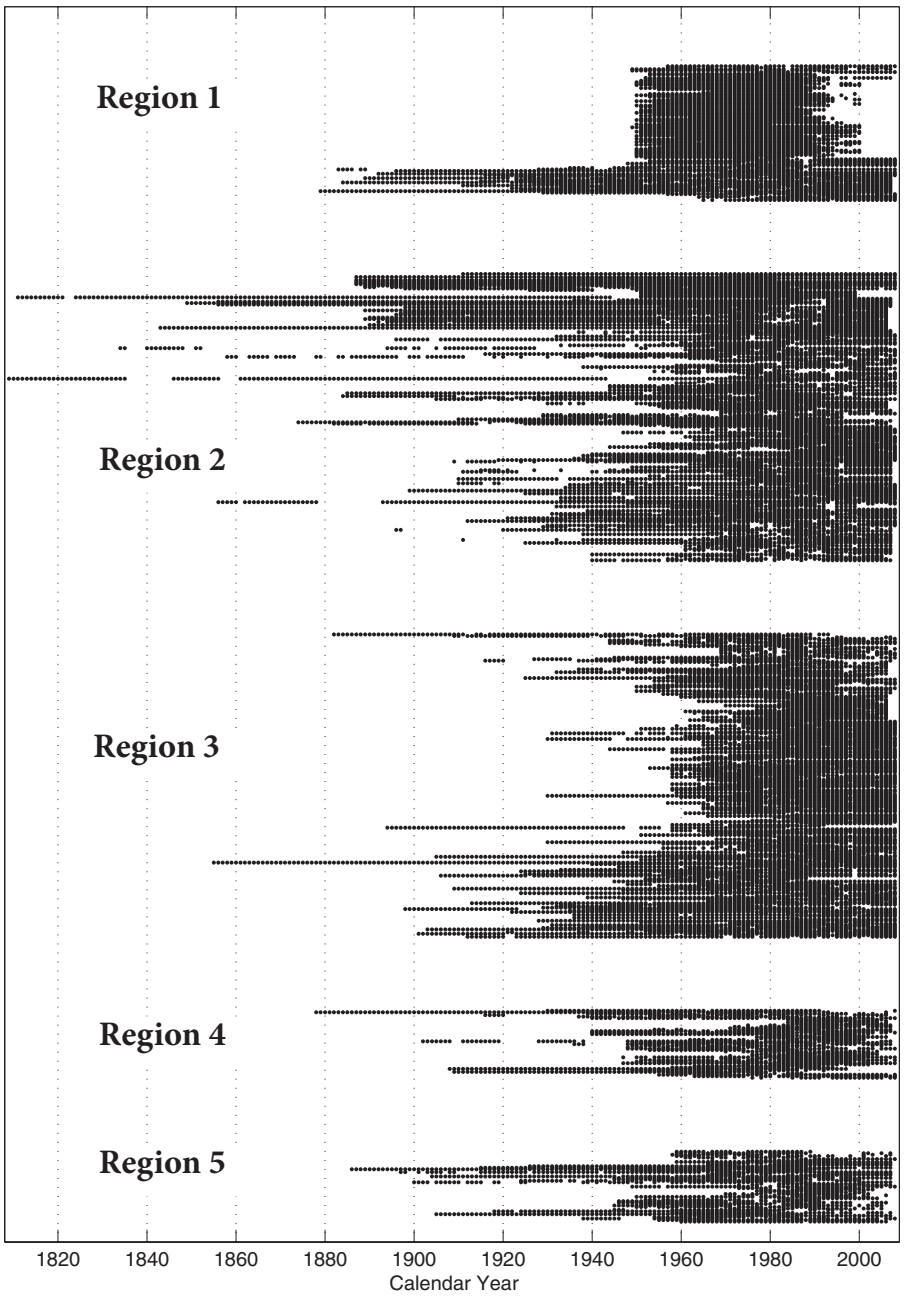

Figure 2.2: Temporal availability of the 596 tide gauges shown in Figure 2.1 subdivided by geographic region. The regions are specified in Figure 2.1

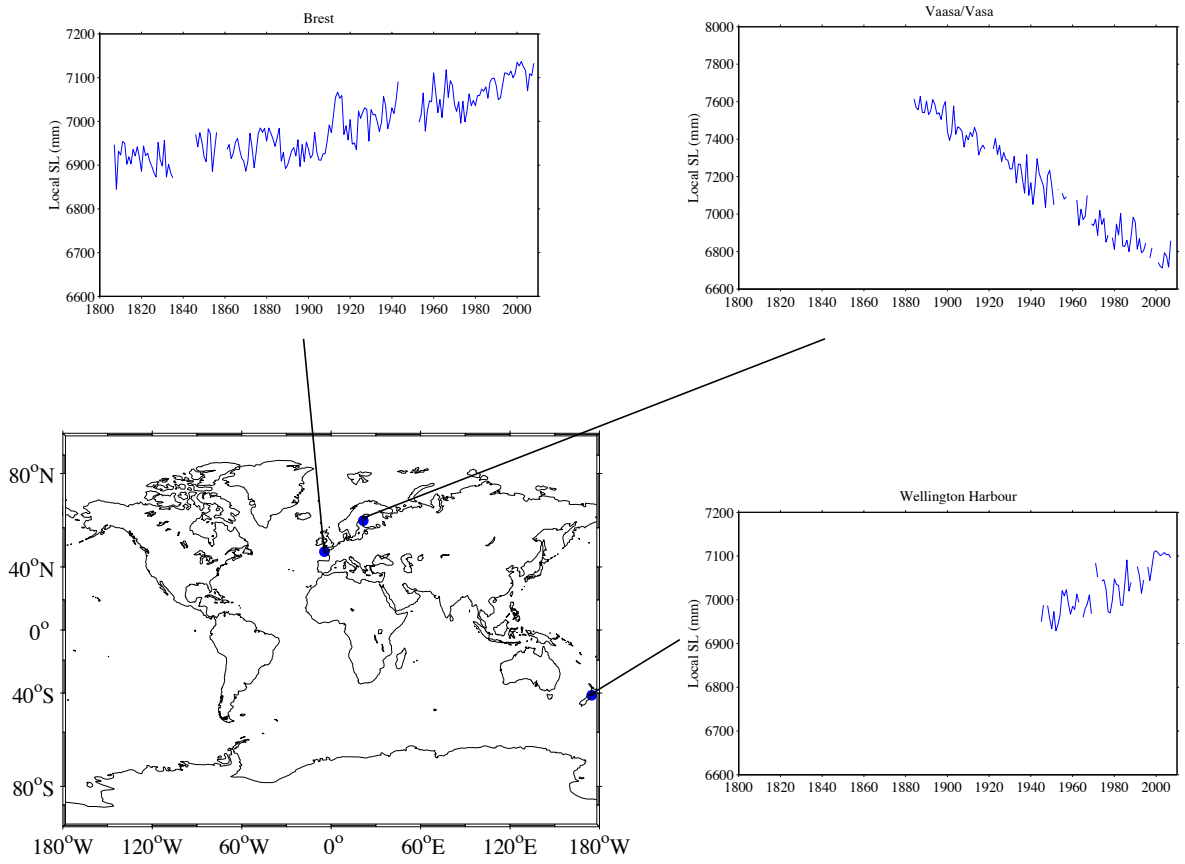

Figure 2.3: Local relative sea level recorded at thee tide gauge sites: Brest, France; Vaasa, Finland; and Wellington Harbour, New Zealand.

and San Francisco, USA.

In addition to variation in the duration, many of the records possess data gaps after the initiation of the observations. In particular, Figure 2.2 shows that the majority of tide gauges located within Region 1 terminate between 1990 and 2000. Most of these records are located along the Russian Arctic coast, and the abrupt termination of these records has implications on the resolvability of melt contributions from the Northern Russian glaciers.

As an example of individual records, Figure 2.3 shows the annual time series from three

tide gauge sites: Wellington Harbour, NZ; Brest, France; and Vaasa, Finland. The significantly different trends and variability in each of these spatially separated records highlights the complexity of sea-level changes and the different constituents that drive the changes. For example, the record at Brest shows a positive trend in the sea level of ~ 1 mm/yr that is the result of both subsidence of the peripheral bulge from the former Fennoscandian ice sheet and ongoing melting of land ice over the 20th century (Mitrovica et al., 2001). In contrast, Vaasa, which is located in a region formerly covered by the Fennoscandian ice sheet is a experiencing significant sea level fall associated with ongoing crustal uplift due to GIA. Wellington Harbour, which lies in the far-field of the late Pleistocene ice sheets, is experiencing a positive trend in sea level that may be caused by a combination of ongoing GIA effects, land-ice melt contributions and ocean dynamic effects.

Despite the regional variability of sea level, estimates of global mean sea level (GMSL) are often used as a metric to describe the trends in sea level. However, differences in the data selection and the method of computing GMSL should be considered when evaluating results described in the literature. The first, and most common approach to computing GMSL is to use a limited number of tide gauge sites that meet criteria based on record duration and continuity, consistency between neighboring sites and distance from active margins or other tectonically active regions (e.g. Peltier and Tushingham, 1989; Douglas, 1991, 1997; Holgate and Woodworth, 2004). A second approach combines regional means of larger subsets of tide gauges (e.g. Jevrejeva et al., 2008). A third method computes global reconstructions of sea level using the spatial variability estimated using altimetry observations with the temporal variability and extent provided by tide gauge records (Church and White, 2006;

Church et al., 2011; Church and White, 2011). All of these approaches yield estimates of the GIA-corrected trend in GMSL similar to the rate of 1.7 ± 0.2 mm/yr from 1900 to 2009 computed by Church and White (2011). From 1993 to 2009 this trend has been estimated to have increased to 2.8 ± 0.8 mm/yr using tide gauges and 3.2 ± 0.4 mm/yr with altimetry data (Church and White, 2011).

The principal causes of GIA-corrected sea-level trends in over the 20th century are the thermal expansion of the oceans due to increased heat content and the addition of land-based ice melt into the oceans (Cazenave and Llovel, 2010). Estimates of ocean heat content have been made since the 1960s using bathythermograph and conductivity measurements. The trend in GMSL due to thermometric contributions over the period 1955 - 1995 has been estimated to be 0.40 ± 0.09 mm/yr using five-year mean temperature data down to 3000 m depth in the oceans (Antonov et al., 2005). The trend from thermometric contributions to an ocean depth of 700 m over the period 1955 to 2003 has been estimated as 0.33 ± 0.07 mm/yr using the annual mean temperature data of Levitus et al. (2009) and 0.36 ± 0.12 mm/yr using the monthly ocean temperature data of Ishii et al. (2006) (Antonov et al., 2005). In the decade of 1993 - 2003, this contribution is estimated to have increased to between $1.2 - 1.8$ mm/yr (e.g. Antonov et al., 2005; Lombard et al., 2005; Ishii et al., 2006; Ishii and Kimoto, 2009).

Since thermometric contributions are thought to contribute $\sim 25\%$ of the sea-level trend over the past century (and up to $\sim 55\%$ in the last decade of the 20th century), changes in the mass of polar ice sheets and mountain glaciers account for $\sim 75\%$ of the century-scale trend (and $\sim 45\%$ of the trend in the last decade of the century). Mass balance estimates of

glacier melt (excluding the Greenland and Antarctic periphery glaciers) indicate that they contributed 0.33 ± 0.17 mm/yr over the time period 1961 - 1990 and 0.77 ± 0.26 mm/yr from 1991 - 2004 (Kaser et al., 2006). Estimates of Greenland and Antarctic Ice Sheet melt have each ice sheet contributing 0.05 ± 0.12 mm/yr and 0.14 ± 0.41 mm/yr, respectively, from 1961 - 2003. From 1993 to 2003 these rates increased to 0.21 ± 0.07 mm/yr and 0.21 ± 0.35 mm/yr, for the Greenland and Antarctic Ice Sheets respectively (Bindoff et al., 2007).

Changes in the mass of land ice and the complementary water load deform the Earth and perturb its gravitational field and rotational state. This generates a geographically variable response that can be predicted given the structure of the Earth and the geometry of the load change. Specifically, a rapidly melting ice sheet or glacier produces a unique and highly non-uniform pattern of sea level change, termed a "fingerprint" (e.g. Woodward, 1888; Clark and Lingle, 1977; Conrad and Hager, 1997; Mitrovica et al., 2001; Tamisiea et al., 2001). Sea level within the near-field of the melting ice will fall because of an uplift of the lithosphere due to the unloading and a decrease in the gravitational pull of the now smaller ice mass on the surrounding ocean. This fall can be up to an order of magnitude larger than the rise that would be expected if the melt water were uniformly distributed over the oceans. In the far-field of the ice complex, sea level will generally rise with increasing distance from the melt and can reach a magnitude $\sim 30\%$ larger than the uniformly-distributed equivalent (Mitrovica et al., 2011). These distinct fingerprints of melt can be used as basis functions in inferences of melt contributions from individual sources (e.g. Mitrovica et al., 2001; Plag and Juttner, 2001; Hay et al., 2012).

The following section outlines the derivation of the so-called sea-level equation that can

be used to predict sea-level changes associated with the melting of grounded ice on time scales associated with both the ongoing GIA response from the melting of the Late Pleistocene ice sheets and the more recent signal from anthropogenic climate change.

2.2 The Sea Level Equation

Relative sea level (SL) is defined as the difference between the height of the sea surface equipotential, G, and the radial position of the solid Earth surface, R:

$$SL(\theta, \psi, t) = G(\theta, \psi, t) - R(\theta, \psi, t) \tag{2.1}$$

where θ and ψ are the colatitude and longitude, respectively, and t is time. For clarity, in the following derivations the spatial dependence is made implicit and the spatial geometry of sea level is specified globally, unless otherwise noted.

We define topography (T) as the negative of SL:

$$T(t) = -SL(t) \tag{2.2}$$

In contrast to global SL, the ocean height, S, is only defined over the oceans. S can determined by projecting SL onto the ocean geometry using the so-called ocean function, $C(t)$:

$$S(t) = SL(t)C(t) \tag{2.3}$$

where

$$C(t) = \begin{cases} 1, & \text{if } SL(t) > 0 \text{ and there is no grounded ice} \\ 0, & \text{otherwise} \end{cases} \tag{2.4}$$

The global sea level, SL, may be computed as a perturbation from its initial value at time t_0:

$$SL(t_i) = SL(t_0) + \Delta SL(t_i) \tag{2.5}$$

where $\Delta SL(t_i)$ represents the change in SL from t_0 to t_i. R and G may be similarly defined such that the change in SL can be written as:

$$\Delta SL(t_i) = \Delta G(t_i) - \Delta R(t_i) \tag{2.6}$$

The ocean height, S, can also be expressed in a form similar to Equation 2.5, although in this case the perturbation to S includes a term associated with the migration of shorelines:

$$\begin{aligned} \Delta S(t_i) &= SL(t_i)C(t_i) - SL(t_0)C(t_0) \\ &= \Delta SL(t_i)C(t_i) - T(t_0)[C(t_i) - C(t_0)] \end{aligned} \tag{2.7}$$

Changes in the sea surface height, ΔG, can be decomposed into two terms: the geographically-variable perturbation to the equipotential surface, denoted as $\Delta\mathcal{G}$; and the uniform shift in the height of the equipotential upon which the sea-surface lies, written as $\frac{\Delta\Phi}{g}$. In particular:

$$\Delta G(t_i) = \Delta\mathcal{G}(t_i) + \frac{\Delta\Phi(t_i)}{g} \tag{2.8}$$

where g is the local surface gravitational acceleration and using the terminology of geodesy, $\Delta\mathcal{G}$ is the perturbation to the geoid height.

Combining Equation 2.8 with Equation 2.6, the change in SL can be rewritten as:

$$\Delta SL(t_i) = \Delta\mathcal{SL}(t_i) + \frac{\Delta\Phi(t_i)}{g} \tag{2.9}$$

where $\Delta\mathcal{SL}(t_i)$ represents changes in the geographically-variable component of SL:

$$\Delta\mathcal{SL}(t_i) = \Delta\mathcal{G}(t_i) - \Delta R(t_i) \tag{2.10}$$

Changes in $\mathcal{SL}$ are due to changes in the height of both the grounded ice load, ΔI, and the ocean load, ΔS, as well as perturbations to the angular velocity vector of the Earth, Δw (Milne and Mitrovica, 1998). Specifying these dependencies in Equation 2.10, and using Equation 2.7, yields the generalized sea-level equation:

$$\Delta S(t_i) = [\Delta\mathcal{SL}(\Delta I, \Delta S, \Delta w, t_i) + \frac{\Delta\Phi(t_i)}{g}]C(t_i) - T(t_0)[C(t_i) - C(t_0)] \tag{2.11}$$

The uniform shift in the equipotential, $\Delta\Phi(t_i)$, can be explicitly described by invoking conservation of mass in the surface load:

$$\rho_w \iint_\Omega \Delta S(t_i) d\Omega + \rho_I \iint_\Omega \Delta I(t_i) d\Omega = 0 \tag{2.12}$$

where ρ_w and ρ_I are the densities of water and ice, respectively, and the symbol Ω is the

solid angle $d\Omega = \sin(\theta)d\theta d\phi$. Integrating the change in ocean height (Equation 2.11) and using the conservation law (Equation 2.12), yields an expression for the uniform shift in the sea surface:

$$\begin{aligned}\frac{\Delta\Phi(t_i)}{g} = -\frac{1}{A(t_i)}\frac{\rho_I}{\rho_w}\iint_\Omega \Delta I(t_i)d\Omega - \frac{1}{A(t_i)}\iint_\Omega \Delta\mathcal{SL}(\Delta I, \Delta S, \Delta w, t_i)C(t_i)d\Omega \\ + \frac{1}{A(t_i)}\iint_\Omega T(t_i)[C(t_i) - C(t_0)]d\Omega\end{aligned} \tag{2.13}$$

where $A(t_i)$ is the area of the ocean, defined as:

$$A(t_i) = \iint_\Omega C(t_i)d\Omega \tag{2.14}$$

A useful concept when discussing ice sheet and glacier melt is that of eustatic sea level change (ESL) which is defined as the change in sea level on a rigid Earth due solely to the addition of water from melting grounded ice into the ocean basins, neglecting the gravitational and rotational effects that accompany the load redistribution. This relation can be found by setting $\Delta\mathcal{SL} = 0$ in Equation 2.11:

$$\Delta S_{ESL}(t_i) = \frac{\Delta\Phi(t_i)}{g}C(t_i) - T(t_0)[C(t_i) - C(t_0)] \tag{2.15}$$

with,

$$\frac{\Delta\Phi(t_i)}{g} = -\frac{1}{A(t_i)}\frac{\rho_I}{\rho_w}\iint_\Omega \Delta I(t_i)d\Omega + \frac{1}{A(t_i)}\iint_\Omega T(t_i)[C(t_i) - C(t_0)]d\Omega \tag{2.16}$$

2.2.1 Spectral form of the Sea Level Equation for a Non-Rotating Earth

For the general case of a 3-D viscoelastic Earth model, the perturbed global sea level, $\Delta\mathcal{SL}$, required in the generalized sea level equation (Equation 2.11) is solved using finite element codes (e.g. Latychev et al., 2005). This solution methodology is required for investigating the effects of lithospheric and upper mantle structure on ice-age sea-level changes (e.g. Latychev et al., 2005; Kendall et al., 2006; Austermann et al., 2013). However, if one assumes a spherically-symmetric, viscoelastic Earth with a rheology only specified as a function of depth, then the solution of the sea-level equation is traditionally found using viscoelastic Love number theory (Peltier, 1974). In this section we outline the latter approach for the case of a non-rotating Earth (i.e., the Δw dependence in Equation 2.11 is dropped).

The Love numbers are coefficients of Legendre polynomial expansions of the impulse response of a linear viscoelastic Earth as a function of spherical harmonic degree. The $k_l(t)$ and $h_l(t)$ Love numbers are the coefficients in expansions for the perturbation to the geopotential and radial displacement response, respectively, where l is the spherical harmonic degree. These have the form:

$$k_l(t) = {k_l}^E \delta(t) + \sum_{j=1}^{K} r_j'^l e^{-s_j^l t} \tag{2.17}$$

$$h_l(t) = {h_l}^E \delta(t) + \sum_{j=1}^{K} r_j^l e^{-s_j^l t} \tag{2.18}$$

where ${k_l}^E$ and ${h_l}^E$ are the elastic Love numbers and $\delta(t)$ is the Dirac delta function. The parameters r_j^l and $r_j'^l$ are the amplitudes of the non-elastic component of the jth normal

mode response to the forcing, with the associated decay time s_j^l. The first term in both equations represents the instantaneous elastic response to the forcing, while the second term is the non-elastic response. The viscoelastic structure of the Earth model is encapsulated in these response coefficients.

For a spherically symmetric Earth model, the response to a loading is only dependent on the angular distance between the load and the point of observation. Thus, this response can be computed as a space-time convolution of the load with the appropriate Green's function. The Green's function for the radial displacement response is:

$$\Gamma(\gamma, t) = \frac{a}{M_e} \sum_{l=1}^{\infty} \left[{h_l}^E \delta(t) + \sum_{j=1}^{K} r_j^l e^{-s_j^l t} \right] P_l(cos(\gamma)) \tag{2.19}$$

where a is the radius of the Earth, M_e is the mass of the Earth, P_l are the unnormalized Legendre polynomials, and γ is the angular distance between the observation point and the location of the impulse forcing. Similarly, the Green's function for the perturbation to the geopotential is:

$$\phi(\gamma, t) = \frac{ag}{M_e} \sum_{l=1}^{\infty} \left[\delta(t) + {k_l}^E \delta(t) + \sum_{j=1}^{K} r_j^{\prime l} e^{-s_j^l t} \right] P_l(cos(\gamma)) \tag{2.20}$$

The first term in the summation represents the perturbation in the geopotential due to the load itself.

Recalling that the spatially variable change in relative sea level, $\Delta\mathcal{SL}$, is defined as the difference between changes in the height of the surface equipotential and the solid Earth surface (Equation 2.10), it can be computed by differencing the Green's functions and spatio-

temporally convolving the result with the load forcing:

$$\Delta\mathcal{SL}(\theta,\psi,t_i) = \int_{-\infty}^{t_i} \iint_{\Omega} \Delta L(\theta',\psi',t') \left[\frac{\phi(\gamma,t_i-t')}{g} - \Gamma(\gamma,t_i-t')\right] d\Omega' dt' \tag{2.21}$$

where we have reintroduced spatial coordinates and:

$$\Delta L(\theta,\psi,t_i) = \rho_I \Delta I(\theta,\psi,t_i) + \rho_w \Delta S(\theta,\psi,t_i) \tag{2.22}$$

It will be useful to temporally discretize the surface mass load into a series of step load increments such that:

$$\Delta L(\theta,\psi,t_i) = \sum_{n=0}^{N} \left[\rho_I \delta I_n(\theta,\psi) + \rho_w \delta S_n(\theta,\psi)\right] H(t_i - t_n) \tag{2.23}$$

where $H(t_i - t_n)$ represents a Heaviside function and δI_n and δS_n are the step increments in the height of the grounded ice and ocean loads, respectively.

It will also be useful to decompose all spatial fields using spherical harmonic expansions. For example, we may write:

$$\Delta S(\theta,\psi,t_i) = \sum_{l=0}^{\infty} \sum_{m=-l}^{l} \Delta S_{l,m}(t) Y_{l,m}(\theta,\psi) \tag{2.24}$$

where $Y_{l,m}$ are the spherical harmonic basis functions of degree l and order m. We assume the following normalization of the spherical harmonic basis functions:

$$\iint_{\Omega} Y_{l\prime,m\prime}(\theta,\psi)Y_{l\prime,m\prime}(\theta,\psi)^{*}sin(\theta)d\theta d\psi = 4\pi a^{2}\delta_{l\prime,l}\delta_{m\prime,m} \tag{2.25}$$

By spectrally decomposing the grounded ice and ocean spatial fields, and using Equations 2.21 -2.23, we can evaluate the space and time convolutions analytically. In this case, the geographically variable change in global sea level can be written as:

$$\begin{aligned}\Delta\mathcal{SL}(\theta,\psi,t_i) = &\sum_{l=0}^{\infty}\sum_{m=-l}^{l} T_l E_l \left[\rho_I \Delta I_{l,m}(t_i) + \rho_w \Delta S_{l,m}(t_i)\right] Y_{l,m}(\theta,\psi) \\ &+ \sum_{l=0}^{\infty}\sum_{m=-l}^{l} T_l \sum_{n=0}^{i-1} \beta(l,t_n,t_i)\left[\rho_I \delta I_{l,m}(t_n) + \rho_w \delta S_{l,m}(t_n)\right] Y_{l,m}(\theta,\psi)\end{aligned} \tag{2.26}$$

where:

$$E_l = 1 + k_l^E - h_l^E \tag{2.27}$$

$$\beta(l,t_n,t_i) = \sum_{k=1}^{K} \frac{r_k'^l - r_k^l}{s_k^l}\left[1 - e^{-s_k^l(t_i - t_n)}\right] \tag{2.28}$$

and

$$T_l = \frac{4\pi a^3}{M_e(2l+1)} \tag{2.29}$$

Similarly, Equation 2.13 can be written as:

$$\frac{\Delta\Phi(t_i)}{g} = \frac{1}{A(t_i)}\left(-\frac{\rho_I}{\rho_w}\Delta I_{00}(t_i) - RO_{00}(t_i) + TO_{00}(t_i)\right) \tag{2.30}$$

where RO_{lm} and TO_{lm} are the spherical harmonic expansion of the second and third terms in Equation 2.13, respectively.

Equations 2.11, 2.26-2.30 represent the spectral form of the generalized sea-level equation valid for a 1-D, non-rotating Earth. At long timescales, the non-elastic component of the global sea-level change (the second term in Equation 2.26) dominates the loading response. At shorter timescales, the first term in Equation 2.26, representing the elastic response to load changes, dominates the global sea level response. We next consider the characteristics of these distinct responses in the following sections.

2.2.2 Viscoelastic Sea Level

Sea-level changes due to ongoing GIA from the melting of the Late Pleistocene ice sheets (which are assumed to have ended $\sim$ 5 ka) are computed using the complete viscoelastic sea-level equation. The prediction is sensitive to both the timing and geometry of the ice sheet deglaciation history and the assumed viscoelastic structure of the Earth. Relatively minor changes in the viscosity of the lower mantle can change the estimate of the rate of GMSL by ~ 0.5 mm/yr (Mitrovica and Davis, 1995).

Figure 2.4 shows the prediction of the present-day rate of change in sea level due to GIA assuming the ICE-5G deglaciation history (Peltier, 2004) and an Earth model that has a lithospheric thickness of 120 km, an upper mantle viscosity of 0.5×10^{21} Pa s and a lower mantle viscosity of 5×10^{21} Pa s. The patterns in the prediction can be separated into three regions dominated by distinct physical processes. The regions under the former ice sheets are currently experiencing a significant sea-level fall associated with the rebound of the lithosphere due to the removal of the ice sheets. For example, present-day sea level in

Hudson Bay and the Gulf of Bothnia is predicted to be falling due to GIA at a rate of ~ 10 mm/yr as a result of crustal uplift in these regions. Outside the footprint of the former ice sheet but still within the near-field, sea level is predicted to be rising at rates on the order of 1 - 5 mm/yr as regions in the periphery of ancient ice centers subside. Finally, beyond the peripheral bulges and away from the continental margins, water is moving from the far-field equatorial regions into the ocean regions being vacated by the subsiding peripheral bulges. This process, known as "ocean syphoning", causes a sea-level fall that has a maximum rate of ~ 0.5 mm/yr. Additionally in the far-field of the former ice sheets, but adjacent to the continents, the addition of the water load due to deglaciation drives a tilting at continental margins resulting in a sea level rise oceanward and a fall landward in a process termed "continental levering". A more detailed discussion of the above process may be found in Mitrovica and Milne (2002).

2.2.3 Elastic Sea Level

At short time scales, viscous effects are small and sea-level predictions are dominated by elastic and gravitational effects. The characteristic time scale for a Maxwell body with the properties of the mantle below the lithosphere is ~ 500 years. Considering only melting in the 20th century, a time span well below the Maxwell time, allows the viscous terms of the general sea-level equation to be ignored. In this case, the geographically variable component of the global sea-level change can be written as:

$$\Delta\mathcal{SL}(\theta,\psi,t_i) = \sum_{l=0}^{\infty}\sum_{m=-l}^{l} T_l E_l \left[\rho_I \Delta I_{l,m}(t_i) + \rho_w \Delta S_{l,m}(t_i)\right] Y_{l,m}(\theta,\psi) \tag{2.31}$$

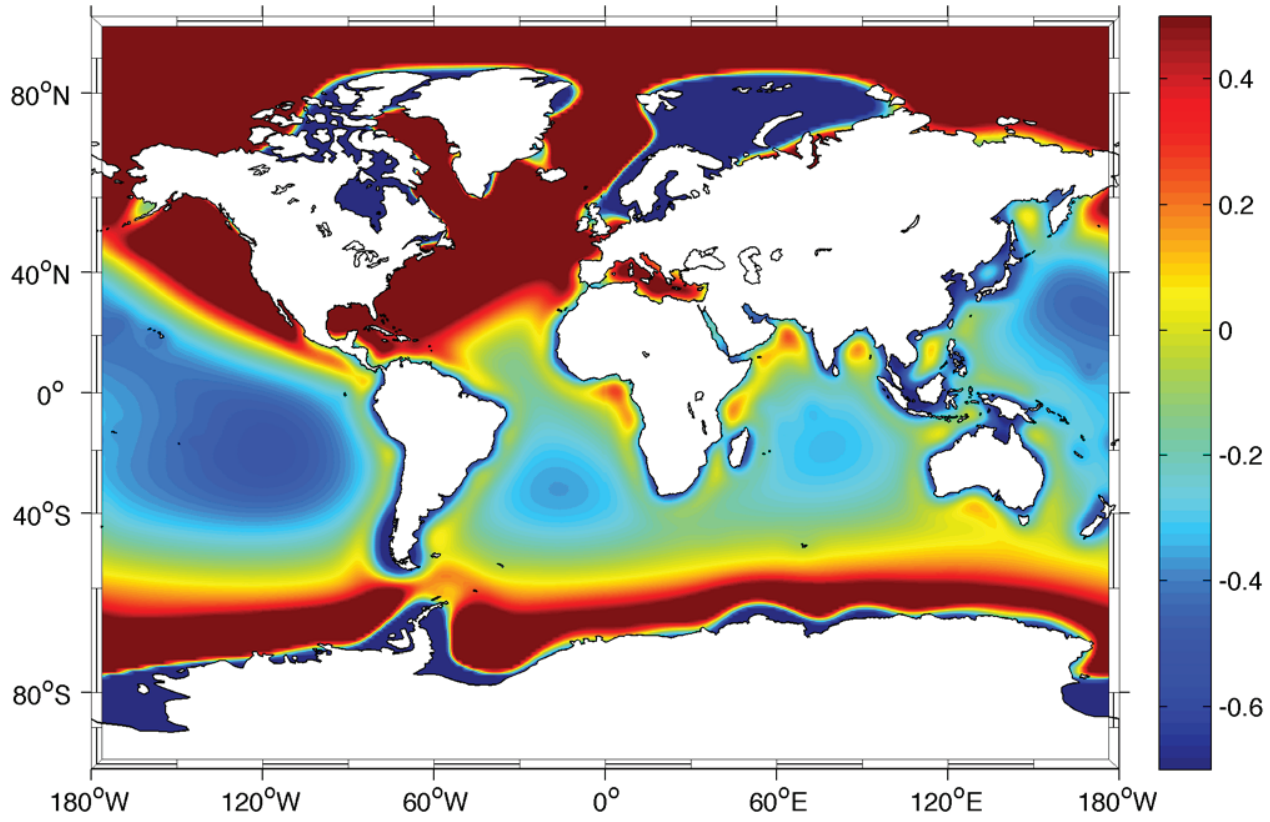

Figure 2.4: Prediction of the present-day rate of global sea-level change (mm/yr) due to on-going glacial isostatic adjustment. The calculation used the ICE-5G ice history (Peltier, 2004) with an Earth model consisting of a lithospheric thickness of 120 km, an upper mantle viscosity of 0.5×10^{21} Pa s and a lower mantle viscosity of 5×10^{21} Pa s.

Figure 2.5 shows the total (geographically variable plus uniform component) global sea-level change associated with rapid melt from the Greenland (top frame) and West Antarctic (bottom frame) ice sheets. These non-uniform patterns of sea-level change are unique for every meltwater source, and as such, they have come to be known as "sea-level fingerprints". The fingerprints in Figure 2.5 are shown normalized to the equivalent eustatic value associated with the melt event.

Both of the fingerprints in Figure 2.5 were computed by assuming a uniform melt across each of the respective ice sheets. While the fingerprints are sensitive to the melt geometry, the sensitivity decreases rapidly with distance from the ice sheet and thus the far-field regions are relatively insensitive to the melt geometry (Mitrovica et al., 2011). With the bulk of 20th century sea-level observations being located in the far-field of the ice sheets, the assumption of uniform melt is appropriate.

Within the near-field of the melting ice sheet, sea level falls due to the reduction of gravitational attraction from the melting ice sheet on the ocean and due to the uplift of the lithosphere in response to the unloading. This fall can be up to an order of magnitude greater than the equivalent eustatic value of the melt. As one moves away from the near-field, the sea level increases such that deep in the far-field of the melting ice sheet the predicted sea-level rise can be up to 30% higher than the equivalent eustatic rise associated with the melt event.

Although the theory described in Sections 2.2.1 - 2.2.3 is valid for a non-rotating Earth, the results in Figures 2.4 and 2.5 dove the generalized sea-level equation (Equation 2.11) in Section 2.2, using a spectral theory valid for a rotating Earth. The extensions necessary to

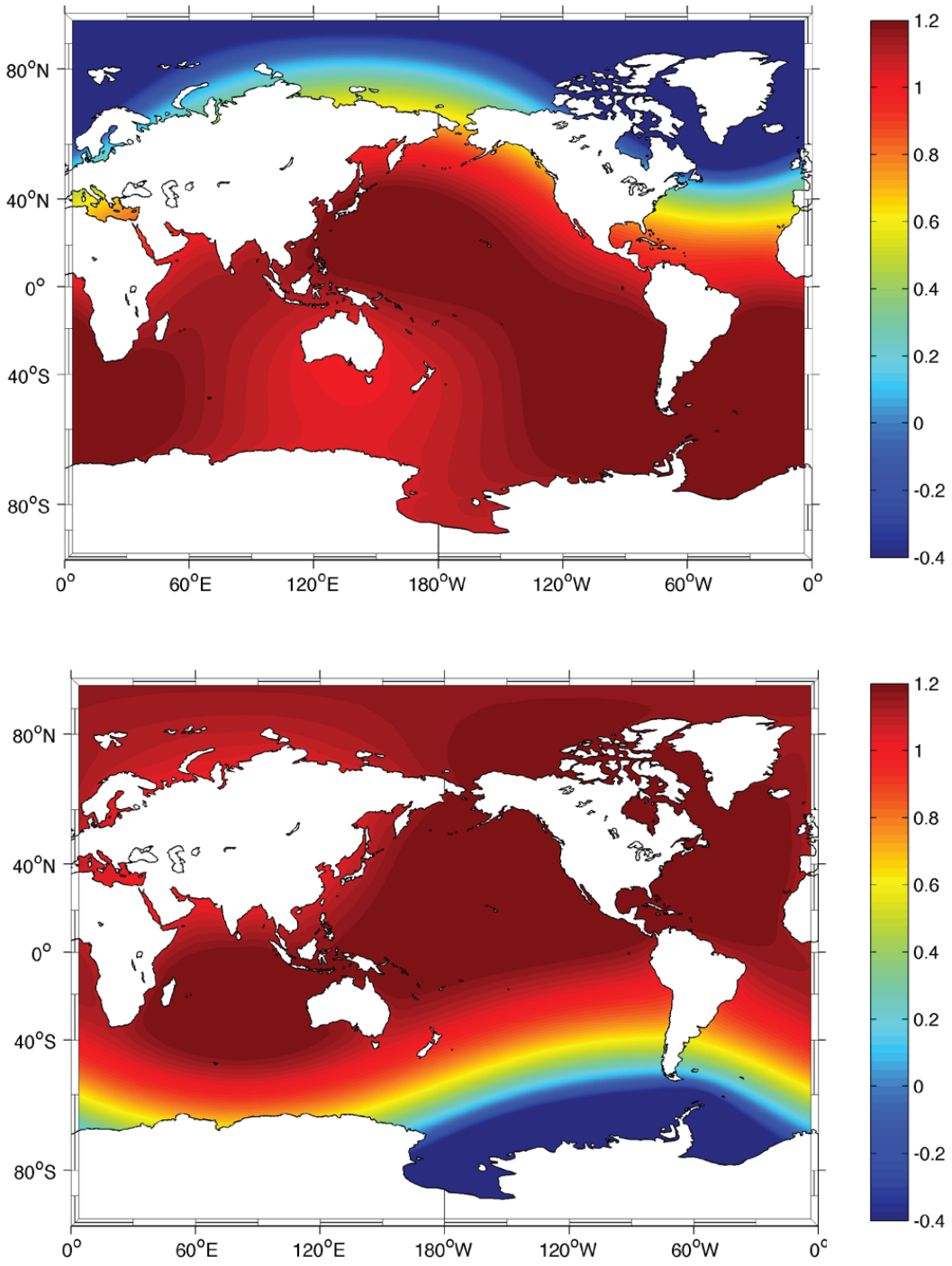

Figure 2.5: Predicted sea-level fingerprints associated with uniform melt across the Greenland Ice Sheet (top) and the West Antarctic Ice Sheet (bottom). The predictions are normalized such that they represent the change in mm per mm of the equivalent eustatic sea-level change associated with the melt.

treat this case are given in Kendall et al. (2005).

Chapter 3

An Enigma in Current Estimates of Past Dynamic Ellipticity

Abstract

The precession and obliquity frequencies of the Earth's rotational motion are functions of the dynamic ellipticity of the Earth's gravitational figure, and this connection has provided a novel bridge between studies of palaeoclimate and geodynamics. In particular, analyses of tuned climate proxy records have yielded bounds on the mean relative perturbation in dynamic ellipticity over both the last 3 Myr and 25 Myr that are less than $\sim$3 per cent of the non-hydrostatic component of the ellipticity. We demonstrate that this apparent consistency actually defines an important geophysical enigma. Over the last 3 Myr, changes in the Earth's figure are likely dominated by ice age forcings - in this case, a small perturbation to dynamic ellipticity implies significant isostatic compensation of the ice-ocean surface mass loads and, hence, a relatively low mantle viscosity. In contrast, over the last 25 Myr, changes in the Earth's long-wavelength gravitational form are likely dominated by mantle convective flow,

This Chapter was published with J. X. Mitrovica, A. M. Forte, P. Glisŏvić and P. Huybers in Geophysical Journal International (2012), Vol. 191, 1129 - 1134.

and in this case, the small perturbation to dynamic ellipticity implies sluggish convection and a relatively high mantle viscosity. There are at least four possible routes to resolving this enigma: The viscosity in the Earth's mantle is transient (i.e. dependent on the timescale of the applied forcing), tidal dissipation changed in a manner between the last 3 Myr and 25 Myr that was sufficient to resolve the issue, the observationally inferred bounds are unrealistically restrictive, or Earth models exist in which the ice age and convection effects approximately cancel leading to no net perturbation. In this paper, we compute a suite of numerical predictions of ice age and convection-induced perturbations to the dynamic ellipticity to illustrate the enigma described above.

3.1 Introduction

Analysis of deep-sea sedimentary cores has revealed Milankovitch band variations in a diverse suite of climate proxy records, including, for example, depth-series of elemental and isotopic ratios, organic material, and magnetic susceptibility (Shackleton et al., 1999; Pälike and Shackleton, 2000; Lourens et al., 2001; Lisiecki and Raymo, 2005). Comparison of these variations with results from many-body orbital integrations (Laskar et al., 1993) allows these depth-series to be converted to time series through a process termed astronomical calibration - or tuning - which has been applied to major portions of the Cenozoic time-scale (Shackleton et al., 1990; Hilgen et al., 1995; Shackleton et al., 1999). The accuracy of the tuning procedure is a function of several factors, notably the existence of well-dated tie points within the cores, such as magnetic reversals, and the stability of Milankovitch frequencies within the precession and obliquity bands. In particular, these frequencies are

functions of the dynamic ellipticity of the Earth, and there has been growing appreciation that geophysical processes, such as glacial isostatic adjustment (GIA) associated with the last ice age (Laskar et al., 1993; Mitrovica et al., 1994; Mitrovica and Forte, 1995; Jiang and Peltier, 1996) and thermal convection within the Earth's mantle (Forte and Mitrovica, 1997) will drive non-negligible perturbations in this ellipticity. Moreover, with an eye to the geophysical implications, several studies have used paleoclimate records obtained from marine sediment cores to place bounds on the variation of the dynamic ellipticity across time scales extending over the past 3 Myr (Lourens et al., 2001) and 25 Myr (Pälike and Shackleton, 2000). The dynamic ellipticity (H), or precession constant, of the Earth is defined as:

$$H = \frac{C - \frac{1}{2}(A + B)}{C} \tag{3.1}$$

where C is the polar moment of inertia and A and B are the principal equatorial moments of inertia. One can show that the relative perturbation in H may be written as (Laskar et al., 1993; Mitrovica et al., 1994):

$$\frac{\delta H}{H} = \frac{3}{2H}\frac{\delta C}{C} \tag{3.2}$$

A related, and perhaps more physical measure of the oblateness of the planet is the flattening, f. The flattening is defined as the difference between the equatorial and polar radii of the Earth's geoid at spherical harmonic degree and order (2,0), and it is related to the perturbation in the dynamic ellipticity by:

$$\delta f = \frac{3CH}{2M_e a}\frac{\delta H}{H} = 1.06 \times 10^4 \frac{\delta H}{H} \tag{3.3}$$

where M_e and a are the mass and radius of the Earth, respectively, and f is in meters.

The Earth's dynamic ellipticity is dominated by the hydrostatic form, which denotes the equilibrium, fluid response of the planet to its present rotation rate. The residual, non-hydrostatic form of the Earth is characterized by an excess ellipticity of $\delta H/H = 0.011$ or, alternatively, an excess flattening of $\delta f = 113$ m (Chambat et al., 2010). The excess flattening is widely thought to be driven by mantle convective flow, and specifically the distortion of the Earth's form associated with two super plumes rising from the core-mantle-boundary below Africa and the southeast Pacific (Lithgow-Bertelloni and Silver, 1998) and the ring of subduction encircling the Pacific Ocean. In the following, we will denote the observationally-inferred and predicted perturbations from these present-day values by $\delta H/H$ and δf. Furthermore, the mean value of these perturbations over a time window of 3 Myr and 25 Myr will be denoted by $\langle\rangle_{3Ma}$ and $\langle\rangle_{25Ma}$, respectively.

Bounds on $\langle \delta H/H \rangle$ and $\langle \delta f \rangle$ obtained by Lourens et al. (2001) and Pälike and Shackleton (2000) from the analysis of sedimentary cores are shown in Figure 3.1. Lourens et al. (2001) measured the depth variation of a titanium-aluminum ratio within a core drilled in the eastern Mediterranean (ODP Site 967) dated to span 2.44-2.90 Ma. They compared this depth series to orbital (many-body) solutions generated for a suite of integrations in which the tidal dissipation and dynamic ellipticity were varied from their present-day values. They concluded that 0.0003 > $\langle \delta H/H \rangle_{3Ma}$ > -0.0003 or, equivalently, that 3.2 m > $\langle \delta f \rangle_{3Ma}$ > -3.2 m (Figure 3.1A). Pälike and Shackleton (2000) bounded the tidal dissipation and dy-

namic ellipticity over the past 25 Myr by fitting the amplitude modulation of a magnetic susceptibility record from the Ceara Rise (ODP Leg 154) interfered with a reference orbital signal to a semi-analytical approximation to the orbital solution. They concluded that 0.0004 $> \langle \delta H/H \rangle_{25Ma} >$ -0.0001 or, equivalently, that 4.2 m $> \langle \delta f \rangle_{25Ma} >$ -1.1 m (Figure 3.1B).

The apparent consistency between these bounds on the Earth's dynamic ellipticity may be misleading. The two analyses cover different time scales and, more importantly, the dominant geophysical processes that drive changes in the Earth's figure over each of these time scales may be distinct. Over the last 2-3 Myr, perturbations in the Earth's dynamic ellipticity are thought to be largely driven by glacial isostatic adjustment (GIA); that is, mass redistribution associated with the Plio-Pleistocene ice age. In this case, the bound on $\langle \delta H/H \rangle_{3Ma}$ obtained by Lourens et al. (2001) implies that the ice-age surface mass loading remained largely isostatically compensated across the glacial period and this, in turn, implies a relatively low deep mantle viscosity. In contrast, the advection of density heterogeneities and boundary deformation associated with thermal convection in the Earth's mantle are thought to dominate changes in the Earth's ellipticity over the longer, 25 Myr, time scale. In this case, the bound on $\langle \delta H/H \rangle_{25Ma}$ derived by Pälike and Shackleton (2000) implies sluggish mantle flow and, hence, a high deep mantle viscosity. Thus, the consistency in the bounds on $\langle \delta H/H \rangle$ over the last 3 Myr and 25 Myr defines a potentially important enigma in our present understanding of the global scale dynamic evolution of the Earth during the Late Cenozoic.

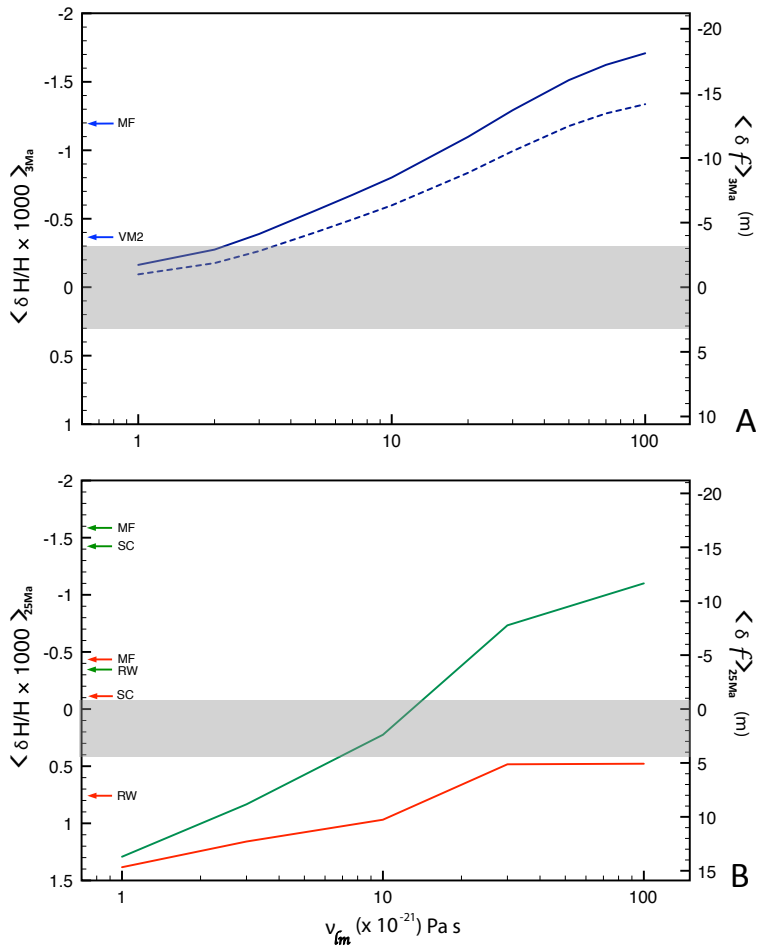

Figure 3.1: (A) Observationally inferred and predicted perturbations in the dynamic ellipticity over the last 3 Myr. The shaded region is the bound on the mean relative perturbation in the dynamic ellipticity inferred by Lourens et al. (2001) from the analysis of a sedimentary core from the eastern Mediterranean dated to span 2.442.90 Ma. The solid blue line is a prediction of $< \delta H/H >_{3Ma}$ due to GIA as a function of the lower-mantle viscosity of the adopted earth model using an ice volume history inferred from the oxygen isotope record of Lisiecki and Raymo (2005) (see text). The blue arrows marked MF and VM2 are GIA predictions of $< \delta H/H >_{3Ma}$ based on the same ice history and viscosity models MF and VM2 (see Fig. 3). The dashed blue line is identical to the solid, with the exception that ice volumes are inferred from the sea level estimate of de Boer et al. (2010). (B) As in frame A, except for the time span of 25 Myr. The shaded region is the associated bound on $< \delta H/H >_{25Ma}$ derived by Pälike and Shackleton (2000) from a magnetic susceptibility record from the Ceara Rise. The red line is a numerical prediction of $< \delta H/H >_{25Ma}$ due to mantle convection. The green line is a prediction of the total $< \delta H/H >_{25Ma}$ due to both mantle convection and GIA. The arrows MF, RW and SC are predictions of $< \delta H/H >_{25Ma}$ computed using the viscosity models MF, RW and SC (see Figure 3.3), respectively. In this case, the red and green arrows refer to predictions including mantle convection alone and mantle convection plus GIA, respectively.

3.2 Numerical Results

3.2.1 Defining the Enigma

To begin, we outline a suite of numerical predictions of the $\delta H/H$ over the last 3.0 Myr due to GIA. The calculations are based on the methodology outlined in Mitrovica et al. (1997). We adopt a spherically symmetric, self-gravitating, elastically compressible Maxwell viscoelastic Earth model with the elastic and density structure prescribed from the seismic model PREM (Dziewonski and Anderson, 1981). The ice model used in the calculation is constructed in a two step procedure ultimately based on the ICE-5G model for the geometry of global ice cover during the last glacial cycle (Peltier, 2004). First, we convert a global stack of oxygen isotope ratios (Lisiecki and Raymo, 2005) over the past 3 Myr (Figure 3.2A) into a time series of ice volume changes relative to the present day. The scaling we adopt yields a change in ice volume from LGM to present that matches the ICE-5G model ice history. Next, whenever the ice volume matches one of the time slices of the ICE-5G model, we adopt the ice geometry of the latter in the former. Perturbations in the dynamic ellipticity are relatively insensitive to the level of uncertainty that characterizes the mapping between oxygen isotope variations and eustatic sea level (see below). Moreover, perturbations in H reflect deformation on very long spatial scales, and therefore predictions of these perturbations are also insensitive to the detailed spatial geometry of the model ice history.

In addition to the ice load, a gravitationally self-consistent ocean load is computed by solving a sea-level equation that accounts for shoreline migration, changes in the extent of grounded, marine-based ice and the feedback of rotation into sea level (Kendall et al., 2005). One output of the sea-level calculation is the time variation in the height of the geopotential

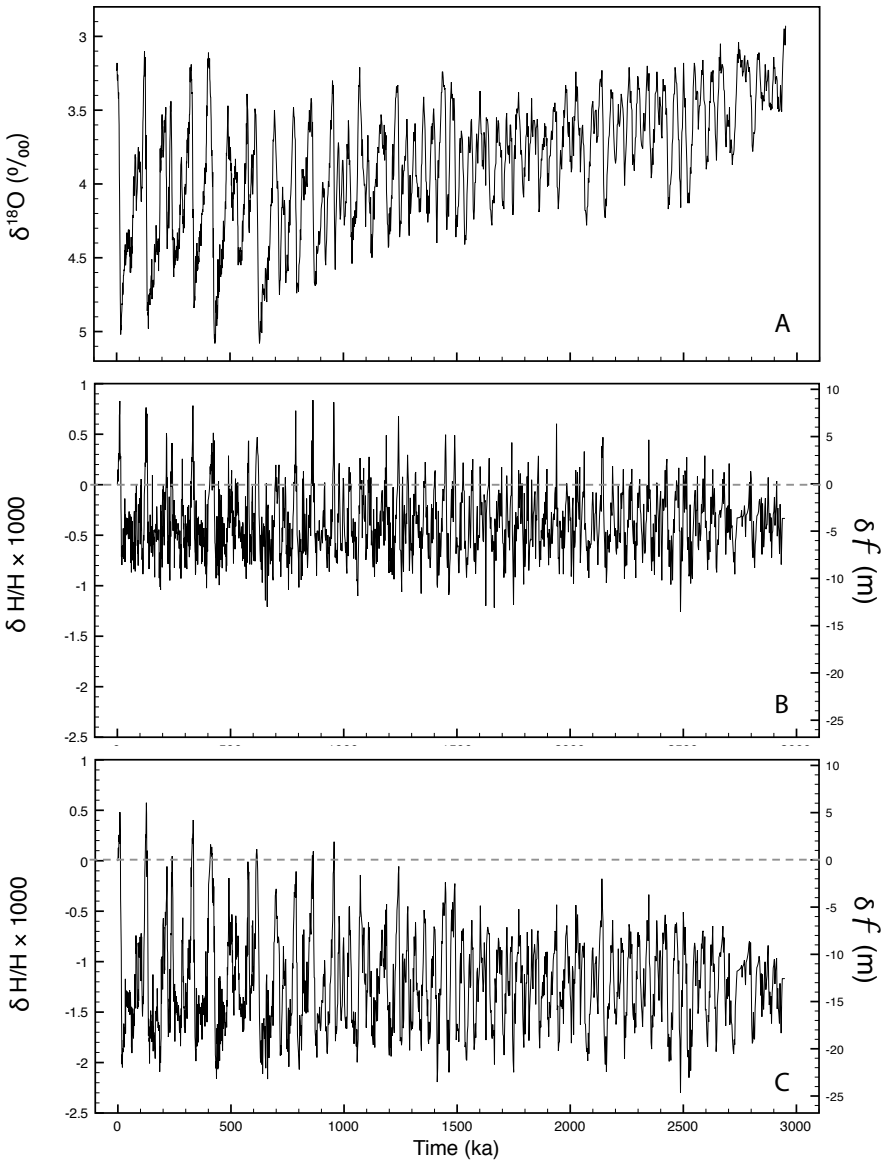

Figure 3.2: (A) Global stack of benthic $\delta^{18}O$ records over the last 3Myr from Lisiecki and Raymo (2005). (B) Numerical prediction of the relative perturbation in dynamic ellipticity, $\delta H/H$ due to GIA, based on the ice history derived from frame A (see text) and the VM2 profile of mantle viscosity (Peltier, 2004). (C) As in frame B, except that the MF viscosity model is adopted (Mitrovica and Forte, 2004).

that defines the sea-surface; the perturbation in dynamic ellipticity is proportional to the spherical harmonic degree two zonal component of this time series (Mitrovica et al., 1997).

Figures 3.2B and 3.2C show predictions of $\delta H/H$ based on two distinct profiles of mantle viscosity, the VM2 model derived on the basis of GIA data (Peltier, 2004) and model MF, which is one of a suite of models inferred from a joint inversion of GIA and mantle convection data sets (Mitrovica and Forte, 2004). These models are shown in Figure 3.3. Model VM2 is characterized by mean upper and lower mantle viscosities of $\sim 5 \times 10^{20}$ Pa s and $\sim 2 \times 10^{21}$ Pa s, respectively; analogous means for model MF are $\sim 4 \times 10^{20}$ Pa s and 2×10^{22} Pa s. The mean values of the time series in Figures 3.2B and C, i.e., $\langle \delta H/H \rangle_{3Ma}$ are -0.37×10^{-3} ($\langle \delta f \rangle_{3Ma}$ = -3.9 m) and -1.20×10^{-3} ($\langle \delta f \rangle_{3Ma}$ = -12.7 m), respectively. These values are plotted as blue arrows on the left side of Figure 3.1A. Both models predict perturbations in the mean dynamic ellipticity over the last 3 Myr that fall outside the range inferred by Lourens et al. (2001) on the basis of the core data from the eastern Mediterranean (see Figure 3.1), though the misfit associated with the VM2 prediction is relatively small.

The average ice cover over the last 3 Ma is greater than in the current interglacial. Therefore, the ice age perturbation to the mean value of H over the last 3 Ma will always be negative (i.e., more mass will be concentrated at the poles during periods of glaciation than at present day), as in Figures 3.2B and 3.2C. The magnitude of the (negative) perturbation will have a strong sensitivity to the lower mantle viscosity (Mitrovica and Forte, 1995; Mitrovica et al., 1997). In particular, the higher the lower mantle viscosity, the smaller the level of isostatic compensation of the surface mass load, and the greater the ice age perturbation to the dynamic ellipticity. The mean lower mantle viscosity in model MF is about ten times the mean value for model VM2, and this explains the higher amplitude of the perturbation in Figure 2C relative to 2B.

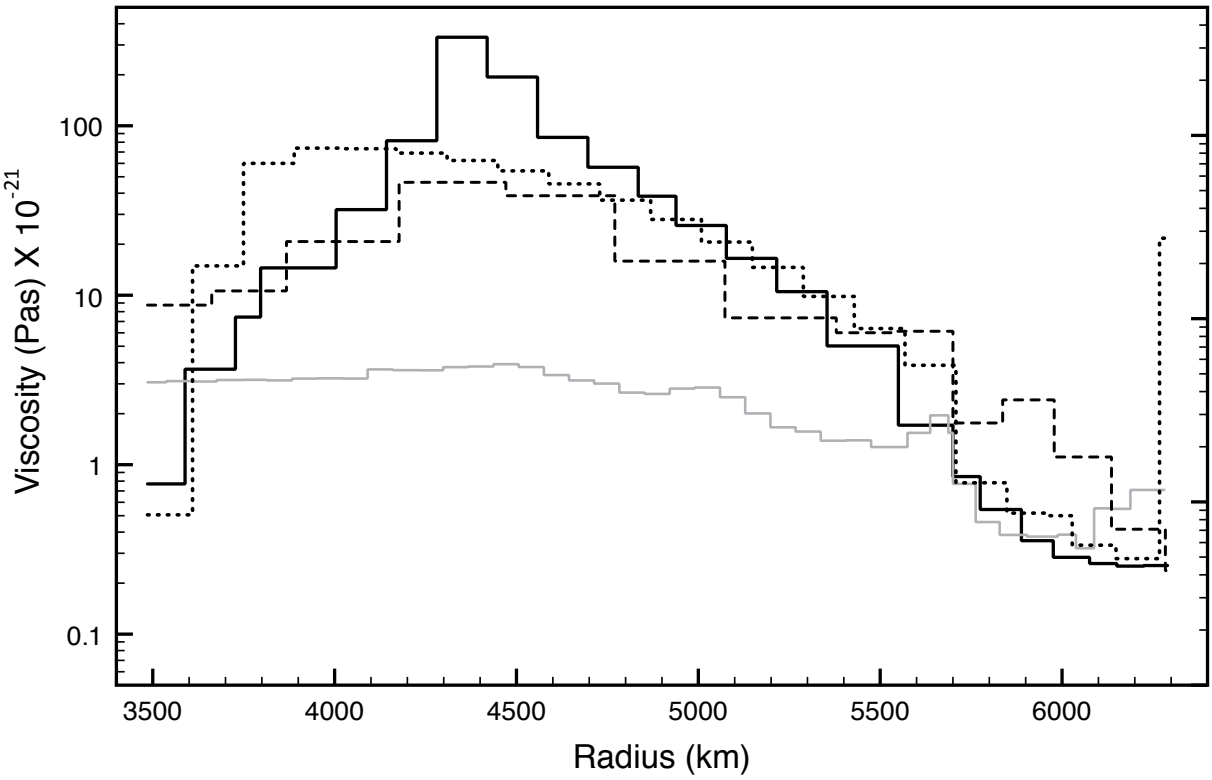

Figure 3.3: The four radial profiles of mantle viscosity described in the text, MF (black solid line), SC (dotted line), RW (dashed line) and VM2 (solid grey line).

The sensitivity of the GIA prediction to viscosity is systematically explored in Figure 3.1A (solid line), where we plot values of $< \delta H/H >_{3Ma}$ generated using a suite of Earth models in which a constant lower mantle viscosity (henceforth denoted by ν_{lm}) is varied from 10^{21} Pa s to 10^{23} Pa s. This range encompasses all geophysical estimates of ν_{lm} published in the last 40 years. These predictions adopt a constant upper mantle viscosity of 5×10^{20} Pa s and the ice history prescribed above. Over this range of lower mantle viscosity, the mean ice age perturbation to the dynamic ellipticity increases monotonically to a value of -1.7×10^{-3} ($\langle \delta f \rangle_{3Ma}$ = -18.0 m) as ν_{lm} is increased to 10^{23} Pa s. Most importantly, the bound on $\langle \delta H/H \rangle_{3Ma}$ inferred by Lourens et al. (2001) is only fit with an ice age calculation in which the lower mantle viscosity is less than 2×10^{21} Pa s.

de Boer et al. (2010) have inferred a time series of eustatic sea-level variations over the last 35 Myr on the basis of inverse modeling of benthic $\delta^{18}O$ records in combination with 1-D ice sheet models. We include this time series as their results indicate that the scaling between δ^{18}O and ice volume is not constant over the past 35 Myr. The most recent 25 Myr of this time series is shown in Figure 3.4A. The dashed line in Figure 3.1A is analogous to the solid line with the exception that the ice history used in the prediction of $\langle \delta H/H \rangle_{3Ma}$ is constructed from the last 3 Myr of the de Boer et al. (2010) time series. These results are on the order of 20% smaller than those based on the ice history inferred from the time series in Figure 3.2A. This difference is consistent with the excess ice volumes at LGM associated with these two ice histories. In particular, the ICE-5G history is characterized by a eustatic sea level change of $\sim$ 130 m, whereas this difference is $\sim$ 104 m in the time series derived by de Boer et al. (2010).

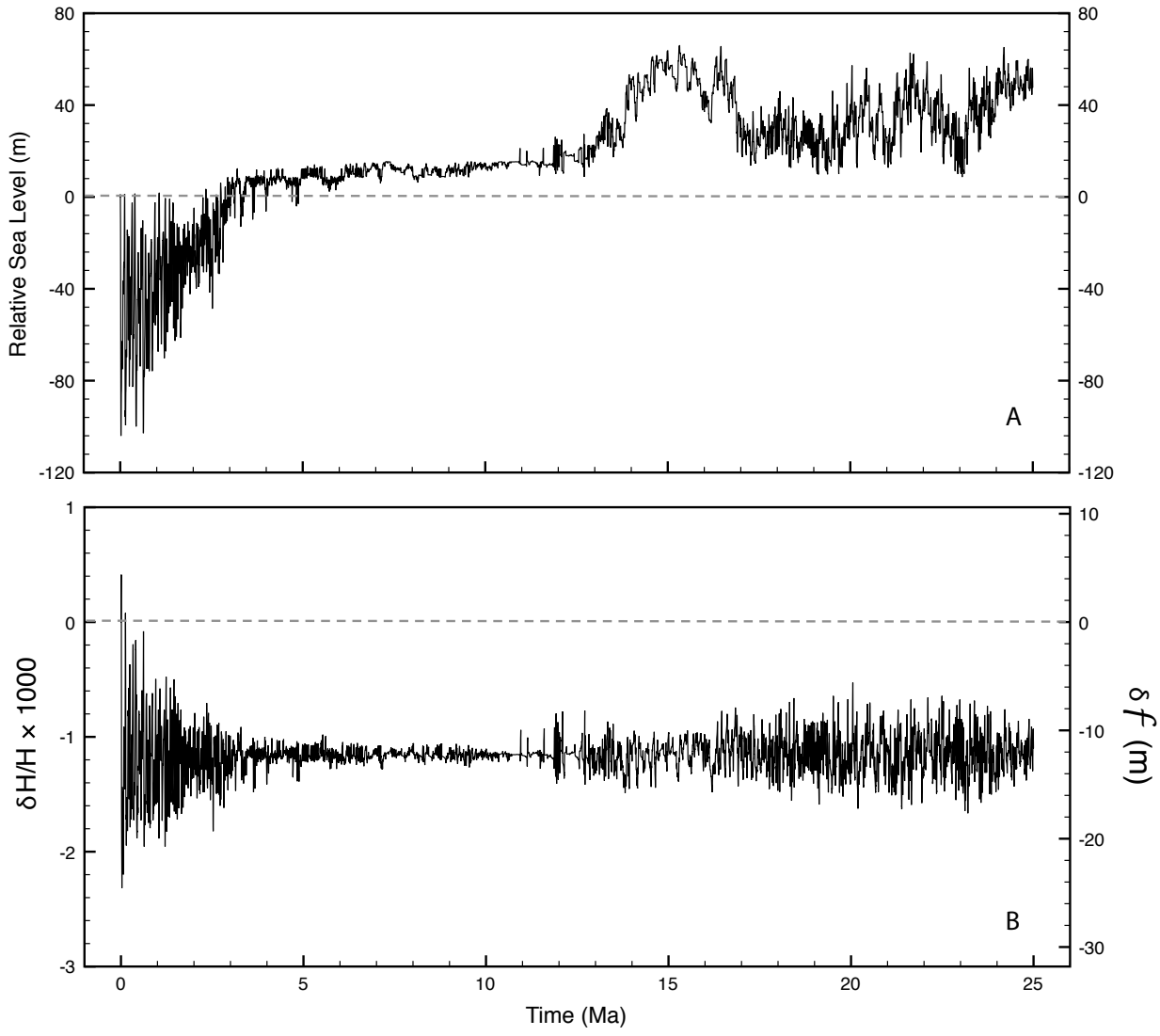

Figure 3.4: (A) A time-series of eustatic sea level relative to present day for the past 25 Myr compiled by de Boer et al. (2010). (B) Numerical prediction of the relative perturbation in dynamic ellipticity, $\delta H/H$ due to GIA, based on the ice history derived from frame A (see text) and the MF profile of mantle viscosity (see Figure 3.3)

Next, we turn to predictions of the perturbation in dynamic ellipticity over the last 25 Myr driven by mantle convection. These predictions adopt the tomography based flow model described in Forte et al. (2010) that solves the field equations valid for a compressible, Newtonian viscous fluid within a spherical shell geometry. Surface tectonic motions are coupled to the mantle flow rather than being imposed as boundary conditions (Forte, 2007). The system of governing equations is backward advected 25 Myr from an initial density field derived via a joint inversion of global seismic and geodynamic data sets (Simmons et al., 2009). The latter includes present-day free-air gravity anomalies, surface (crust-corrected) dynamic topography, tectonic plate motions, and the geodetically inferred excess ellipticity of the core-mantle-boundary. The inversion is based on viscosity model MF. Figure 3.5 shows time series of $\delta H/H$ computed using viscosity profile MF. From this time series we obtain a mean perturbation $< \delta H/H >_{25Ma} = -4.1 \times 10^{-4}$.

The sensitivity of the convection-induced mean perturbation, $\langle \delta H/H \rangle_{25Ma}$, to ν_{lm} is illustrated in Figure 3.1B (red line), where, we show results for a suite of models in which ν_{lm} is varied from 10^{21} Pa s to 10^{23} Pa s. The bound derived by Pälike and Shackleton (2000) is best fit for Earth models with a lower mantle viscosity in excess of 3×10^{22} Pa s. This preference for a high viscosity deep mantle is not surprising given that the bound on the mean perturbation in $\langle \delta H/H \rangle_{25Ma}$ or $\langle \delta f \rangle_{25Ma}$ derived by Pälike and Shackleton (2000) is only a few percent of the total present-day excess ellipticity and flattening of the Earth thought to be driven by mantle flow. This level of perturbation to the dynamic ellipticity or flattening over the past 25 Myr strongly implies a sluggish overturn time.

In addition to the results for the model MF, Figure 3.5 also shows time series of $\delta H/H$

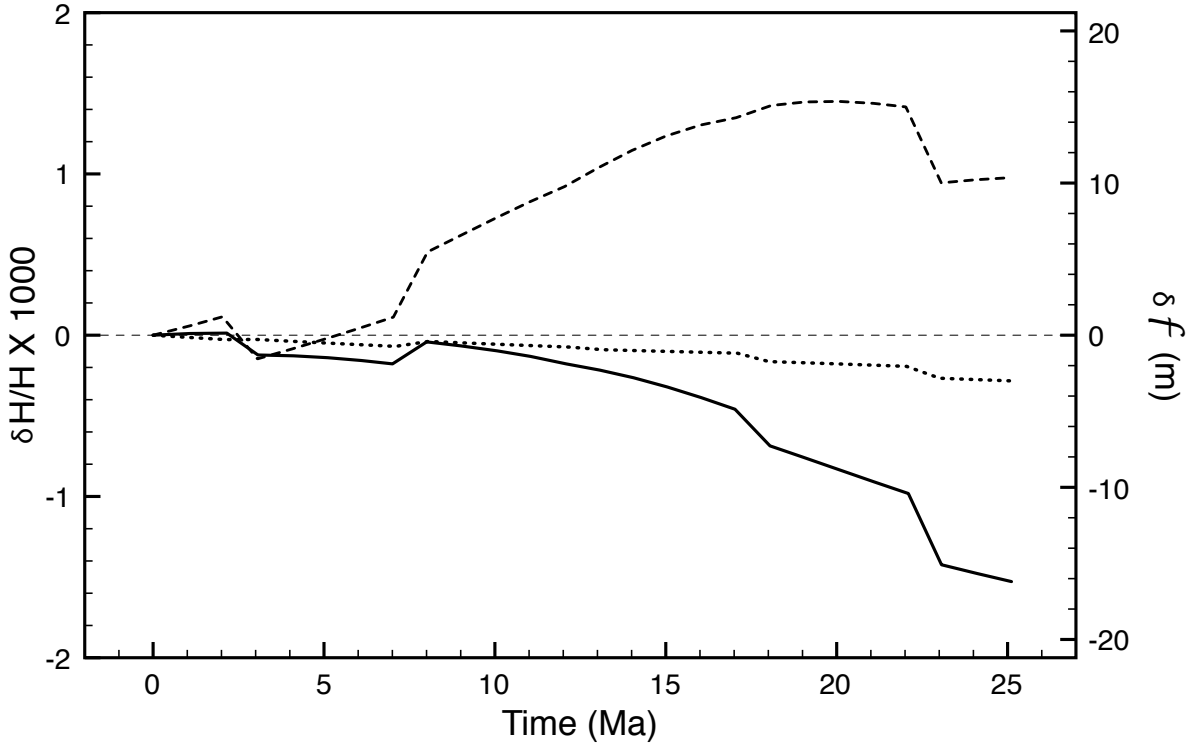

Figure 3.5: Numerical prediction of the relative perturbation in dynamic ellipticity, $\delta H/H$ due to mantle convection based on the viscosity models MF (black solid line), SC (dotted line) and RW (black dashed line). Details of the calculation are described in the text.

computed using two additional viscosity profiles, which we label as RW and SC (see Figure 3.3). The profile RW, taken from Ricard and Wuming (1991), is inferred from a set of surface geophysical observables related to mantle convection, while the model SC (Steinberger and Calderwood, 2006) is additionally constrained using results from mineral physics. In contrast to MF, the profiles RW and SC are not directly constrained by GIA data, although model SC satisfies the so-called Haskell average of mantle viscosity derived from the analysis of ice age data (Mitrovica, 1996). The mean perturbation in $\langle \delta H/H \rangle_{25Ma}$ obtained from the three time series in Figure 3.5 are shown in Figure 3.1B (red arrows). These results cluster around the observational constraint of Pälike and Shackleton (2000). (We also computed the mean GIA-induced perturbation, $\langle \delta H/H \rangle_{3Ma}$, using models RW and SC. The values we obtained, -1.15×10^{-3} and -1.36×10^{-3} respectively, are consistent with the prediction based on MF shown in Figure 3.1A.)

The two frames of Figure 3.1 define the enigma introduced above. No value of ν_{lm} within the family of two layer viscosity profiles we have adopted can simultaneously reconcile the ice age and mantle convection predictions of changes in the dynamic ellipticity with the bounds estimated by Lourens et al. (2001) and Pälike and Shackleton (2000). The ice age predictions (Figure 3.1A, blue line) require a relatively weak lower mantle viscosity to satisfy the bound on $\langle \delta H/H \rangle$ for the past 3.0 Myr, but this class of viscosity models will produce a gross misfit between mantle convection predictions over the past 25 Myr and the associated bound on dynamic ellipticity (Pälike and Shackleton, 2000). As an example, while an ice age prediction based on model VM2 falls moderately above the lower bound on $\langle \delta H/H \rangle_{3Ma}$ derived by Lourens et al. (2001), a convection simulation based on the same viscosity model yields a

perturbation to $\langle \delta H/H \rangle_{25Ma}$ that is three times higher than the bound on this quantity derived by Pälike and Shackleton (2000). Similarly, the high values of ν_{lm} necessary to reconcile the constraint on the mean value of $\delta H/H$ over the last 25 Myr derived by (Pälike and Shackleton, 2000) (Figure 3.1B; red line) will predict an ice age perturbation that is many times higher than the bound inferred by Lourens et al. (2001). This is demonstrated by the results based on models MF, RW and SC: While these models yield a convection-induced $\langle \delta H/H \rangle_{25Ma}$ that cluster around the observed bound on this quantity, these models predict a GIA-induced mean perturbation $\langle \delta H/H \rangle_{3Ma}$ that significantly exceeds the bound provided by Lourens et al. (2001).

Not all models considered in Figure 3.1 fit the broad suite of GIA and mantle convection data sets that have been used to infer mantle viscosity (Nakada and Lambeck, 1989; Lambeck et al., 1998; Mitrovica and Forte, 2004; Peltier, 2004). As an example, while the viscosity models VM2 and MF have been independently inferred by groups analyzing GIA data, the two layer model with $\nu_{lm} = 10^{23}$ Pa s would grossly misfit most GIA data sets. In regard to Figure 3.1B, model MF provides an excellent fit to data sets connected to mantle convection (e.g., long wavelength geoid harmonics, divergence of horizontal plate motions, dynamic topography, and the excess ellipticity of the core mantle boundary). As a specific example, MF provides a 86% variance reduction of geoid harmonics up to degree and order 32. In contrast, the three lowest viscosity models sampled by the red line in Figure 3.1B ($\nu_{lm} = 10^{21}, 3 \times 10^{21}, 10^{22}$ Pa s) increase the variance by 226%, 140% and 33% respectively, while the two higher viscosity models (3×10^{22} and 10^{23} Pa s) decrease the variance by only 51% and 18% respectively. That is, models with a constant lower mantle viscosity of 10^{22}

Pa s or less (including VM2) provide a very poor fit to surface observables related to mantle convection.

3.3 Discussion: Resolving the Enigma?

There are at least four possible routes to resolving the enigma described above. First, the results in Figure 3.1 may indicate that the viscosity of the mantle is transient; that is, the viscous response to an applied stress is a function of the time scale of the forcing. A flurry of ice-age related papers in the early 1980s considered this possibility (Sabadini et al., 1985), but interest in the topic diminished when no unambiguous evidence of such behaviour emerged in the analysis of GIA data sets and when viscosity profiles were found that could simultaneously reconcile observational constraints associated with GIA and mantle convection (Nakada and Lambeck, 1989; Lambeck et al., 1998; Mitrovica and Forte, 2004).

Second, bounds on $\delta H/H$ derived from deep-sea sedimentary core records may not be robust. For example, Lourens et al. (2004) have highlighted an inaccuracy in the age model adopted by Pälike and Shackleton (2000). Moreover, estimating the stability of Milankovitch frequencies using a time series that has been pre-tuned to an orbital solution raises the possibility of circular reasoning. This concern was explicitly noted by Pälike and Shackleton (2000) and Lourens et al. (2001), though both studies argued that their analysis procedure minimized or avoided the circularity.

Third, tidal dissipation (which also impacts dynamic ellipticity) varies with time (Hansen, 1982; Egbert et al., 2004). It is possible that tidal dissipation varied over the last 3 Myr and 25 Myr in the manner necessary to reconcile the enigma (i.e. that changes in the tidal

dissipation compensated the geodynamic perturbations to H). (We note that the impact of so-called climate friction on the geological record is thought to be negligible and its contribution can be added as a small perturbation to tidal dissipation parameters (Laskar et al., 2004)).

Fourth, it may be possible that Earth models exist which yield GIA and convection predictions of $\delta H/H$ that are of opposite sign and approximately equal amplitude. The fact that viscosity profiles with significant similarities (MF, RW and SC in Figure 3.3) yield a wide range of predictions of $\langle \delta H/H \rangle_{25Ma}$ suggests that a search for such models may be warranted.

Insight into these issues may be deepened by taking the calculations described above one step further. In particular, to this point we have considered the perturbations in the dynamic ellipticity due to GIA and mantle convection in isolation. However, it is possible that convection may produce an important perturbation to $\delta H/H$ over the last 3 Myr and that GIA may do the same over the last 25 Myr. We considered the impact of convection on $\langle \delta H/H \rangle_{3Ma}$, by taking the average, over only the last 3 Myr, of the 25 Myr model results. For each model, the 3 Myr average was less than 0.08×10^{-3}, and we conclude that the GIA signal dominates $\langle \delta H/H \rangle_{3Ma}$.

In Figure 3.1B we show predictions of the combined GIA and mantle convection signal on the mean perturbation $\langle \delta H/H \rangle_{25Ma}$. The GIA signal in this case is first computed by constructing an ice sheet model over the last 25 Myr using the time series of eustatic sea level variations derived by de Boer et al. (2010) (Figure 3.4A). Figure 3.4B shows, in analogy with Figures 3.2B and C, a prediction of $\delta H/H$ over the last 25 Myr predicted

using viscosity model MF. (The main difference between these calculations and the earlier GIA predictions for the last 3 Myr, is that over the longer time interval we assume that the ocean load variation is geographically uniform. This assumption introduces an error less than $\sim 5\%$ in predictions of the mean perturbation to the dynamic ellipticity.) Repeating this GIA calculation for two layer viscosity profiles and a suite of ν_{lm} values, computing the mean perturbation over the last 25 Myr, and adding the result to the convection-only calculation based on the same viscosity model (red line, Figure 3.1B) yields the total (GIA plus convection) predicted perturbation (green line, Figure 3.1B). In this case, the magnitude of the GIA contribution is greater than the magnitude of the convection signal for Earth models with a lower mantle viscosity higher than 10^{22} Pa s. This is as one would expect from earlier results; the higher the viscosity, the less complete the isostatic compensation of the ice age surface mass load and the more sluggish the convective flow. We note that while the convection only signal (red line) nearly fits the constraint on $\langle \delta H/H \rangle_{25Ma}$ derived by Pälike and Shackleton (2000) for models with $\nu_{lm} > 3 \times 10^{22}$ Pa s, the combined signal from GIA plus convection only fits this constraint for a band of ν_{lm} values near 10^{22} Pa s.

The results in Figure 3.1 do not rule out transient rheology as a mechanism for reconciling the enigmatic observations of the mean perturbation $\langle \delta H/H \rangle$ over the last 3 Myr and 25 Myr, since distinct viscosity models can be found that fit each data set. However, neither do these results preclude an underestimate of the uncertainty or the presence a bias in the observational constraints based on astronomical tuning. As an example, a factor of two increase in the uncertainty of Figure 3.1A would allow a model with ν_{lm} values near 10^{22} Pa s to fit the observed constraints on both $\langle \delta H/H \rangle_{3Ma}$ and $\langle \delta H/H \rangle_{25Ma}$; although, as dis-

cussed above, there is no guarantee that such a model would simultaneously fit independent convection and GIA data sets. Similarly, if an Earth model could be found that yielded a cancellation of the ice age and convection perturbations to H, then such a model would also need to simultaneously fit the large database of GIA and convection observables that have been used in past inferences of viscosity.

In any case, the results summarized in Figure 3.1 define a rather fundamental enigma in estimates of the Earth's dynamic ellipticity that warrants further attention. A stratigraphic record extending to at least 30 Ma, characterized by significant Milankovitch periodicities and accurate age constraints, would be key to resolving this enigma. Such a record could be compared with geophysical models to decouple the effects of tidal dissipation, which may vary significantly with time (Hüsing et al., 2007), from perturbations in dynamic ellipticity due to GIA and mantle convection. The ultimate resolution of the enigma may lead to a reappraisal of mantle viscosity, a key parameter governing the long-term evolution of the Earth system, or of astronomical calibration or tuning, a methodology that has been used to establish time scales extending through the Cenozoic and into the Mesozoic.

Chapter 4

Low-degree Gravity Harmonics and Modern Climate

Abstract

A comprehensive analysis of satellite data sets (Shepherd et al., 2012) has estimated that the ice sheets of Greenland, West Antarctica, the Antarctic Peninsula and East Antarctica experienced a net mass loss of -100 ± 92 Gt/yr over the period 1992-2000 and -298 ± 58 Gt/yr from 2000-2011, representing an increase of -198 ± 109 Gt/yr between the two epochs. We demonstrate that the time rate of change of the degree-four zonal harmonic of the Earth's gravitational potential, $\dot{J}_4$, provides an independent check on these mass balances that is less sensitive to uncertainties that have contaminated previous analyses of the degree-two harmonic (e.g., ongoing GIA, solid Earth body tides, core-mantle coupling). For the period 2000-2011, the $\dot{J}_4$ signal implied by the ice sheet mass flux cited above is $(3.8 \pm 0.6)^{-11}\mathrm{yr}^{-1}$, while the change in the $\dot{J}_4$ harmonic across the two epochs is $(2.3 \pm 1.1) \times 10^{-11}\mathrm{yr}^{-1}$. In comparison, using satellite laser ranging (SLR) data, we estimate a GIA-corrected $\dot{J}_4$ value of $(3.8 \pm 0.6) \times 10^{-11}\mathrm{yr}^{-1}$ for the epoch 2000-2011, and a change across the two epochs of

This Chapter was published with J. X. Mitrovica, M. G. Sterenborg, and C. Harig in Journal of Climate (2013), Vol. 26, 6535 - 6540.

$(5.3 \pm 1.6) \times 10^{-11}\mathrm{yr}^{-1}$. We conclude that the former supports recent estimates of melting over the last decade, while the latter suggests either that estimated melt rates for the earlier epoch were too high or that the uncertainty associated with the SLR-based inference of $\dot{J}_4$ during the earlier epoch is underestimated.

4.1 Introduction

A recent, combined reanalysis of satellite-based regional altimetry, interferometry and gravimetry data sets (Shepherd et al. 2012, henceforth S2012) has estimated the mass balance of ice sheets covering Greenland (GIS), the Antarctic Peninsula (APIS), West Antarctica (WAIS) and East Antarctica (EAIS) over the period 1992-2011 as well as during various epochs within this two decade time window (Table 4.1). The uncertainties ascribed to these estimates account for the limited and unique time span associated with each of the three space-geodetic techniques, observation errors, and, through modeling, uncertainties in corrections for ice-sheet surface mass balance and glacial isostatic adjustment (GIA). Over the period 2000-2011, for example, the total estimated mass flux from these ice sheets, -298 ± 58 Gt/yr (1-sigma uncertainty), equates to a eustatic sea-level (ESL) rise of 0.83 ± 0.16 mm/yr. (We adopt the term eustatic as the geographically uniform shift in sea level over the oceans that would yield a volume equal to the melt water addition. Gregory et al. (2012) has suggested the term "barystatic" for this quantity.) In this paper we demonstrate that this estimate may be independently tested by invoking the constraint provided by the time rate of change of the zonal harmonic of the Earth's gravitational potential at spherical harmonic degree four, $\dot{J}_4$ (or, alternatively, the trend in the C_{40} Stokes coefficient) (Hofmann-Wellenhof and

Table 4.1: Ice sheet mass balance estimates (Gt yr^{-1}; S2012) and associated J_4 rate ($yr^{-1} \times 10^{-11}$)

Region	1992-2000	2000-11	Change
EAIS	-2 ± 54	26 ± 36	28 ± 65
WAIS	-38 ± 32	-85 ± 22	-47 ± 39
APIS	-8 ± 17	-29 ± 12	-21 ± 21
GIS	-51 ± 65	-211 ± 37	-160 ± 75
Total	-100 ± 92	-298 ± 58	-198 ± 109
J_4 rate	1.0 ± 0.9	2.9 ± 0.6	1.9 ± 1.1

Moritz, 2006).

Estimates of secular trends in the low-degree zonal harmonics of the geopotential based on satellite laser ranging (SLR) have been available for over a quarter of a century, initially at spherical harmonic degree two (Yoder et al., 1983; Rubincam, 1984) and later at higher degrees (Cheng et al., 1989). The first analyses of the $\dot{J}_2$ harmonic interpreted it as being dominated by ongoing GIA (Yoder et al. 1983; Rubincam 1984; Wu and Peltier 1984; Peltier 1983; Yuen and Sabadini 1985; Ivins et al. 1993; Vermeersen et al. 1998), and commonly used the harmonic as a basis for inferring the average viscosity of the lower mantle. Motivated, at least in part, by the growing appreciation of the impact of modern climate change on the Earth's gravitational field, other, generally later, analyses of these harmonics highlighted the potential signal from recent changes in the mass balance of polar ice sheets and mountain glaciers (Sabadini et al., 1988; Mitrovica and Peltier, 1993; James and Ivins, 1997; Trupin and Panfili, 1997). In addition, coupling between the fluid outer core and the overlying mantle has also been identified as a potentially important contributor to the $\dot{J}_2$ harmonic (Fang et al., 1996).

A significant change in the secular trend of the J_2 coefficient in the mid-1990s, as estimated from SLR data (Cox and Chao, 2002), has led to renewed interest in the geophysical

interpretation of this harmonic. Explanations for the observation have included a possible error in the standard geodetic correction for the 18.6 year body tide signal (Benjamin et al., 2006), a change in the dynamics of the El-Niño-Southern Oscillation (Cheng and Tapley, 2004; Marcus et al., 2009) and increased melting of either mountain glaciers (Marcus et al., 2009; Dickey et al., 2002) or polar ice sheets (Nerem and Wahr, 2011).

The spherical harmonic basis function at degree two and order zero has the same sign in both high northern and southern latitudes. As such, the $\dot{J}_2$ datum provides an integrated measure of the combined (recent) mass balance of the GIS and AIS (Ivins et al., 1993; Mitrovica and Peltier, 1993). In contrast, basis functions associated with odd harmonics have a different sign near the north and south poles, and they thus provide a measure of the difference in mass balance of the two polar ice sheets. Since the mass balance of the AIS and GIS is of comparable magnitude, this difference will be sensitive to their relative sizes. However, while the integrative nature of the J_2 harmonic is an advantage over the odd harmonics for inferring total polar ice sheet mass changes, there are other sources of uncertainty that decrease with higher spherical harmonic degrees (e.g. 18.6 year body tide, core-mantle coupling, etc.). Consequently, the optimal spectral component to examine for estimating net polar mass change is an even harmonic that is of low enough degree that the basis function integrates over the region of interest (in this case the polar ice sheets) but is of high enough degree to reduce the contribution from non-melt signals.

In this regard, the $\dot{J}_4$ harmonic, which has been overlooked in recent geodetic analyses of climate signals, provides a potentially more rigorous constraint on integrated polar ice sheet mass balance. The $\dot{J}_4$ signal due to recent mass loss from either the GIS or AIS should only

be ∼10% smaller than the analogous signal in the $\dot{J}_2$ harmonic (Ivins et al., 1993; Mitrovica and Peltier, 1993), and hence it should be significant and observable (as we demonstrate below). Furthermore, the $\dot{J}_4$ datum avoids many of the various complications that arise in analyzing the $\dot{J}_2$ harmonic. For example, the $\dot{J}_4$ signal associated with the 18.6 year body tide and core-mantle coupling will be about three orders of magnitude smaller than the analogous signal in $\dot{J}_2$.

The $\dot{J}_2$ and $\dot{J}_4$ harmonics will both have a significant contribution from ongoing GIA and any effort to estimate recent mass flux from polar ice sheets based upon these harmonics must address the uncertainty associated with this signal. In the analysis described below, we implement two strategies for this purpose. The first is to consider observed changes in the rates of the harmonics, for example from the epoch 1992-2000 relative to the epoch 2000-2011 (Table 4.1, column 4). This will remove any sensitivity to the GIA process because the change in the GIA-induced rate will be negligible over the two decade time window of the present analysis. A second strategy for dealing with the contamination of the $\dot{J}_4$ harmonic due to GIA, which we turn to next, is forward modeling of the GIA process.

4.2 Analysis and results

4.2.1 GIA predictions

The results in Figure 4.1 show the predicted GIA-induced signal in $\dot{J}_2$ and $\dot{J}_4$ as a function of the adopted lower mantle viscosity of the Earth model. The calculations are based on spherically symmetric, Maxwell viscoelastic Earth models (Peltier 1974) with density and elastic structure given by the seismic model PREM (Dziewonski and Anderson, 1981). The

lithospheric thickness and upper mantle viscosity are set to 70 km and 5×10^{20} Pa s, respectively. Our predictions of the long-wavelength zonal harmonics are insensitive to the former and in the calculations below we explicitly investigate the sensitivity to the latter. The predictions adopt the ICE-5G model for the evolution of ice thickness over the last glacial cycle (Peltier, 2004) and they incorporate a gravitationally self-consistent sea-level theory (Kendall et al., 2005). This theory outputs the present-day rate of change of relative sea level and sea-surface height; the spherical harmonic coefficients of the latter are proportional to the rates of change of the Stokes coefficients (Mitrovica and Peltier, 1993).

In addition to the total GIA-induced perturbation in each harmonic (solid lines, Figure 4.1), we decompose the perturbation into contributions from the GIS, AIS and all other ice sheets included in the ICE-5G inventory (e.g., Laurentia, Fennoscandia, etc.). The results indicate that while ice sheets other than the AIS and GIS dominate the GIA-induced signal in the $\dot{J}_2$ harmonic, the signal associated with AIS evolution over the last glacial cycle dominates the GIA prediction of the $\dot{J}_4$ harmonic. Moreover, for lower mantle viscosities greater than $\sim 3 \times 10^{21}$ Pa s, which is a hard lower bound for ice-age-based inferences (Nakada and Lambeck, 1989; Lambeck et al., 1998; Mitrovica and Forte, 2004; Peltier, 2004), the GIA-induced $\dot{J}_4$ signal driven by ice sheets other than the AIS is relatively insensitive to uncertainties in the radial profile of mantle viscosity. We have verified that this insensitivity extends to predictions based on Earth models in which the upper mantle viscosity is varied from $3 - 10 \times 10^{20}$ Pa s (Figure 4.2) and an independent ice history (Fleming and Lambeck, 2004). These $\dot{J}_4$ predictions are also insensitive to the adopted lithospheric thickness.

The decomposition in Figure 4.1 highlights another important advantage of using the

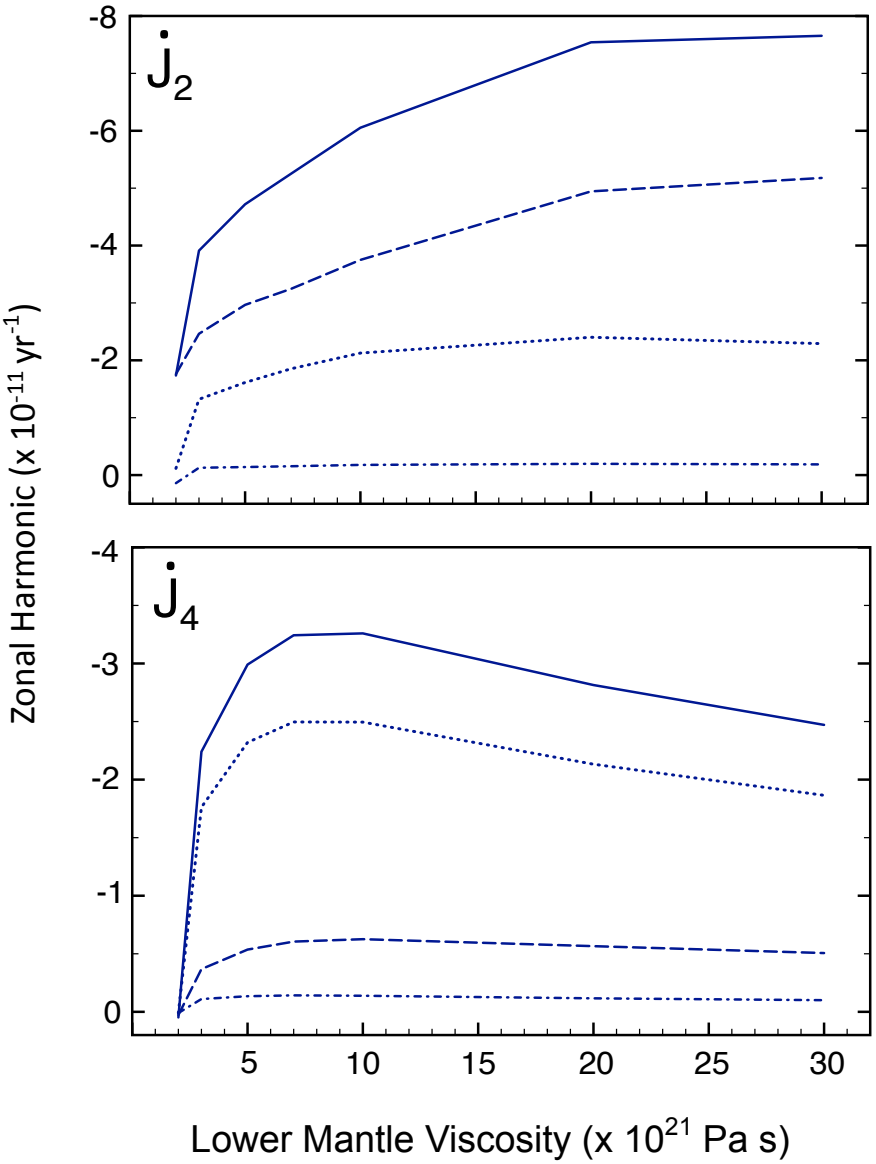

Figure 4.1: Components of present-day GIA contributions to $\dot{J}_2$ and $\dot{J}_4$. Predictions of the present-day time rate of change of the (top) $\dot{J}_2$ and (bottom) $\dot{J}_4$ zonal harmonics of Earth's geopotential due to ongoing GIA as a function of the lower-mantle viscosity of the Earth model. In these calculations, the elastic lithospheric thickness and upper-mantle viscosity are set to 70 km and 5×10^{20}Pa s, respectively. The solid line on each frame represents the total GIA-induced perturbation computed using the ICE-5G (Peltier, 2004) ice sheet model for the last glacial cycle. The dotted and dashed-dotted lines represent the contributions to this total associated with the Antarctic and Greenland components of the ICE-5G ice history, respectively, whereas the dashed line is the contribution from the remaining ice cover (i.e., the solid line equals the sum of the three other lines).

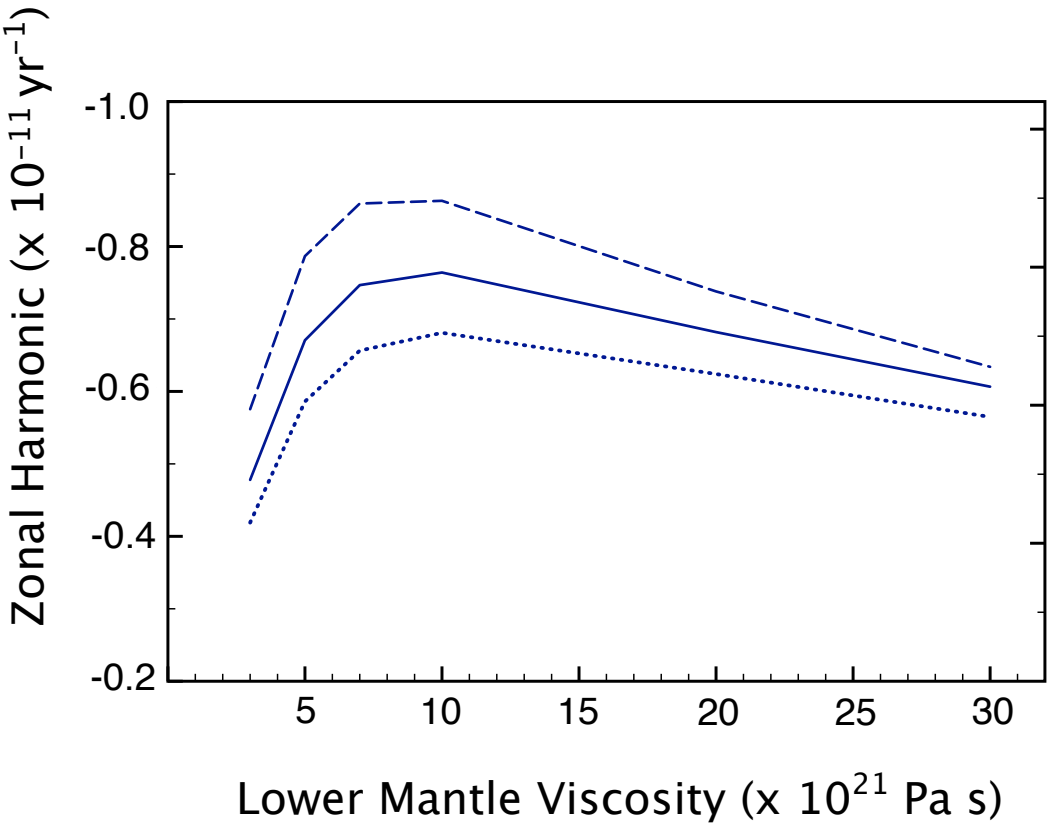

Figure 4.2: Dependence of present-day GIA contributions to $\dot{J}_4$ on lower-mantle viscosity for three different values of upper-mantle viscosity. Predictions of the present-day time rate of change of the $\dot{J}_4$ zonal harmonic of Earths geopotential due to ongoing GIA as a function of the lower-mantle viscosity of the earth model. As in Figure 4.1, these predictions are based on the ICE-5G ice history (Peltier, 2004) for the last glacial cycle, but with the Antarctic component of the ice model removed. The dashed, solid, and dotted lines join simulations in which the upper-mantle viscosity is set to 10^{21}, 5×10^{20}, and 3×10^{20} Pa s, respectively. All calculations adopt an elastic lithospheric thickness of 70 km.

observed $\dot{J}_4$ harmonic, rather than the $\dot{J}_2$ harmonic, as a basis for estimating recent polar ice sheet mass flux. In particular, any uncertainty in the GIA correction to $\dot{J}_4$ is largely isolated to the contribution to the GIA signal associated with the AIS. In this regard, GIA models for Antarctica over the last glacial cycle have recently been improved, relative to earlier models such as ICE-5G/VM2 (Peltier, 2004), by combining numerical ice sheet models with geological observations of ice extent, local relative sea-level histories and GPS-derived uplift rates (Whitehouse et al., 2012). In adopting the $\dot{J}_4$ harmonic to estimate recent polar mass flux, a second strategy for dealing with the GIA signal is to use the correction generated by this new, improved class of ice age AIS models.

We begin by focusing on the period 2000-2011 and compute a GIA correction based on a combination of our GIA modeling and the W12a Antarctic GIA model (Whitehouse et al., 2012). The results in Figure 4.2 indicate that the GIA contribution to $\dot{J}_4$ from sources other than the Antarctic falls within the (conservative) range $(-0.7 \pm 0.2) \pm 10^{-11}\mathrm{yr}^{-1}$. Moreover, using the upper and lower bound estimates of the W12a model (Whitehouse et al., 2012) yields an Antarctic GIA contribution to $\dot{J}_4$ of $(-0.96 \pm 0.14) \times 10^{-11}\mathrm{yr}^{-1}$. Thus, we estimate the total GIA contribution to be $(-1.7 \pm 0.2) \times 10^{-11}\mathrm{yr}^{-1}$. We analyzed the SLR-derived times series for J_4 over the time periods 1992-2000 and 2000-2011 (Figure 4.3). Correcting the observed trend in J_4 during each of these epochs using the total GIA signal yields residual trends of $(-1.6 \pm 1.5) \times 10^{-11}\mathrm{yr}^{-1}$ and $(3.7 \pm 0.6) \times 10^{-11}\mathrm{yr}^{-1}$, respectively.

We note that the Antarctic ice volume change in the W12a model (Whitehouse et al., 2012) is significantly smaller than in the ICE-5G history. The difference amounts to approximately 10 m of equivalent eustatic sea level rise, or $\sim$10% of the total non-Antarctic

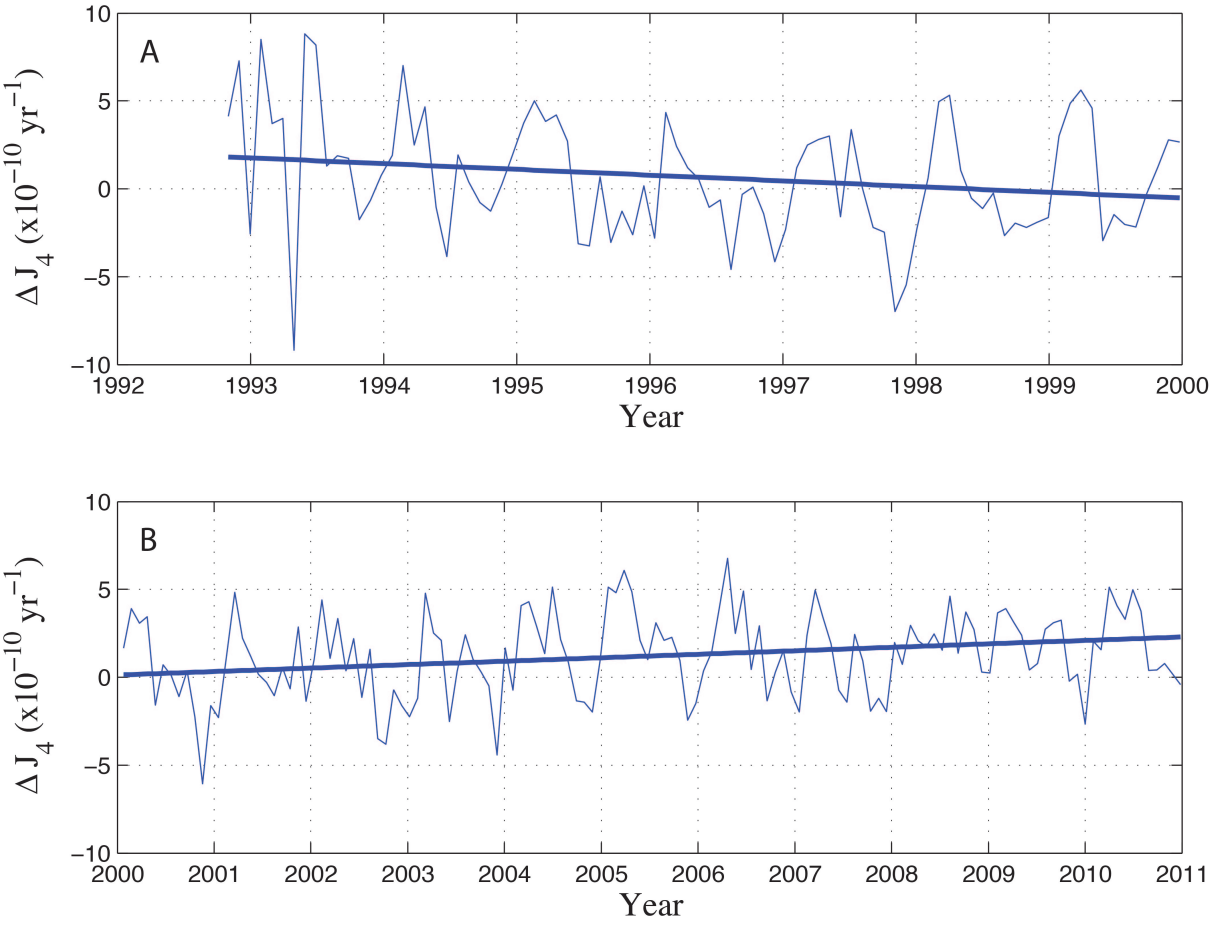

Figure 4.3: SLR-estimated $\dot{J}_4$ time series. Time series of the J_4 zonal harmonic of Earths geopotential inferred from SLR data (a) from 1992 to 2000 and (b) from 2000 to 2011. The records within both intervals were fit to models containing constant and linear terms in addition to sinusoids representing the annual and semiannual components of the signal. The J_4 trends within each of these epochs, computed using an unweighted least squares linear regression (superimposed on each frame), were $(-3.3 \pm 1.5) \times 10^{-11}\mathrm{yr}^{-1}$ and $(2.0 \pm 0.5) \times 10^{-11}\mathrm{yr}^{-1}$, respectively. Thus, the change in the trend across these two time periods was $(5.3 \pm 1.6) \times 10^{-11}\mathrm{yr}^{-1}$.

ice volume in ICE-5G. This reduction would have to be compensated by an increase in the excess volume of northern hemisphere ice relative to ICE-5G in order to maintain a fit to far-field relative sea-level records Austermann et al. (2013). This suggests that the amplitude of our computed non-Antarctic GIA contribution (Figure 4.2) will be biased low by 10%. Accounting for this effect, yields GIA-corrected trends in J_4 of $(-1.5 \pm 1.5) \times 10^{-11}\text{yr}^{-1}$ and $(3.8 \pm 0.6) \times 10^{-11}\text{yr}^{-1}$ for the epochs 1992-2000 and 2000-2011, respectively.

4.2.2 Polar mass change contribution to J_4

We next turn to the estimate of polar ice sheet mass balance based on the comprehensive S2012 analysis of satellite-based measurements (Shepherd et al., 2012) (Table 4.1). What signal in $\dot{J}_4$ does this level of modern melting imply? To answer this, we adopted a special, elastic case of our sea-level software to compute the $\dot{J}_4$ signal associated with uniform melting over 1) EAIS, 2) WAIS, 3) APIS, and 4) GIS (Table 4.2). The calculations are normalized so that they represent perturbations to the J_4 trend per mm/yr of ESL rise. Using these results, we converted the total mass flux estimates in Table 4.1 into a $\dot{J}_4$ signal (last row, Table 4.1). For the epoch 2000-2011, we obtain the range $(2.9 \pm 0.6) \times 10^{-11}\text{yr}^{-1}$. A final, significant contribution to the J_4 trend is associated with melting of mountain glaciers. A tabulation of mountain glacier mass balance by Jacob et al. (2012), based on GRACE gravity data, covers the period 2003-2010. Using this database, we computed a J_4 trend of $0.9 \times 10^{-11}\text{yr}^{-1}$. If we assume that this rate is applicable to the 2000-2011 epoch adopted in Table 4.1, we can augment the above estimate ($(2.9 \pm 0.6) \times 10^{-11}\text{yr}^{-1}$) to include the mountain glacier signal; in particular, we arrive at an estimate of $(3.8 \pm 0.6) \times 10^{-11}\text{yr}^{-1}$. The consistency between this estimate and our GIA-corrected SLR-derived trend, $(3.8 \pm 0.6) \times 10^{-11}\text{yr}^{-1}$,

Table 4.2: The J_4 rate in a given melt region normalized to 1 mm yr^{-1} ESL rise (yr$^{-1} \times 10^{-11}$)

Melt region	J_4 rate
EAIS	3.7
WAIS	4.0
APIS	2.9
GIS	3.4

provides independent support for recent estimates of polar ice sheet (Shepherd et al., 2012) and mountain glacier Jacob et al. (2012) mass flux over the last decade.

Alternatively, in inferring polar ice sheet mass balance we can avoid entirely the contaminating effect of GIA by considering the change in the trend of the J_4 harmonic from 1992-2000 to 2000-2011 (i.e., the first strategy for dealing with GIA discussed above). From Table 4.1, the change in polar ice mass flux across these time periods inferred in the S2012 study (Shepherd et al., 2012) maps into a change in the $\dot{J}_4$ signal of $(1.9 \pm 1.1) \times 10^{-11}\text{yr}^{-1}$. Taking into account a change in the mountain glacier signal using the tabulations of Kaser et al. (2006) for the first epoch and (as above) Jacob et al. (2012) for the second epoch, raises this value to $(2.3 \pm 1.1) \times 10^{-11}\text{yr}^{-1}$. As noted above, our direct, SLR-derived estimate of the change in trend is $(5.3 \pm 1.6) \times 10^{-11}\text{yr}^{-1}$. This analysis suggests either that estimates of melt rates during the earlier epoch are too high, and/or that the uncertainty in the SLR-derived change in the $\dot{J}_4$ signal has been underestimated. In regard to the latter, we note that the observed trend across the earlier epoch ($(-3.3 \pm 1.5) \times 10^{-11}\text{yr}^{-1}$ as cited in the caption to Figure 4.3) is sensitive to the start time of the epoch.

4.3 Conclusions

We have demonstrated that estimates of net polar ice sheet mass balance may be independently tested by invoking the long-neglected constraint associated with the rate of change of the degree four zonal harmonic of the Earth's potential. The $\dot{J}_4$ harmonic is relatively insensitive to the uncertainties associated with signals from the 18.6 year Earth tide and core-mantle coupling that must be accounted for in analyses of the $\dot{J}_2$ harmonic. Analyses of the $\dot{J}_4$ harmonic must, however, address the potentially significant signal from GIA, either by considering a change in trend across two epochs, rather than the absolute value of the harmonic, or through numerical modeling. In regard to the latter, we have shown that the dominant GIA contribution to the $\dot{J}_4$ is associated with the Antarctic Ice Sheet, and thus the uncertainty in the GIA correction can be reduced significantly by adopting recent, well-constrained models of Antarctic GIA. In any event, our application of this approach indicates that the J_4 trend supports recent inferences of increased melting from polar ice sheets and mountain glaciers over the last decade. This demonstrates that analyses of the $\dot{J}_4$ harmonic can play an important role in advancing our understanding of ice sheet stability in a progressively warming world.

Chapter 5

A Bias in Estimates of GRACE Ice Mass Loss due to Sea Level Variations

Abstract

Over the last decade, measurements of the geopotential from the GRACE satellites have been used to infer modern ice mass changes from the polar ice sheets and glaciers. However, these estimates have not considered the effect that the sea-level change associated with the ice melt, which will also affect the geopotential, can have on the ice flux estimates. The contamination from this effect is sensitive to the geometry of the ice melt and the characteristics of the adopted spatial averaging filter. Over the Antarctic Peninsula we conclude that GRACE-based estimates of mass change are overestimating the ice loss by up to 9% for filter radii of less than 500 km.

This Chapter was published in a different form as: Sterenborg, M. G., E. Morrow, and J. X. Mitrovica (2012): Bias in GRACE estimates of ice mass change due to accompanying sea-level change, Journal of Geodesy, Vol. 87, 387 - 392.

5.1 Introduction

The Gravity Recovery and Climate Experiment (GRACE) has provided useful insights into large-scale gravity changes within the Earth since the satellites were launched in 2002. Examples of processes that GRACE data have been used to examine include ocean mass variability (Chambers et al., 2004), the on-going glacial isostatic adjustment from the melting of the Late Pleistoscene ice sheets (Tamisiea et al., 2007), earthquakes (Han and Simons, 2008) and the continuous transport of water within and between continental hydrological basins and the oceans (Tapley et al., 2004; Wahr et al., 2004; Rowlands et al., 2005). Most notably, GRACE has provided important and novel integrated constraints on ice sheet mass fluxes (Luthcke et al., 2006; Velicogna and Wahr, 2006a; Chen et al., 2008; Ivins et al., 2011; Jacob et al., 2012).

The GRACE products, generated for example by the Center for Space Research (Tapley et al., 2004), are monthly averages of the global geopotential field. These averages are provided in the form of coefficients of spherical harmonic coefficients representing a decomposition to degree 60, which corresponds to a length scale of several hundred kilometers (Jeans, 1923). In the past, solutions were provided (e.g., offered by GFZ - Helmholtz Centre Potsdam) that represented spectral decompositions to higher degree and at a higher frequency and sampling, however the higher degree solutions have large errors and are not typically used.

Even with the truncation of the spherical harmonic decomposition to degree 60, the variance of the solution increases with the spherical harmonic degree (Swenson and Wahr, 2006; Wahr et al., 2006). This variance is reduced by spatially averaging the estimated

surface mass anomaly over the region of interest, for example over a hydrological basin or ice sheet. Computationally, the region is defined by an exact averaging mask with values of 1 and 0 ascribed to areas within and outside the region, respectively. In the case of an ice sheet, this exact averaging mask would include either some subregion of the ice sheet, and exclude the remaining ice sectors and the surrounding ocean. In practice, progressively larger errors in the GRACE fields with increasing harmonic degree are attenuated by smoothing the averaging mask with a low pass filter, often a Gaussian filter specified by a desired smoothing radius (Swenson and Wahr, 2002). However, the reduction of resolution by the low pass filter extends the averaging kernel into regions adjacent to the specific region of interest and thus the signal outside of the desired region "leaks" into the regional average. This basic averaging methodology has been used to estimate mass changes within both the Greenland (Velicogna and Wahr, 2006a) and Antarctic (Velicogna and Wahr, 2006b) Ice Sheets, though the adopted Gaussian filters often extend the averaging beyond the ice margins. Therefore, estimates of mass change attributed to the changing ice sheets will represent a combination of mass change directly due to the ice melt and any nearby sea level changes.

As described in Chapter 2, a rapidly melting, grounded ice sheet will drive a migration of water away from the region of melt due to both a decrease in the gravitational attraction between the ocean and ice, and uplift of the crust associated with the unloading (Gomez et al., 2010; Riva et al., 2010). The gravitational effect on local sea level has not been accounted for in GRACE-based analyses of ice mass change, and therefore ice-loss estimates may have been systematically overestimated. We note that the sampling of nearby ocean mass changes has been discussed as an error source in previous estimates of ice mass balance,

but the systematic bias associated with water migration away from the melting ice sheet has not previously been considered.

It is important to note that this systematic bias will impact any ice change estimate based upon GRACE products. A similar bias has been identified in hydrological mass transport studies for basins located near oceans (Tamisiea et al., 2010). The goal of the present study is to evaluate the level of bias introduced in estimates of ice mass changes that have been derived by analyzing GRACE data using the Gaussian filter smoothing method.

5.2 Method

To investigate the bias described above, we generate synthetic GRACE solutions represented by geopotential maps. We focus on melt from the Antarctic Peninsula (Figure 5.1) as it has been identified in GRACE analyses as a region of recent significant melt (Chen et al., 2008) and because it is a relatively narrow peninsula with wide ocean expanses on either side. The use of low pass filters with the radii typically used in such analyses (on the order of several hundred kilometers) will clearly sample a large area of the surrounding ocean. Figure 5.1A shows an example mask used in specifying the region of interest over the Antarctic Peninsula. Figure 5.1A, B, and C show the mask after convolution with Gaussian filters of radii 200 km, 300 km and 500 km, respectively. Note that for even the smallest filter radius of 300 km, significant leakage of averaging kernel into the surrounding ocean is evident.

To evaluate the impact on ice mass estimates of the sea-level change associated with the localized melt, we compute two synthetic geopotential anomaly maps: the first incorporates ice mass loss on the Antarctic Peninsula and the associated sea-level change, and the second

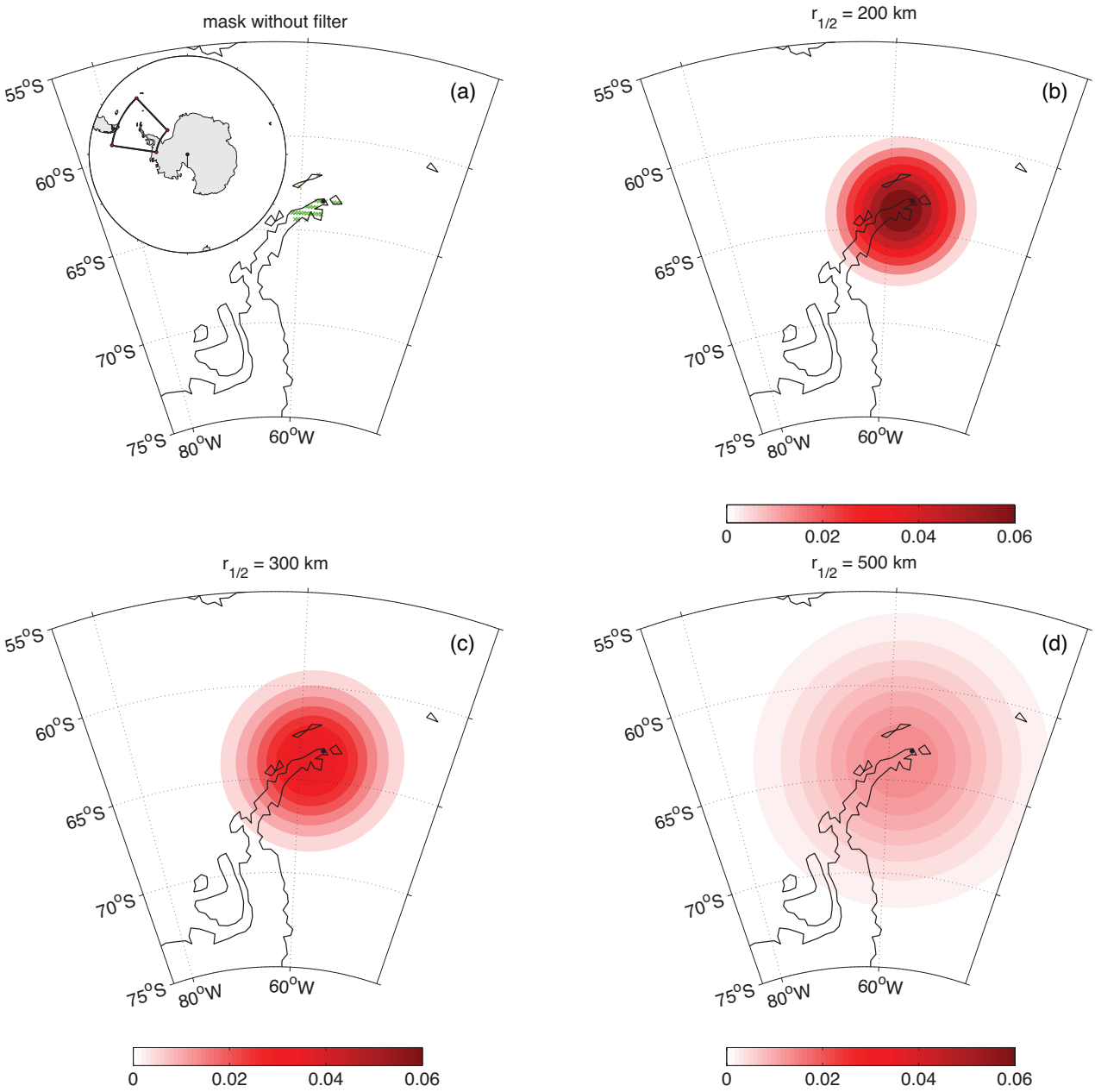

Figure 5.1: An example of the geometry associated with the calculations of a synthetic geopotential anomaly and the Gaussian smoothing applied to this anomaly. (a) The green hatched region shows an example of a land mask that is defined as the region interior to both coastlines and within a distance of 200km from a point at the tip of the Antarctic Peninsula (black dot). (b) - (d) The land mask in Frame (a) after convolution with Gaussian filters of radii (half-width $r_{1/2}$) of 200, 300 and 500km, respectively. The shading indicates the magnitude of the convolved land mask.

includes changes in the geopotential due to ice mass changes alone. The difference between the fields represents the total perturbations in the geopotential due to the effects other than the ice melting, including the water migration described above and the feedback on sea level of Earth rotation changes.

The geopotential anomaly is computed by solving a 1-D, gravitationally self-consistent sea-level equation that accounts for shoreline migration, changes in the extent of grounded, marine-based ice and the feedback of rotation into sea level (Milne and Mitrovica, 1998; Kendall et al., 2005). The computations are performed using the elastic-case of the pseudo-spectral sea-level solver (Kendall et al., 2005) as the time scales associated with the rapid melt of the ice sheet are much less than the 300 - 500 year Maxwell time of the viscoelastic Earth. The geometry of the melt is assumed to be uniform over the specified region of interest. The geopotential fields are computed to degree and order 512 then truncated to degree 60 for consistency with the Center for Space Research (University of Texas at Austin) GRACE solutions.

Figure 5.2 shows the difference between the complete and ice-only geoid height anomaly predictions for the cases of melt that only covers the tip of the Antarctic Peninsula (Frame A) and melt that covers the entirety of the peninsula (Frame B). The anomalies are dimensionless as they are presented normalized to the equivalent eustatic sea-level change associated with the melt. In the case of short time scales (i.e., forcings much less than the Maxwell time), the geoid height perturbation is a linear function of the forcing and as such the anomaly maps can be scaled by the equivalent eustatic change of any ice mass flux that has the same melt geometry. Frames C and D of Figure 5.2 show the equivalent water thickness associated

with the differenced geoid height anomaly maps, again normalized to the equivalent eustatic change in sea level (Swenson and Wahr, 2002).

Figure 5.2 shows that along the coast line adjacent to the melt region there is a significant lowering in the height of the geoid due to the regional dominance of the water migration (which lowers the geoid) over the impact of the gravitational field associated with the elastic rebound of the lithosphere (which raises the geoid). The smoothing of the GRACE solutions when computing the regional averages samples the geopotential in the region of this water migration, contaminating the estimates of ice mass loss. The degree of contamination is a function of the radius of the smoothing filter employed in the averaging. Additionally, the geometry of the melt is uncertain and masks are typically used that are assumed to completely encompass the melt region. To investigate the impact of these assumptions on biases introduced into the regional averages of ice mass change, we vary the size of both the smoothing radii and the mask coverage while computing the average over the region of interest using the perturbations of the geoid not directly related to the ice mass change. We also investigate the impact of the size of the actual melt on the bias by varying the size of the melt zone.

For clarity, we define the bias as the mass loss inferred with the 'complete' geopotential anomaly minus the inference from the 'ice-only' geopotential anomaly, all quoted with respect to the 'ice-only' estimate. Therefore, a positive value of the bias refers to an overestimation of the ice mass. Additionally, by reporting the bias as a value relative to the 'ice-only' estimate, we need not consider the scaling that is typically applied to account for the filter attenuation associated with the Gaussian smoothing (Velicogna and Wahr, 2006a).

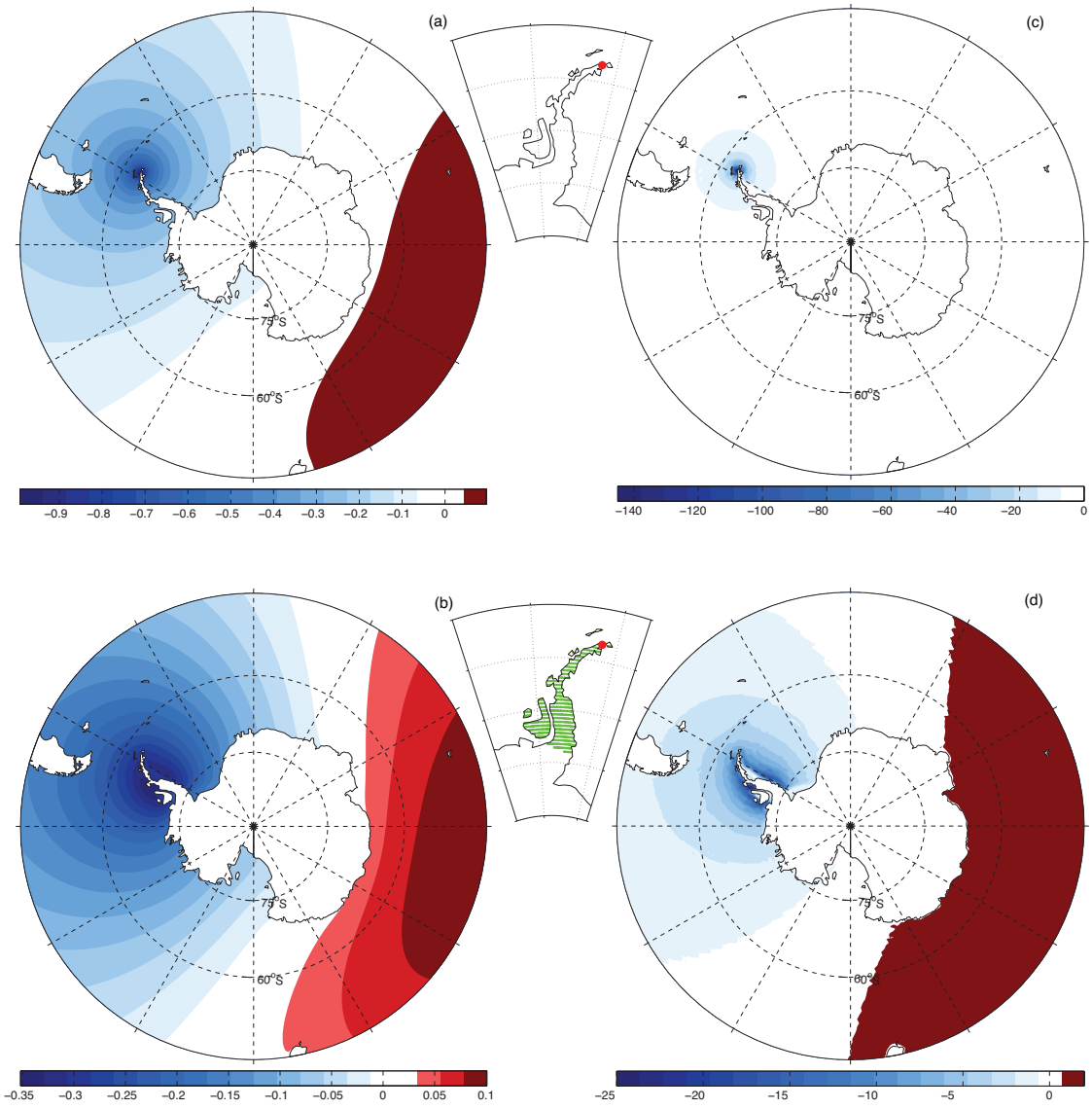

Figure 5.2: Geoid and mass variation differences between the 'complete' and 'ice-only' synthetic calculations. Frame (a) shows the difference between the geoid height anomaly predicted using the complete ice-ocean mass transfer and loading-induced deformation for melt occurring on the tip of the Antarctic Peninsula (see inset between Frames (a) and (c), the red dot approximately covers the entire melt area), and the prediction in the case where only the signal associated with the ice loss is included. The geoid height anomaly difference is normalized by the equivalent globally uniform sea-level change associated with the ice-melt event, and can be scaled to consider arbitrary melt rates with the same geometry. Frame (b) shows a similarly normalized geoid height anomaly difference for a melt region that covers the entire Peninsula (see inset between Frames (b) and (d)). Frames (c) and (d) show the mass variations, expressed in equivalent water thickness, associated with the differenced geoid height anomaly in Frame (a) and (b), respectively. These mass variations maintain the same normalization as the geoid anomaly plots and can therefore also be scaled to consider any melt rate of the same geometry.

5.3 Results and Discussion

Figure 5.3 shows the bias as a function of the melt area and the radius of the Gaussian low pass filter. The melt area is as defined in Figure 5.2, where the melt region begins as a delta function at the tip of the peninsula and then systematically increases to encompass the entirety of the Antarctic Peninsula. The radii of the Gaussian low pass filters range from 200 km to 750 km. The 200 km radius lower bound is close to but below the resolution limit of the GRACE solutions.

The largest bias of $\sim 6.5\%$ is found in the lower right corner of the contour map for the case of a localized melt region and a filter radius at the upper limit of those studied. With a decreasing filter radius, a smaller area of the ocean is sampled by the filter and the contaminating signal from the associated local sea-level fall is monotonically reduced. As the melt area increases, the bias also decreases because the ocean area sampled becomes a proportionately smaller region of the total integrated area under the mask. Typical GRACE analyses use Gaussian filter radii of less than 500 km which suggests an upper bound bias of $\sim 5\%$ in estimates of the ice mass change.

When constructing averaging masks to investigate specific regions of interest, the extent of the actual melt region is typically not known and as such it is unlikely that the averaging mask will exactly match the geometry of the melt. Accordingly, we next examine the impact of the mismatch between the geometries of the filter and the melt by computing the bias that results from a range of mask areas and filter radii for a constant melt geometry. Figure 5.4 shows a contour plot of the bias for a small melt area located at the tip of the Antarctic Peninsula. The smallest bias occurs when both the mask area and the filter radius are small

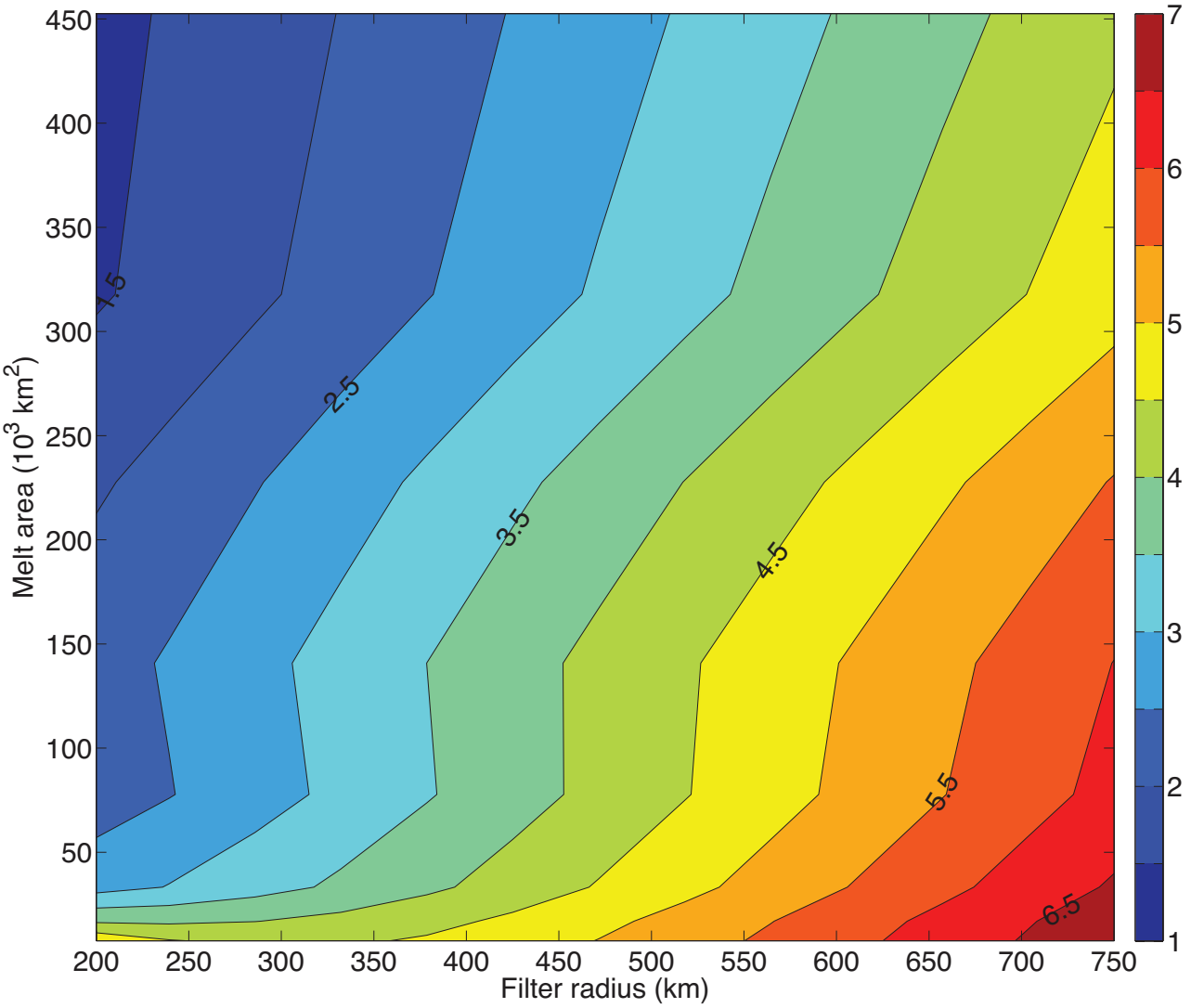

Figure 5.3: Bias (in %) in the estimation of ice mass change as a function of Gaussian smoothing filter radius and the melt area within the Antarctic Peninsula.

and closely fit the melt geometry. As before, increasing the filter radius extends the region averaged by the filter deeper into the adjacent ocean resulting in more sampling of the local sea-level changes associated with the melt. Increasing the size of the mask area kernel also results in a greater sampling of the ocean, though the increased sampling is located along the coastlines rather than the deep ocean. However, the coastlines are where the migrating of water is strongest, so the signal can be pronounced. For filter radii less than 500 km, the upper bound on the bias is $\sim 9\%$.

5.4 Discussion and Conclusions

While computing the regional averages through an exact mask and low pass filter is one method of localizing the gravity signal to a region of interest, another method that is discussed in the literature is the use of mass concentrations or 'mascons' e.g. (Rowlands et al., 2005; Ivins et al., 2011; Jacob et al., 2012). While the mascon approach has a better spatial resolution than the low pass filter approach discussed above, a bias associated with sea-level changes still contaminates the melt signal when the mascons overlap the ocean near the melt region. Smaller mascons can be used to reduce this overlap, but the minimum size is fundamentally limited by the resolution of the GRACE solutions. Moreover, using increasingly smaller mascons reduces the accuracy of the solution as the inversion requires the use of the more poorly determined higher harmonic degrees of the GRACE products (Jacob et al., 2012). Spherical Slepian functions which simultaneously minimize the spatial and spectral leakage of contaminating signals outside of the region of interest also have recently been used to compute the regional averages of mass change and have shown better localization

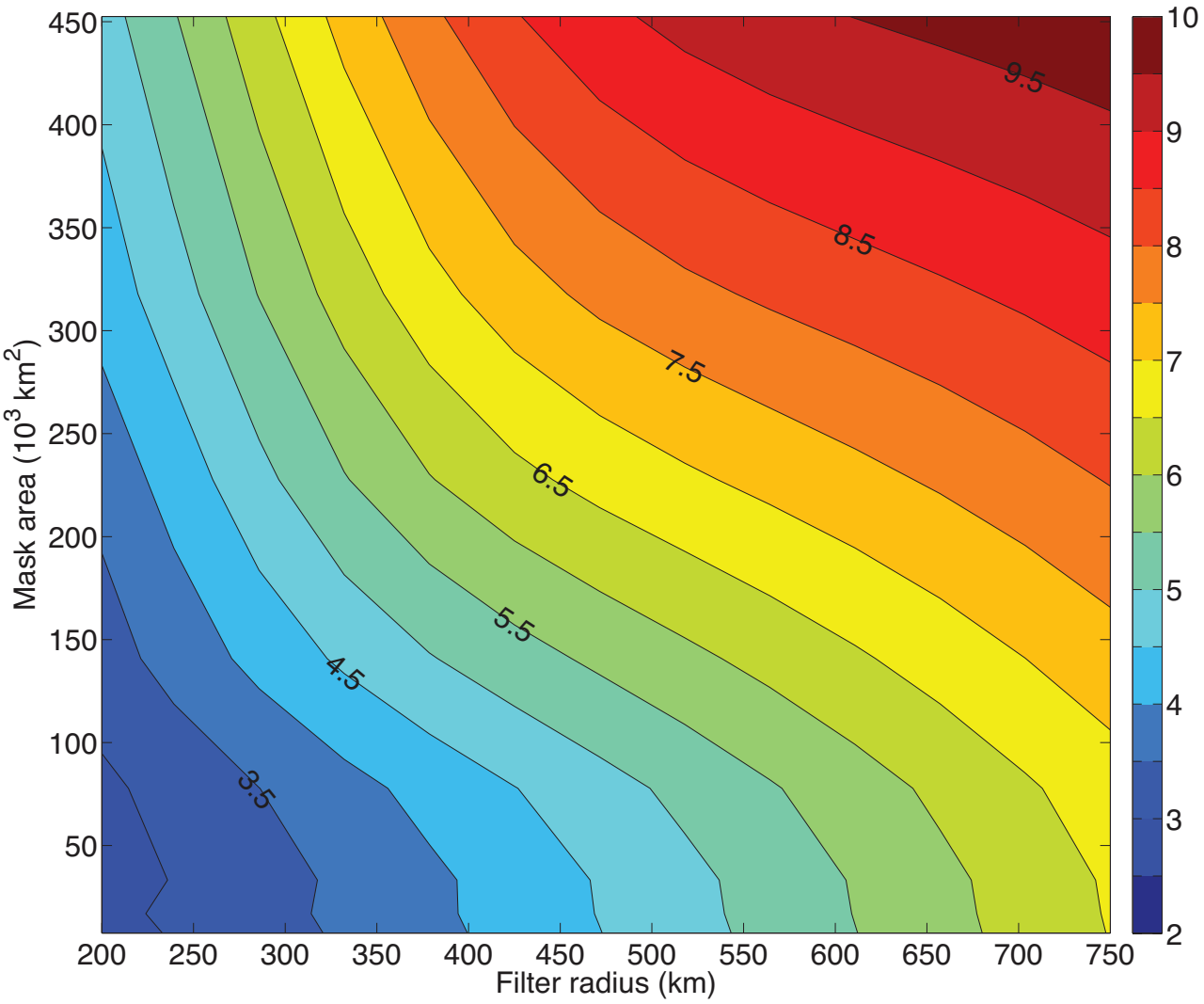

Figure 5.4: Bias (in %) in the estimation of ice mass change as a function of Gaussian smoothing filter radius and the mask area within the Antarctic Peninsula for a specific melt geometry (see text and Figure 5.1).

than Gaussian filters (Simons and Dahlen, 2006; Han and Simons, 2008). However, for the Antarctic Peninsula this approach is still limited by the resolution of the GRACE data. In this case, truncation at spherical harmonic degree 60 corresponding to a wavelength of 600 km, extends well beyond the $\sim$ 300 km width of the peninsula at its widest cross-section.

Estimates of ice mass change from GRACE solutions of the geopotential contain a systematic bias due to neglect of the sea-level changes that accompany rapid ice melt. The level of the bias is a function of the actual ice melt geometry, the assumed ice melt geometry, and the characteristics of the low pass filter used to compute the regional averages. The bias increases for smaller melt zones, larger mask areas, and larger filter smoothing radii or cut-off wavelengths. On the Antarctic Peninsula, biases from this effect range between 1.5 - 10.5%. For filter radii of less than 500 km with a known melt geometry, the bias is limited to 5%. For unknown melt geometries this bias can reach close to 9%.

Chapter 6

An Application of Gaussian Process Regression to Modern Sea-Level Change

Abstract

We develop and apply a Gaussian process regression approach to decompose estimates of the global sea level field into its constituent components. We estimate time series of the melt contributions to sea level from the Greenland Ice Sheet and Alaskan and Western Canadian/US glaciers that have mean values which are in good agreement with previous estimates. We also find a mean global mean sea level (GMSL) rate over the 20th century of 1.3 ± 0.2 mm/yr, a rate that is 24% lower than previous estimates indicating that the methodologies adopted in earlier studies have introduced biases in the estimates of GMSL. Finally, our analysis suggests a preferred GIA model corresponds to a lithospheric thickness of 100 km, an upper mantle viscosity of 0.5×10^{21} Pas and a lower mantle viscosity of 5×10^{21} Pa s.

6.1 Introduction

Changes in sea level have a significant impact on the world's coastal populations. To improve projections of sea-level change over the next century it is important to constrain the spatio-temporal variability in sea-level changes during the last century and the underlying mechanisms responsible for these changes. Within the budget for global mean sea level change (GMSL) there are two primary constituents: the expansion of the water due to heat content changes (e.g. Antonov et al., 2005; Lombard et al., 2005; Ishii et al., 2006; Ishii and Kimoto, 2009), and the addition of water into the ocean from the melting of land-based ice complexes (Church and White, 2011; Gregory et al., 2012, e.g.). On a regional scale, sea level is affected by the on-going glacial isostatic adjustment (GIA) of the Earth to the melting of the Late Pleistocene ice sheets (e.g. Clark et al., 1978; Mitrovica and Peltier, 1991; Milne and Mitrovica, 2008), ocean dynamics, and non-climatic factors such as tectonics and ground subsidence. Each of the processes, including on-going GIA, have distinct spatial and temporal patterns, and those can be used, in principle, to infer the various contributions. For example, the rapid melting of an individual ice sheet or mountain glacier generates a pattern of sea-level change that is distinct from any other ice melt event, an from signals due to GIA, ocean dynamics or non-climatic processes. Consequently, these unique patterns, or fingerprints, can form the basis of an estimation procedure for decomposing global sea level into its source contributions over the 20th century.

Estimating melt source contributions from sea-level change has become a standard methodology over the past decade (e.g. Mitrovica et al., 2001; Plag and Juttner, 2001; Plag, 2006; Hay et al., 2012). Mitrovica et al. (2001) used spatial fingerprints to estimate the melt

contributions of Greenland over the past century, while Gregory et al. (2012) compared the temporal characteristics of each contribution to estimates of GMSL in the effort to close the so-called sea-level budget for the last century. Ideally, using information available in both the spatial geometries and temporal variability could provide a better estimate of the contributions to sea-level rise than each dimension in isolation.

Previous estimates of the sources of 20th century sea-level change have typically used a regression framework that relied on the assumption of a linear model and the stationarity and independence of the noise processes in both the observations and the dynamics. However, recent suggestions of an acceleration in melt contributions to sea level (e.g. Velicogna and Wahr, 2006b; Shepherd et al., 2012) may make this assumption unrealistic. In this regard, recursive regression techniques have been developed (Hay et al., 2012) that permit changes in the assumed noise characteristics and require weaker assumptions concerning the underlying model for the melt source contributions. However, in accounting for the GIA and thermal contributions to sea-level changes, the recursive approaches require the true GIA and heat content signals to be linear combinations of the models considered. Therefore, the estimation of non-melt signals may benefit from an approach that permits the specification of a distribution of GIA, thermal expansion, and melt contribution models.

Recently, Gaussian Process (GP) regression (Rasmussen and Williams, 2006) has been adopted for examining a decomposition of the tide gauge signal along the east-coast of the United States into globally, regionally, and locally coherent fields (Kopp, 2013). This approach, which can also be considered a form of spatio-temporal kriging, uses the covariances between tide gauge locations associated with different physical processes such as GIA or sea-

level changes due to rapid melt events, to estimate both the field at unobserved locations and the magnitude of the underlying contributions. The present work builds on the Kopp (2013) methodology to separate the source contributions to 20th century sea-level change, including melt contributions, ocean dynamics, and on-going GIA to the last ice age.

There are three immediate reasons why the GP approach is well suited to this problem.

First, the sparsity and incompleteness of the tide gauge record is naturally accommodated by the Bayesian nature of the methodology. A prior distribution of sea-level change, estimated using the modeled and underlying relationships between variations in relative sea-level height, is conditioned by the available observations to generate a posterior estimate of the sea-level height at locations and times that lack observations.

Second, the methodology is not directly parametric, which allows the model to be based on the inherent signal characteristics rather than a pre-defined functional form. Any parameterization that exists enters through hyperparameters that partially characterize the prior distribution along with knowledge of the relevant sea-level physics. Using spatio-temporal covariances to specify the model rather than the functional form of the underlying signal also serves to easily incorporate non-stationarity in either the noise or signal characteristics.

Third, the fully probabilistic nature of the method means that measurement and inferred uncertainties are propagated throughout the solution. The inferred posterior probability distribution allows both extreme-value questions, such as a comparison between the rates of sea-level change due to recent melting and to melting at any other time over the past century, and the correlation between posterior model parameter estimates, to be addressed.

In the following, we begin by describing the GP regression method and the spatio-

temporal covariance matrices describing the underlying processes for sea-level variability. We next apply the methodology to tide gauge records from the Permanent Service for Mean Sea Level (Holgate et al., 2013) (PSMSL) database to decompose the contributions to sea-level change over the 20th century.

6.2 Methods

6.2.1 Gaussian Processes

We model sea-level as a spatio-temporal field, $\mathbf{f}$, that is defined as:

$$\mathbf{f}(\mathbf{x}, t) = \mathbf{f}_{GIA}(\mathbf{x}, t) + \mathbf{f}_{M}(\mathbf{x}, t) + \mathbf{f}_{LSL}(\mathbf{x}, t) \tag{6.1}$$

where $\mathbf{f}_{GIA}$, $\mathbf{f}_{M}$ and $\mathbf{f}_{LSL}$ are, respectively, the components of the field due to GIA, on-going melt contributions from land-based ice complexes, and local sea-level changes due to ocean dynamics, tectonics and other non-climatic factors, as a function of position, $\mathbf{x}$, and time, t. Each component of the total field in Equation 6.1 is modeled as a Gaussian process with a mean, μ_i, and covariance, K_i, such that, for example:

$$\mathbf{f}_{GIA}(\mathbf{x}, t) \sim \mathcal{GP}(\mu_{GIA}, K_{GIA}) \tag{6.2}$$

The total field in Equation 6.1 can be written as a multivariate distribution where the field is partitioned into observed sites, $\mathbf{f}_1$, and unobserved sites, $\mathbf{f}_2$, such that:

$$\begin{bmatrix} \mathbf{f}_1 \\ \mathbf{f}_2 \end{bmatrix} \sim \mathcal{N}\left(\begin{bmatrix} \mu_1 \\ \mu_2 \end{bmatrix}, \begin{bmatrix} K_{11} & K_{12} \\ K_{12}^T & K_{22} \end{bmatrix} \right) \tag{6.3}$$

Observations of the field, $\mathbf{y}(\mathbf{x}, t)$, from tide gauges are modeled as the underlying signal with additive white noise, such that:

$$\mathbf{y}(\mathbf{x}, t) = \mathbf{f}_1(\mathbf{x}, t) + \epsilon(\mathbf{x}, t) \tag{6.4}$$

where ϵ is a white noise component attributed to measurement error in the observations and is described by the distribution (e.g. Rasmussen and Williams, 2006):

$$\epsilon(\mathbf{x}, t) \sim \mathcal{N}(\mathbf{0}, \Sigma_p) \tag{6.5}$$

where Σ_p is an identity matrix scaled by a hyperparameter that is estimated from the available observations. Combining Equations 6.3 and 6.4, considering Equation 6.5, the joint distribution of the observations and the value of the field at unobserved sites and times is:

$$\begin{bmatrix} \mathbf{y} \\ \mathbf{f}_2 \end{bmatrix} \sim \mathcal{N}\left(\begin{bmatrix} \mu_1 \\ \mu_2 \end{bmatrix}, \begin{bmatrix} K_{11} + \Sigma_p & K_{12} \\ K_{12}^T & K_{22} \end{bmatrix} \right) \tag{6.6}$$

From this, the mean of the conditional distribution of the field at the unknown sites, given the observations, is (Rasmussen and Williams, 2006):

$$\overline{\mathbf{f}_2} = K_{12}^T [K_{11} + \Sigma_p]^{-1} \mathbf{y} \tag{6.7}$$

The covariance of the conditional distribution is computed using the Schur compliment of K_{22} from the the covariance in Equation 6.6 (Rasmussen and Williams, 2006):

$$\mathbf{V} = K_{22} - K_{12}^T[K_{11} + \Sigma_p]^{-1}K_{12} \tag{6.8}$$

Thus, we use Equation 6.8 to estimate the spatio-temporal distribution of the sea-level heights at the unobserved tide gauges. To decompose total sea-level heights into their constituent parts, only those covariances containing the desired components, such as GIA or the melt from a particular ice sheet, are included in K_{12} and K_{22}.

6.2.2 Covariance Structures

As discussed in the Introduction, there are four broad divisions into which mechanisms for sea-level change can be categorized, each with distinctive characteristic time and spatial scales: 1) on-going GIA due to Late Pleistocene glaciation; 2) ocean dynamics and thermosteric changes; 3) freshwater addition from land-based ice sheets and glaciers; and 4) regional, non-climatic processes such as subsidence and tectonics. In principle, the distinct spatio-temporal variability of the signals for each of these processes provides a framework for estimating the source(s) of sea-level change. However, there are currently only a limited number of available ocean dynamics model outputs and as such discriminating between the variability due to ocean dynamics and the signal from other local effects is challenging. Consequently, we group sea-level signal due to the ocean dynamic variability with the non-climatic factors and separate the contributions due to this grouping from the signals associated with GIA and land-ice melt.

We model the global sea-level field (Equation 6.1) as a Gaussian process that has mean equal to the sum of the means of the GIA signal and ocean dynamic models and a covariance that is the sum of the contributing covariances:

$$K = K_M + K_{GIA} + K_{LSL} \tag{6.9}$$

Each of the constituent covariances is described below.

Melt contributions

The covariances describing the melt contributions to sea-level change, $K_M(t, \mathbf{x})$, are modeled as the summation of space-time separable covariances for each melt source considered:

$$K_M(t, \mathbf{x}) = \sum_{a=1}^{n} (K_{M,a}^{L} + K_{M,a}^{RQ})(t) K_{M,a}(\mathbf{x}) \tag{6.10}$$

where the summation index indicates the a^{th} ice sheet or mountain glacier. For the temporal covariance of each of the melt contributions, we use the sum of a linear component, $K_M^L(t_i, t_j)$, to account for secular changes in the melt contributions and a rational quadratic term, $K_M^{RQ}(t_i, t_j)$, representing a smoothly-varying function of variability where:

$$K_M^L(t_i, t_j) = k_1 t_i t_j \tag{6.11}$$

and,

$$K_M^{RQ}(t_i, t_j) = k_2 (1 + \frac{\Delta t_{i,j}^2}{2\alpha\tau_s^2})^{-\alpha} \tag{6.12}$$

Here, t_i and t_j represent the time at the i^{th} and j^{th} time step, Δt_{ij}, represents the time difference between these steps, k_1, k_2, α and τ_s are hyperparameters that define the linear amplitude, rational quadratic amplitude, roughness and characteristic timescale of the covariance functions (Rasmussen and Williams, 2006). To estimate the hyperparameters, we adopt an empirical Bayesian approach where we compute the parameters that maximize the likelihood of reconstructed time series of previous mountain glacier melt estimates (Kaser et al., 2006) and ice sheet melt estimates (Gregory et al., 2012).

The spatial covariance of each melt contribution, $K_{M,a}(\mathbf{x})$, is computed as the outer product of the unique fingerprint associated with melt from that specific land-based ice complex. The GIS, WAIS, and EAIS fingerprints were computed assuming a geographically uniform melt across the surface of the ice sheets. The mountain glacier fingerprints were computed with a 1-degree disk centered on the areal extent of the glaciers. The computation of the fingerprints is based upon a gravitationally self-consistent SL theory that incorporates shoreline migration and changes in grounded, marine-based ice cover as well as the feedback into SL of perturbations in the Earth's rotation axis (Kendall et al., 2005; Milne and Mitrovica, 1998, see also Chapter 2) (see Chapter 2). Given that the $\sim$100 yr timescale under study is significantly less than the characteristic relaxation time ($\sim$500 yr) for a viscoelastic Earth, we have adopted a 1D elastic Earth model based on the Preliminary Reference Earth Model (Dziewonski and Anderson, 1981) to compute the various sea level fingerprints of rapid melting.

GIA contributions

The spatio-temporal covariance for the GIA contribution to sea-level change, $K_{GIA}(t, \mathbf{x})$, is taken as the sample covariance of 72 predictions of relative sea-level change computed using a more general version of the sea-level theory than was used for the rapid melt fingerprints that includes a viscoelastic response to loading changes. The prior mean is taken as the sample mean across the models at each tide gauge location. The predictions of GIA are dependent on the deglaciation history of the Late Pleistocene ice sheets and the Earth's viscoelastic structure. Each of the 72 predictions represents a different 3-layer model (lower mantle viscosity, upper mantle viscosity, lithospheric thickness) of the Earth's rheology combined with the ICE-5G ice sheet reconstruction (Peltier, 2004). The rheological models use lower mantle viscosities between 2 and 20×10^{21} Pa s, upper mantle viscosities between 0.3 and 1×10^{21} Pa s and lithospheric thicknesses between 72 and 125 km.

Figure 6.1 shows the standard deviation in the prior distribution of sea-level rates (mm/yr) associated with the GIA contribution. The largest variability occurs in the regions under and adjacent to the location of the former Late Pleistocene ice sheets which is not unexpected given the sensitivity of the geometry and amplitude of post-glacial uplift and peripheral bulge subsidence to the Earth model (Mitrovica and Davis, 1995) (see Chapter 2).

Ocean dynamics, tectonics and other non-climatic contributions

The contribution to sea-level changes from thermometric and ocean dynamics effects are partially modeled as the spatio-temporal sample mean and covariance of 7 models from the World Climate Research Programme's Coupled Model Intercomparison Project phase

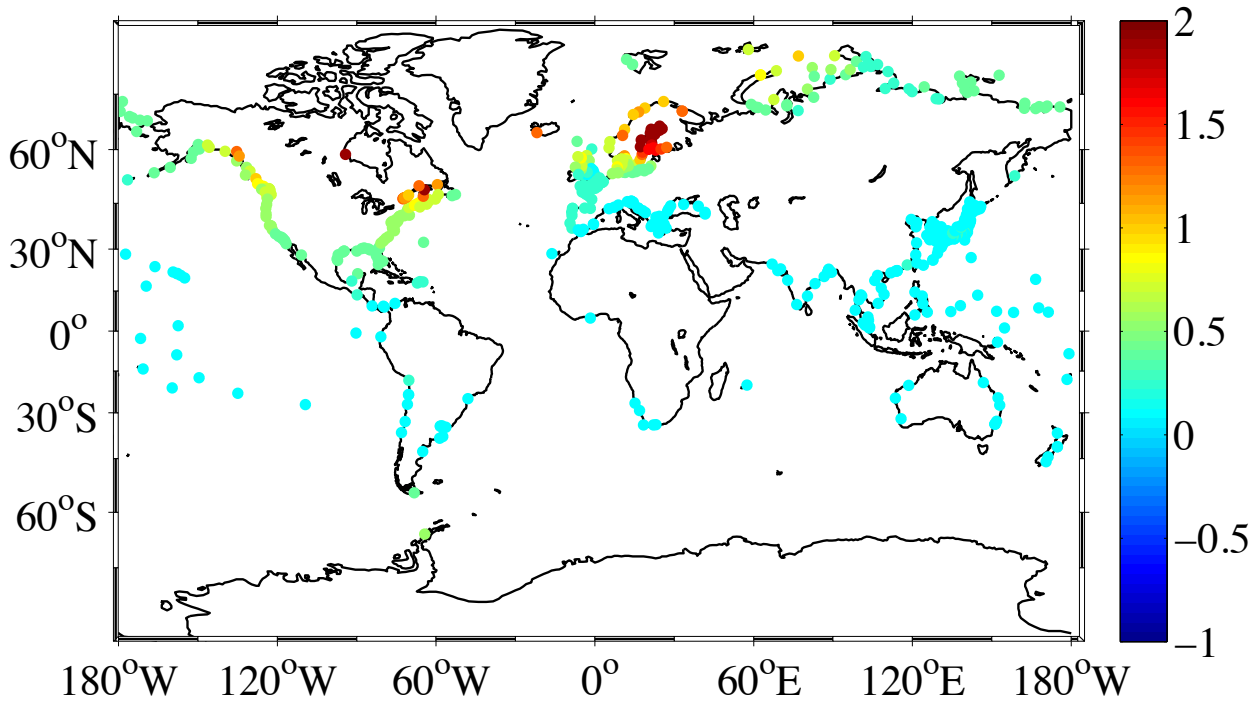

Figure 6.1: Map showing the standard deviation in sea-level rates (mm/yr) at the tide gauge sites considered in this study due to the GIA process.

5 (CMIP5) dataset (Taylor et al., 2012): Beijing Climate Center Climate System Model 1.1 (bcc-csm1-1), Canadian Center for Climate Modelling and Analysis Second Generation Earth System Model (CanESM2), Geophysical Fluid Dynamics Laboratory Earth System Model (GFDL-ESM2M), Institut Pierre Simon Laplace Earth System Model (IPSL-CM5A-LR), University of Tokyo/NIES/JAMSTEC Model for Interdisciplinary Research on Climate (MIROC5), Meterological Research Institute Coupled Global Climate Model 3 (MRI-CGCM3), and the Norwegian Earth System Model 1(NorESM1-M).

Figure 6.2 shows the decadal mean rates of the ocean dynamics contributions to GMSL computed from the 20th century simulations of each of the aforementioned models. Between 1900 and 2000, the mean of the models is ~ 0.6 mm/yr, though this rises to ~ 1.4 mm/yr from 1980 to 2000.

In addition to difference in GMSL, each model considered in Figure 6.2 is also characterized by a distinct spatial geometry of sea-level change. The top frame of Figure 6.3 shows the standard deviation of the sea-level height distribution within the ocean dynamics models in the decade centered on the year 2000. The middle and bottom frames show the difference in the standard deviation of the distributions between the decade centered on the year 2000 and the decades centered on the years 1950 and 1900, respectively. In the decade centered on the year 2000, the largest variability between the models are located in the Baltic, Gulf of Mexico and equatorial Pacific.

While the model outputs are global ocean fields, we require a statistical representation of the the ocean dynamic signal at the locations of the tide gauges. When this location is coincident with a model grid point, the value at the grid point is used. If the tide gauge

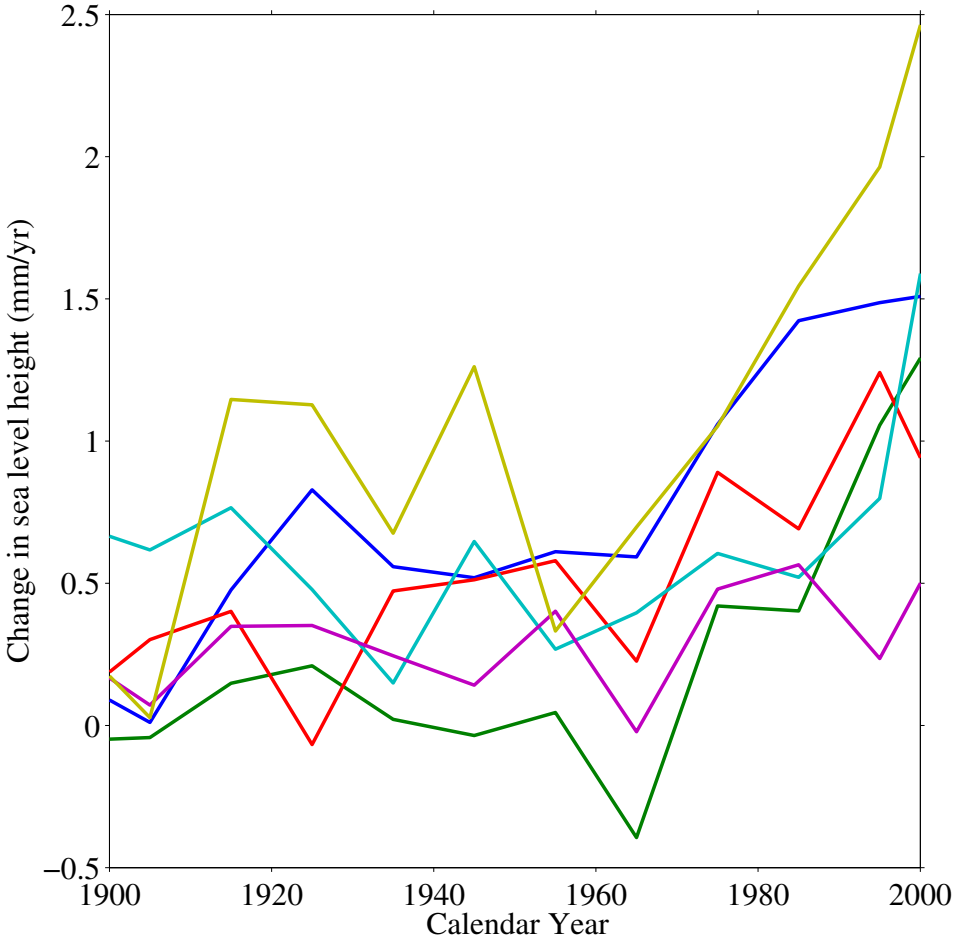

Figure 6.2: Plot showing the decadal means of GMSL rate as simulated by the CMIP5 models. The colors indicate the following models: bcc-csm1-1 (blue); CanESM2 (green); GFDL-ESM2M (red); IPSL-CM5A-LR (cyan); MRI-CGCM3 (magenta); NorESM1-M (yellow).

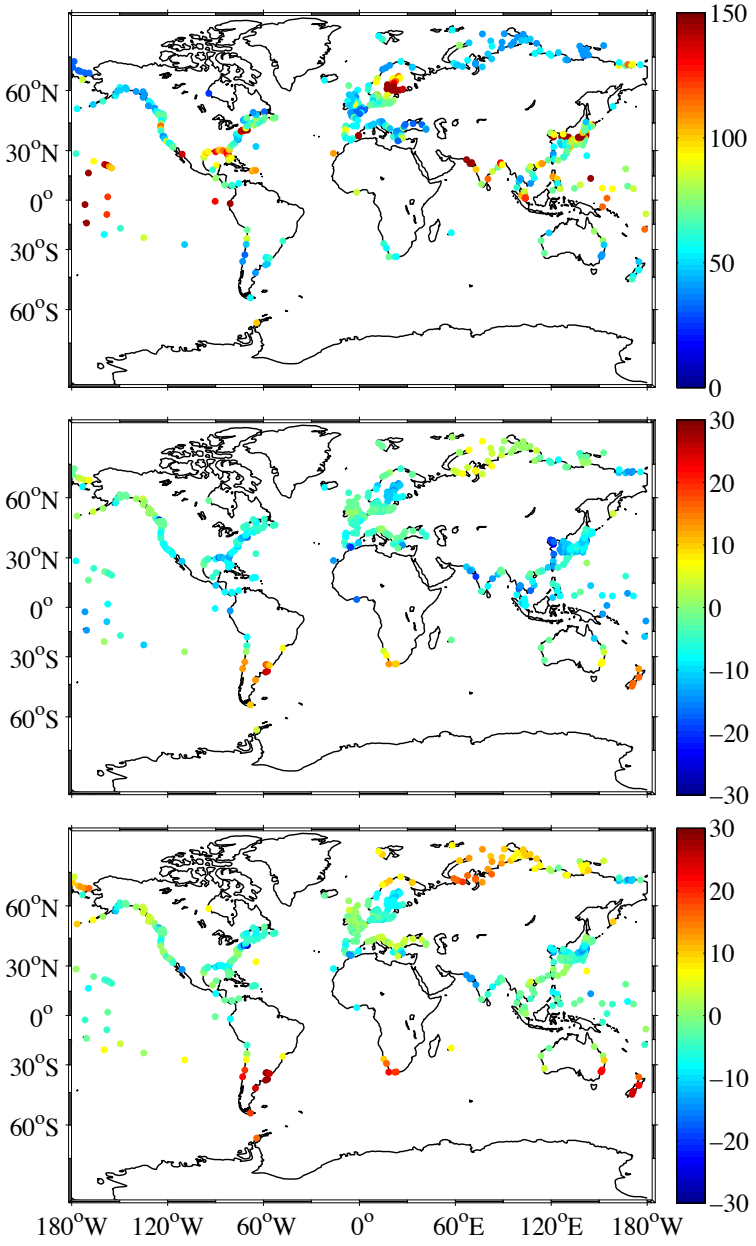

Figure 6.3: Map showing the standard deviation in sea level height (mm) at the tide gauge sites used in this study due to the distribution of steric models. The top frame shows the standard deviation (mm) in the decade centered on the year 2000. The middle and bottom frames show the difference between the standard deviation in the decade centered on the year 2000 and the decades centered on the years 1950 and 1900, respectively.

location does not lie on a model grid point, we use an inverse distance weighting interpolation scheme to estimate the field at the desired location.

Since the distribution of ocean dynamics models is computed from a sample size of 7, it is unlikely to be entirely representative of the parent distribution. Consequently, we supplement the sample covariance with a separable, spatio-temporal covariance structure consisting of the product of Matérn functions, one representing the temporal distribution, and the other the spatial, such that the total covariance describing local sea-level change is:

$$K_{LSL}(t, \mathbf{x}) = K_{CMIP5}(t, \mathbf{x}) + C(t, \nu_1, \tau)C(\mathbf{x}, \nu_2, L) \tag{6.13}$$

where K_{CMIP5} represents the sample covariance of the CMIP5 results, ν_1 and τ are the smoothness parameter and characteristic time scale of the temporal Matérn function, respectively, while ν_2 and L are the smoothness parameter and characteristic length scale of the spatial Matérn function, respectively. In addition to capturing the inaccuracies of the ocean model distribution, Equation 6.13 also models local tectonic, geomorphological and other non-climatic contributions to local sea-level change. The form of the associated Matérn functions used in Equation 6.13 is:

$$C(r, \nu, \gamma) = \frac{2^{1-\nu}}{\Gamma(\nu)} \left(\frac{\sqrt{2\nu}r}{\gamma} \right)^{\nu} K_{\nu} \left(\frac{\sqrt{2\nu}r}{\gamma} \right) \tag{6.14}$$

where Γ is the gamma function, K_{ν} is a modified Bessel function of the second kind, γ is a scale parameter, and ν is a parameter specifying the smoothness of the function.

For the exponents within the Matérn functions, we follow Kopp (2013) and set the ex-

ponent on spatial component to $\nu_2 = \frac{5}{2}$ and the exponent on the temporal component to $\nu_1 = \frac{3}{2}$. In future iterations of this work, these parameters can be set as hyperparameters and estimated from the available data.

The hyperparameters of the Matérn structures and the white-noise variance are computed by finding the parameters that maximize the likelihood of the available tide gauge observations, given the complete model represented by Equation 6.9.

6.2.3 Description of tide gauge data

The Permanent Service for Mean Sea Level (PSMSL) Revised Local Reference (RLR) database (Holgate et al., 2013) contains ∼1200 tide gauge records of relative sea level (www.psmsl.org). While the database is global and contains records that extend back through the early 19th century, there is a significant northern hemisphere bias in the coverage of sites and also a significant variation in the duration and completeness of individual records. In the present study, we restrict the set of tide gauges we adopt to the 596 sites that have at least 20 years of data coverage within the last 50 years in order to maintain a minimum level of data completeness. We use the decadal means, centered around the indicated year, of the mean annual record between 1900 and 2000 to limit the spatio-temporal covariance matrices, which contain elements for the sea-level height for each decade in the 20th century for each tide gauge site, to a computationally tractable size.

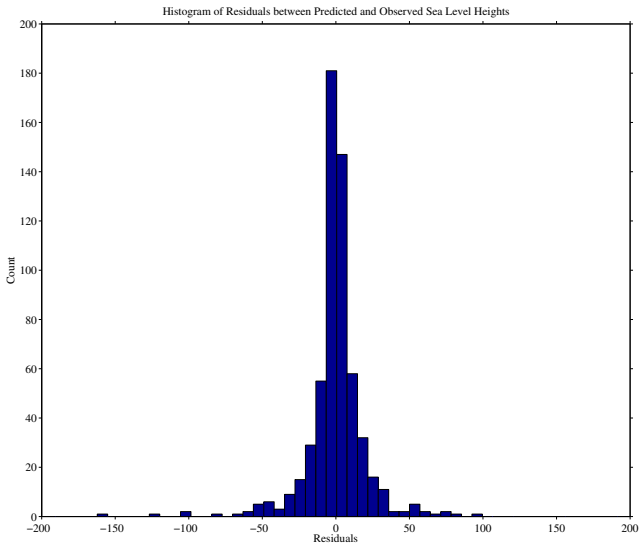

Figure 6.4: Histogram of the residuals (mm) between the predicted and observed sea level at the 596 tide gauge sites used in this study.

6.3 Results and Discussion

6.3.1 Comparison of tide gauge observations and predictions

To evaluate the results of the regression analysis we first examine the residuals between predictions of the tide gauge records of sea level at each decade against the available observations. Figure 6.4 shows a histogram of the residuals.

The distribution of the residuals has a mean of 8.9 mm and a standard deviation of 13.4 mm. While the histogram shows the distribution of the fit at all sites on aggregate, Figure 6.5 shows a map of the mean residual between the predicted height and the available observations at each site. Also plotted on Figure 6.5 is the mean and 1-σ standard deviation of the predictions of the relative sea level, along with the decadal means and standard deviations of the observations, at six tide gauge locations distributed around the continental coastlines.

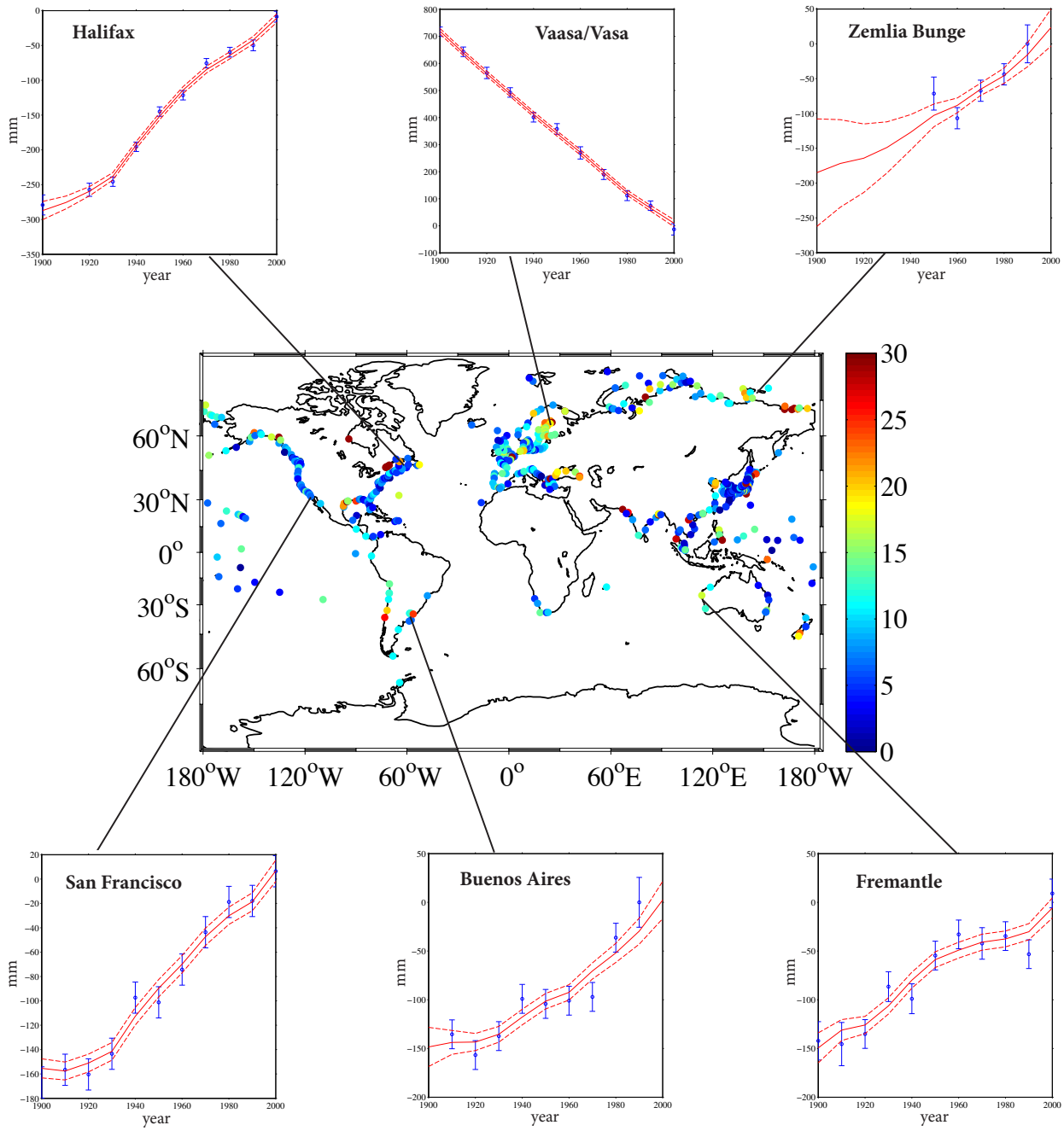

Figure 6.5: Map showing the spatial distribution of the mean residuals (mm) between the predicted and observed heights at the tide gauge sites used in this study. The inset figures show the decadal mean and standard deviation of the tide gauge record (blue circles with error bars) and the predicted height (solid red line) and 1-σ uncertainty (dotted red line) at a selection of sites.

Figure 6.5 indicates that the largest mean residuals occur in three types of regions: outlets of major river systems (e.g. Indus, St. Lawrence, Mekong, Uruguay, Philippines); tectonically active regions like the island of Japan and Peru; and regions experiencing large rates of crustal uplift due to GIA such as Hudson's Bay and the Gulf of Bothnia. The occurrence of large residuals in the first two of these regions suggests that the Matérn covariance structures used to capture local sea-level effects is insufficient to account for either high sedimentation rates or significant tectonic processes at the small number of outlier tide gauge locations. However, limiting either the characteristic time scale or length scale of the Matérn structures in order to accommodate specific outlier records may reduce the predictive skill of the model for computing the posterior distribution of sea level at geographically isolated sites or records with significant data gaps. The large residuals in the vicinity of the former Late Pleistocene ice sheets, however, can be attributed to the large rate of change in sea level within those regions, as can be seen in the Vaasa/Vasa record, which lies at the location of the former Fennoscandian ice sheet. The effect of these large magnitudes is that large absolute differences between the observations and the predictions can occur even with relative errors that are comparable to the uncertainties at the other sites.

The Zemlia Bunge record in Russia demonstrates the behavior of the prediction in the absence of observations. Through the second half of the century, the predictions are constrained by observations with uncertainties that are of the same size or smaller than the decadal mean uncertainties. However, prior to 1950, the uncertainty in the predictions increases with the lack of observational constraints.

Overall, with the exception of Zemlia Bunge, the insets in Figure 6.5 sample sites rep-

resent some of the longest records available in the PSMSL database. In each case, the predictions show good agreement between the predicted distribution and the decadal means of the observations, and these fits are representative of the results at the bulk of the 596 tide gauge sites considered in this study.

6.3.2 Regional Trend Decompositions

Moving beyond reconstructions of the total sea-level record at each site, Figures 6.6 through 6.8 show a decomposition of the total sea level height at three tide gauge locations representing some of the longest and most continuous records in the PSMSL database: Brest, France; Halifax, Canada; Vaasa, Finland.

Woodworth et al. (1999) noted that mean sea-level rates in Europe were anomalously low when compared with the global mean sea level (GMSL) rate over the 20th century. The top frame of Figure 6.6 shows the predicted and observed sea level at the tide gauge in Brest, France. The middle frame of Figure 6.6 shows the estimated contribution from GIA to this trend. The GIA signal has a rate of 0.6 mm/yr, and the mean GIA-corrected sea-level rate at Brest is 1.0 mm/yr, significantly lower than previous estimates of GMSL (1.7 mm/yr) (Church et al., 2011). The bottom frame of Figure 6.6 shows the estimated contribution from all melt sources to sea level at Brest. The mean rate of melt contribution at Brest over the 20th century is 0.8 mm/yr, or 80% of the trend at that site.

As we will demonstrate below, the estimated GMSL rate is $\sim$24% lower than previous estimates, meaning that sea level rates around Europe are less anomalous than previously estimated.

Figure 6.7 shows a decomposition of sea level at the tide gauge in Halifax, Canada. Once

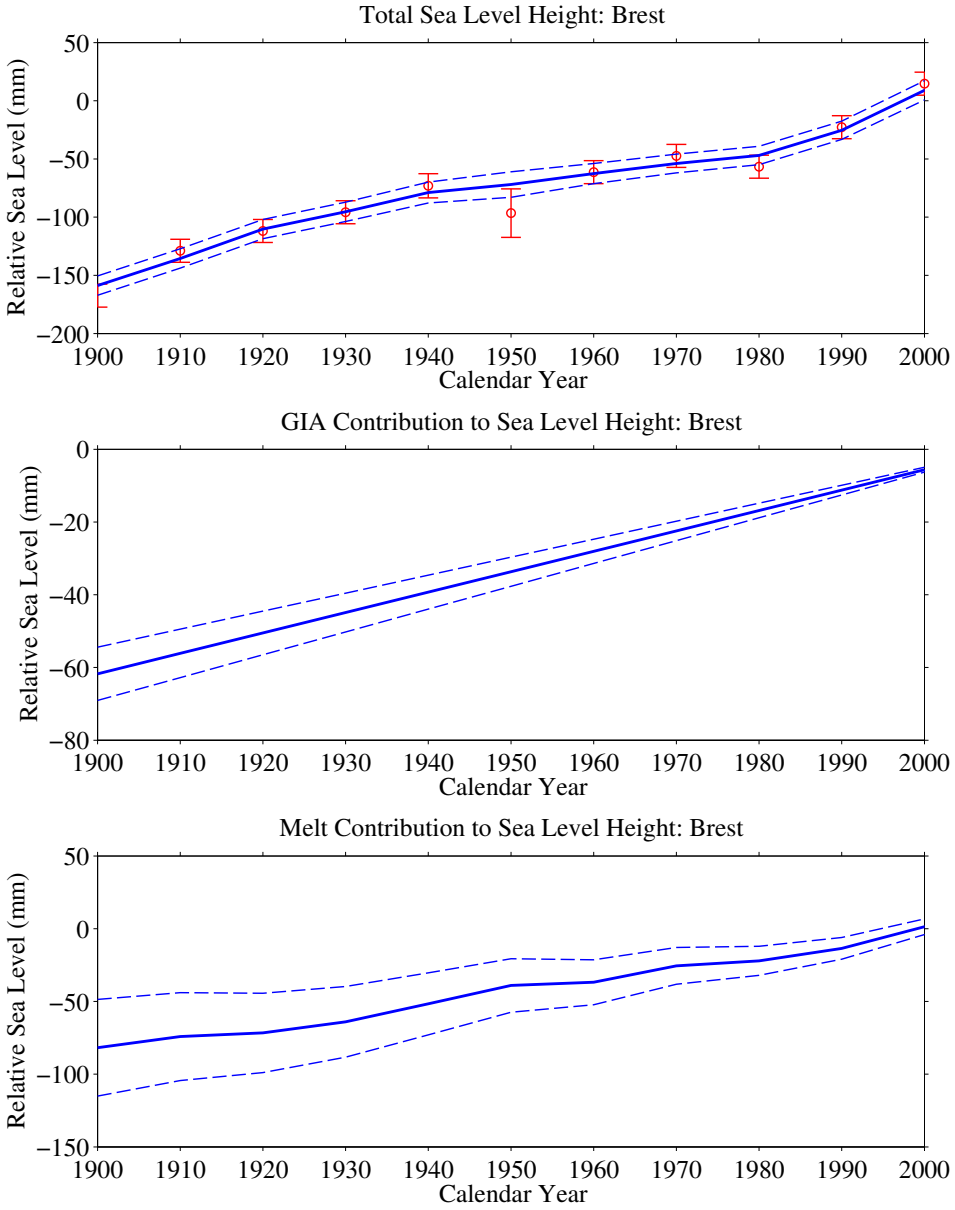

Figure 6.6: Decomposition of tide gauge record of sea level at Brest, France. The top frame shows the predicted sea level together with the decadal means and standard deviations of the observations (red circles). The middle frame shows the GIA contribution to the sea level. The bottom frame shows the sum of all melt contributions to the sea level. The solid and dotted blue lines indicate the mean and 1-σ uncertainty of the various estimates, respectively.

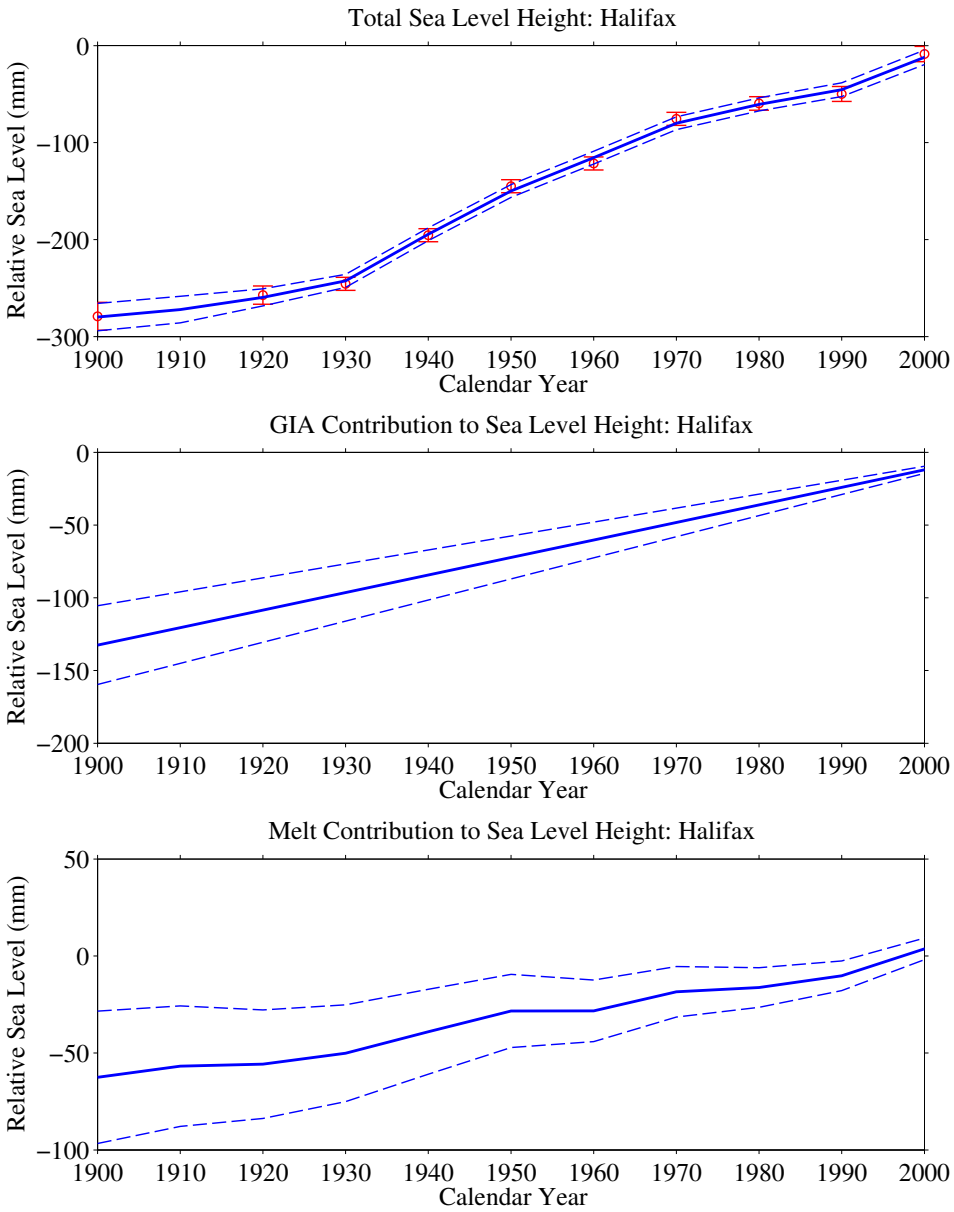

Figure 6.7: As in Figure 6.6 except for the tide gauge site at Halifax, Canada.

again, the top frame of Figure 6.7 shows the estimated and observed sea level over the 20th century, while the middle frame shows the GIA contribution to sea level height. The GIA rate at Halifax is estimated to be 1.2 ± 0.2 mm/yr leaving a GIA-corrected mean rate over the century of 1.3 ± 0.3 mm/yr. We note that this range encompasses two previously published GIA-corrected mean rates: 1.01 mm/yr based on the VM2 viscosity model and the ICE-5G history (Peltier, 2004) and 1.56 ± 0.15 mm/yr computed by Davis and Mitrovica (1996) who argued that a lower mantle viscosity ~ 2.5 times the value of the VM2 model provided a better fit to the trends in tide gauges along the east coast of North America. The relatively large uncertainty is due to the broad prior distribution of the GIA rate in this region which is located on the peripheral bulge of the former Laurentide ice sheet and is thus sensitive to the viscosity of the upper mantle and the top half of lower mantle.

Next, Figure 6.8 shows a decomposition of sea level at Vaasa, Finland. The observed (and predicted) rate of sea-level change is negative, and of significantly larger amplitude than either of the previously examined sites. This is due to the dominance of the GIA contribution to sea level, as is evident in the middle frame of the figure. The estimated GIA contribution to sea-level change is -7.3 ± 0.3 mm/yr. This is less than, for example, the GIA contribution of -9.6 mm/yr estimated using the VM2/ICE-5G (Peltier, 2004). Our results indicate a preferred upper mantle viscosity, in this region, that is less than the VM2 value of 0.5×10^{21} Pa s.

6.3.3 The GP preferred GIA model

Moving beyond these single site comparisons, we next use the predictions of the GIA rates at 596 sites to find the GIA model from the suite of 72 models that maximizes the likelihood

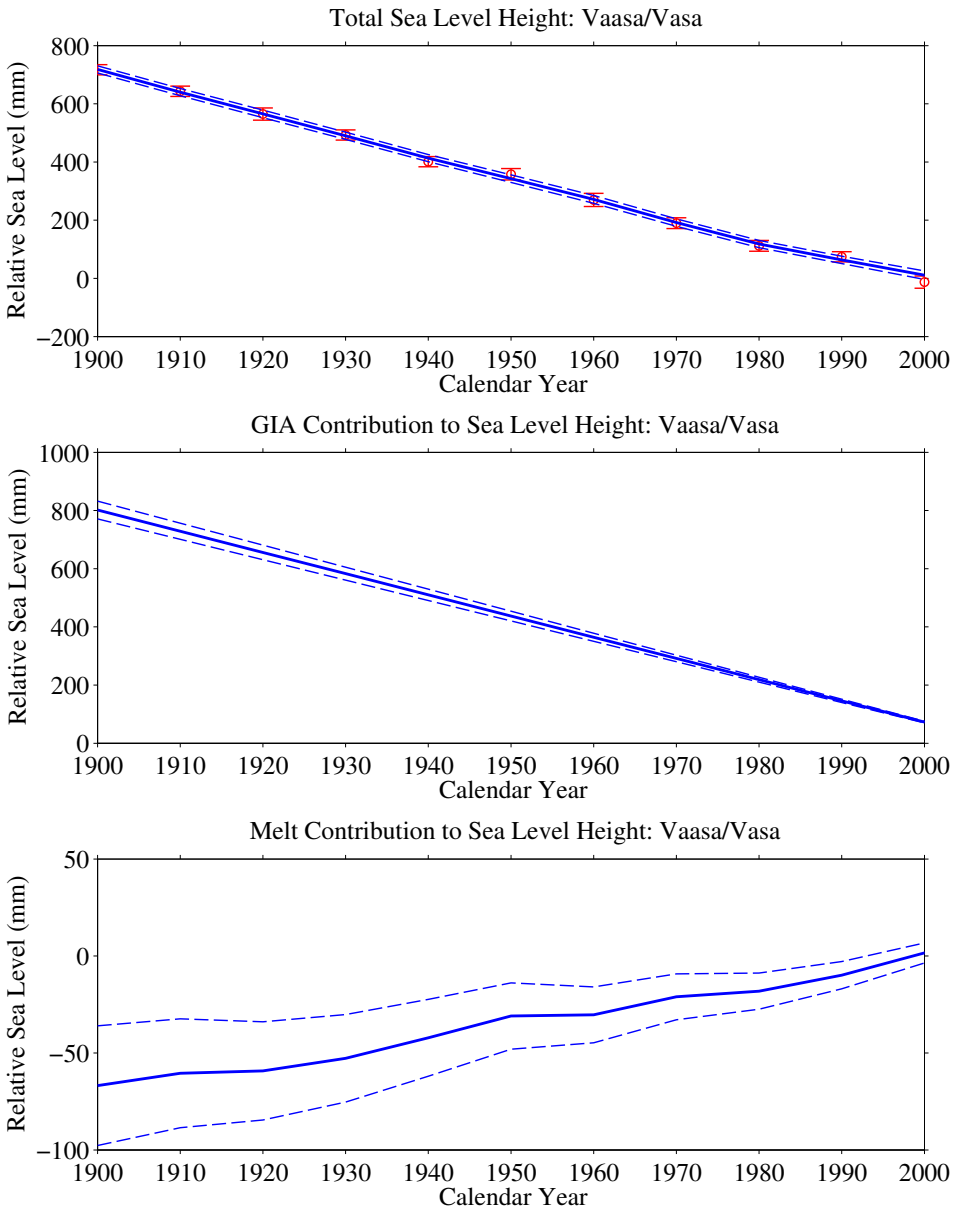

Figure 6.8: As in Figure 6.6 except for the tide gauge site at Vaasa, Finland.

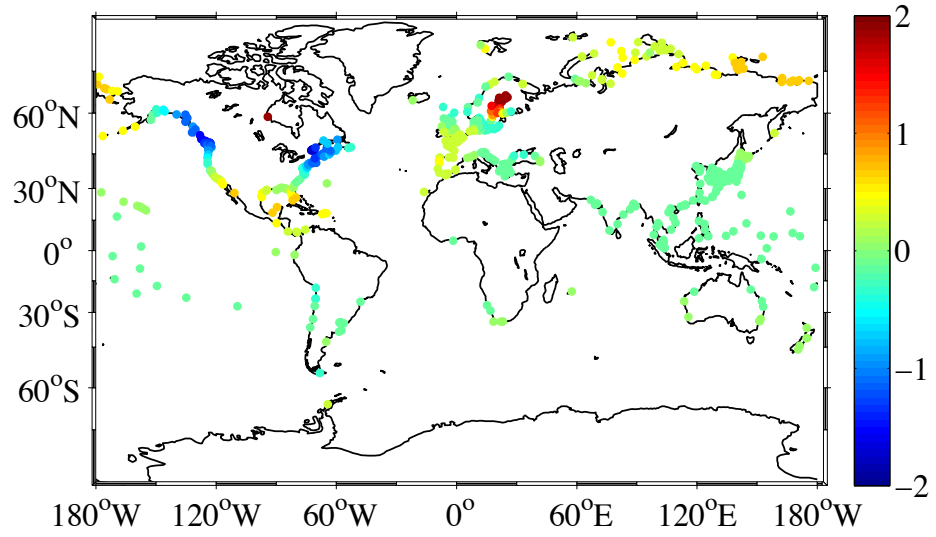

Figure 6.9: Map of difference (mm/yr) between the estimated GIA rate contribution at each site and the rate contribution predicted by the VM2 viscosity model.

given estimates at each site. This preferred model corresponds to a lithospheric thickness of 100 km, an upper mantle viscosity of 0.5×10^{21} Pa s and a lower mantle viscosity of 5×10^{21} Pa s. This model, which has a lower mantle viscosity that is 2.5 times larger than VM2, corresponds well with the lower mantle viscosity inferred by Davis and Mitrovica (1996). It is also consistent with the average viscosity in the top half of the lower mantle (the region to which GIA data are most sensitive) estimated by Mitrovica and Forte (2004) based on a joint inversion of mantle convection and GIA observables. We note, however, that the GIA response is dependent on both the rheological model and the adopted deglaciation history. All GIA models used in the present study, used the ICE-5G history (Peltier, 2004). Adopting different deglaciation histories would allow for a more robust estimate of the viscosity profile.

Figure 6.9 is a map showing the difference between the estimated GIA rates and the rates predicted using the VM2 (ICE-5G) model. The largest differences occur near the locations of the Late Pleistocene ice sheets. Namely, at sites around the Gulf of Bothnia the

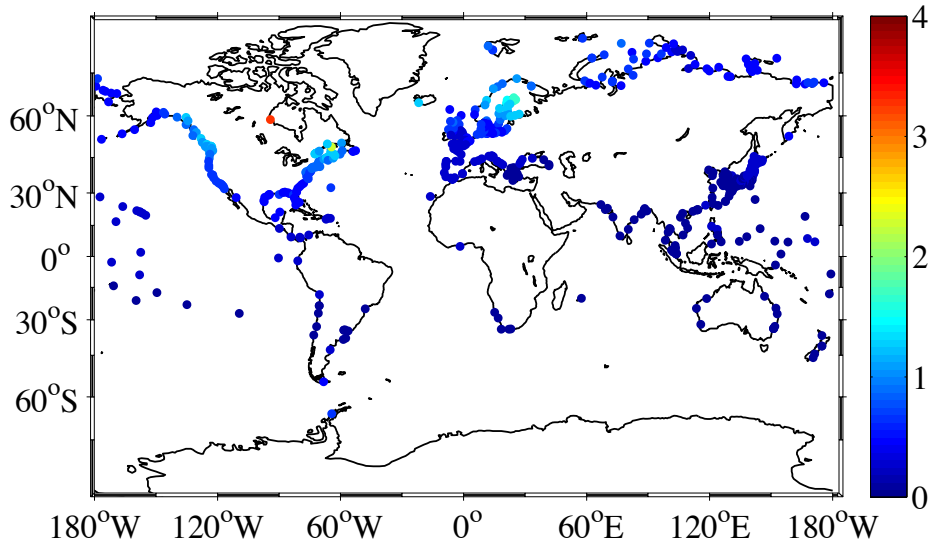

Figure 6.10: Map of the 1-σ posterior standard deviation (mm/yr) of the predicted GIA contribution at each site.

estimated GIA contribution to the sea level rate is up to ∼2 mm/yr smaller than the rates predicted by VM2. Along both the east and west coasts of North America, the estimated GIA contribution is up to ∼1 mm/yr less than the value estimated by VM2. As noted above, the large discrepancies at these latter sites is likely due to their location on the peripheral bulge of the former Laurentide ice sheet which makes them very sensitive to the viscosity of the top half of the of lower mantle (Davis and Mitrovica, 1996). Nevertheless, estimates of sea level in these regions are also characterized by an uncertainty in the estimated GIA rates that is large enough to account for the large discrepancies (Figure 6.10).

6.3.4 Estimates of melt contributions

The covariance representing the on-going melt contributions contains the fingerprints associated with melt from 22 distinct sources. If the observation record extensively sampled the global sea-level field, in particular in the near-field region of the melt sources which would

be characterized by the highest gradients in sea level, then each melt contribution would be highly resolvable. However, the relatively sparse sampling of the field over the 20th century means that some of the melt contributions are highly correlated with each other and as such cannot be uniquely identified.

To identify the resolvable melt sources we compute the so-called resolution matrix, R, which describes the mapping of the true parameter values into the parameter estimates:

$$R = G^{\dagger}G \tag{6.15}$$

where G contains the sea level fingerprints that map the estimated melt parameters into local sea level at the available tide gauge sites and the dagger indicates a generalized inverse. In the Bayesian GP formulation we can define the effective generalized inverse, $G^{\dagger}$, in terms of the conditional distribution as:

$$G^{\dagger} = K_{12}^{T}[K_{11} + \Sigma_p]^{-1} \tag{6.16}$$

Each row, j, of R describes the weightings on the true model parameters that will sum to yield the estimate of the jth model parameter. Where R is the identity matrix, the model parameters are completely resolvable, while the presence of significant, non-zero off-diagonals represent model parameters, or melt contributions, that cannot be separated due to the available sampling.

To explore the resolution of the melt sources as a function of time, we compute the resolution matrix for each decade in the 20th century, using only the records available in

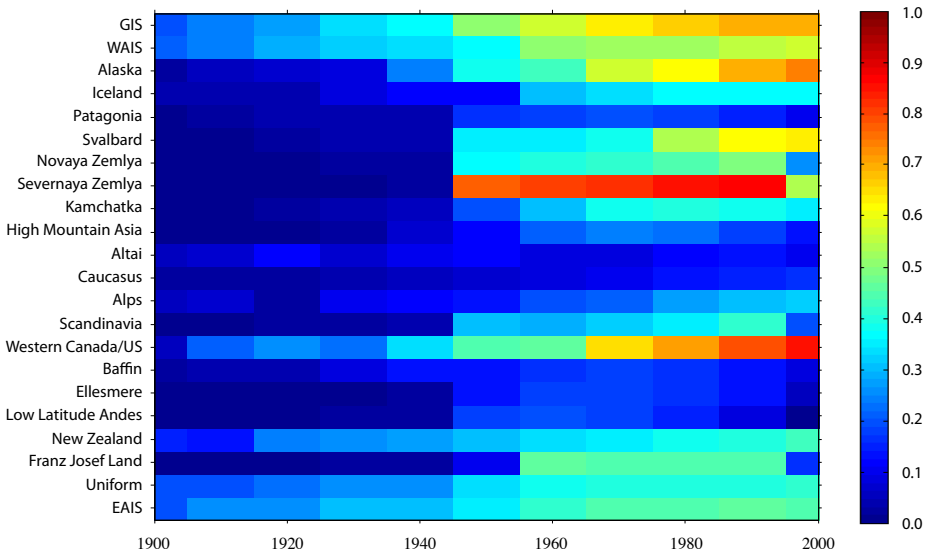

Figure 6.11: Diagonal elements of the melt contribution parameter resolution matrix over the 20th century.

that decade.

Figure 6.11 shows the diagonals of the melt parameter resolution matrix as a function of time. In general, the resolvability of most parameters is low until the 1950s at which point it improves for the glaciers of Arctic Russia, Western Canada/US, and Alaska, and the Greenland Ice Sheet become more resolvable. This improvement in the resolvability of many of the melt sources beginning in the 1950s coincides with a significant increase in the number and distribution of tide gauges.

Figure 6.12 shows the estimated melt rate contribution from the glaciers of Western Canada and the United States. Note that we compute the rate as a forward difference between the sea-level heights at successive times. As the GP regression estimates the component of sea-level change due to an individual melt source at each tide gauge location, we compute the equivalent eustatic contribution from a specific source by dividing the individ-

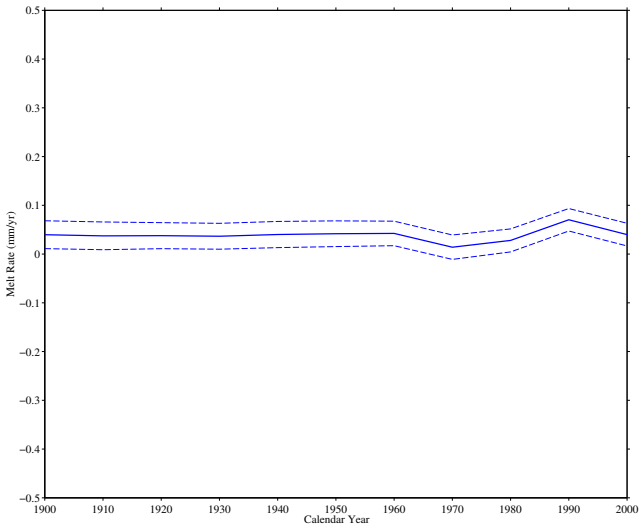

Figure 6.12: Time series of the sum of the melt rate contributions from the glaciers in Western Canada and the US.

ual melt contribution at the tide gauge locations by the associated fingerprint value. The mean rate over the century is 0.04 ± 0.03 mm/yr. For comparison, the Marzeion et al. (2012) model-based estimate of the mean rate from 1900 to 2009 is 0.03 mm/yr. The rate trend shows a slowing of the melt from the century average between 1960 and 1980. This change is consistent with observations that suggest that many glaciers in the North Cascades were characterized by either slowed retreat or advancement due to cooler conditions and increased precipitation during this period (Pelto, 2006).

Figure 6.13 shows the estimated melt rate contribution to sea level from Alaskan glaciers. The mean rate over the century is 0.18 ± 0.06 mm/yr. Berthier et al. (2010) used satellite imagery to estimate that Alaskan glaciers contributed 0.12 ± 0.02 mm/yr from 1962 to 2006 while Marzeion et al. (2012) conclude a lower mean rate from 1900 to 2009 of 0.08 mm/yr from model-based estimates. The time series associated with the Alaskan contribution shows a significant decrease in the melt rate in the 1970s and 1980s. This corresponds well with

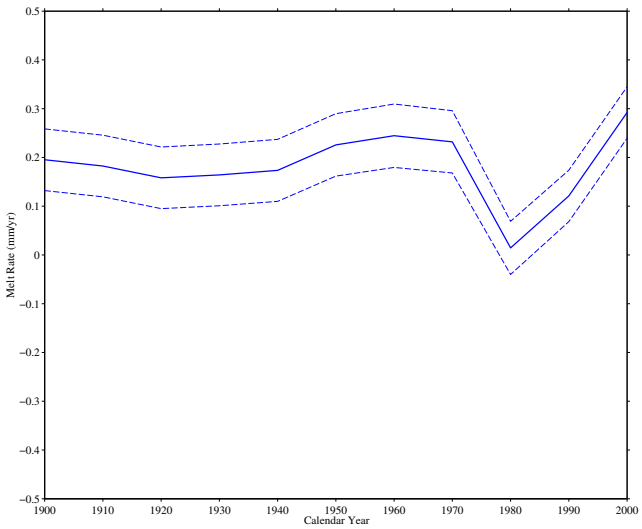

Figure 6.13: Time series of the sum of the melt rate contributions from the Alaskan glaciers.

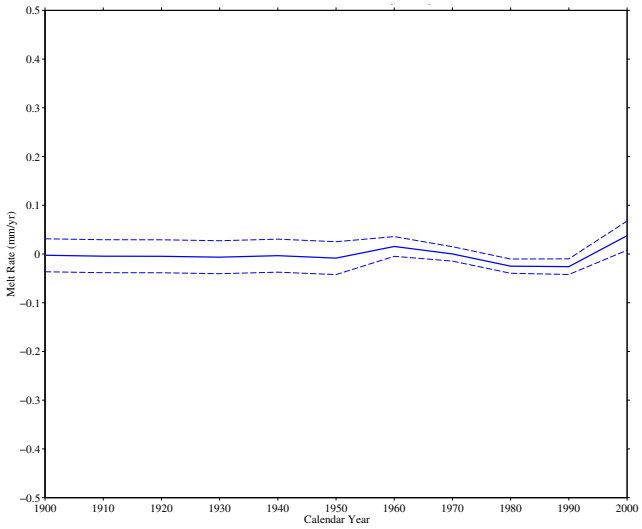

Figure 6.14: Time series of the sum of the melt rate contributions from the Severnaya Zemlya glacier.

a phase of growth in the coastal Wolverine glacier identified for this time period (Mayo and March, 1990; Josberger et al., 2007).

Figure 6.14 shows the estimated melt rate contribution to sea level from glaciers on Severnaya Zemlya. The mean rate over the century is 0.00 ± 0.03 mm/yr. However, in the last portion of the century the melt rate has increased such that in the decade centered on

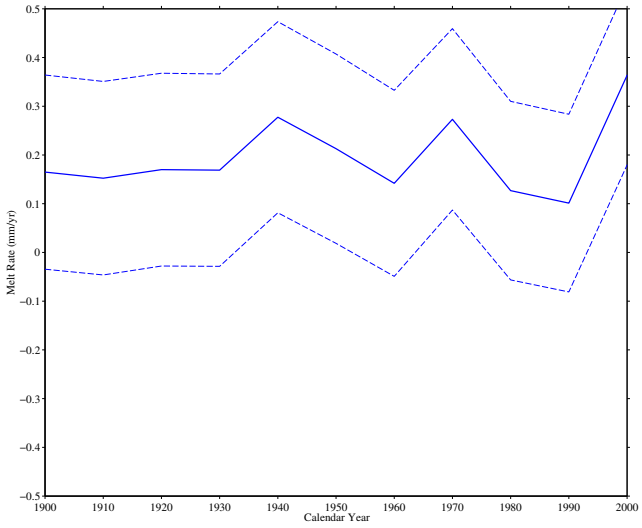

Figure 6.15: Time series of the sum of the melt rate contributions from the Greenland Ice Sheet.

the year 2000, the contribution to sea-level change is 0.04 ± 0.03 mm/yr .

Figure 6.15 shows the time series of the estimated mean melt contributions to sea level from the Greenland Ice Sheet. We estimate the mean rate of this melt contribution to be 0.20 ± 0.19 mm/yr from 1900 to 2000. This is lower than previous fingerprint-based estimates of 0.6 mm/yr (Mitrovica et al., 2001; Tamisiea et al., 2001). Th difference may arise from the fact that we allow a time dependence in the estimate mean and a spatially variable contribution from ocean thermal expansion. Marzeion et al. (2012) estimated GIS mass change over the period 1901 to 2009 to be 0.20 ± 0.03 mm/yr, using a model-based analysis. In contrast, the IPCC AR4 estimates of Greenland melt of 0.05 ± 0.12 mm/yr from 1961 to 2003 and 0.21 ± 0.04mm/yr from 1993 to 2003 (Bindoff et al., 2007).

Finally, we note that our estimate of the sum of melt contributions from GIS and the glaciers of Baffin and Ellesmere Islands is also 0.20 mm/yr. However, due to negative correlations between estimates of the contributions to sea level from Greenland and Arctic Canada,

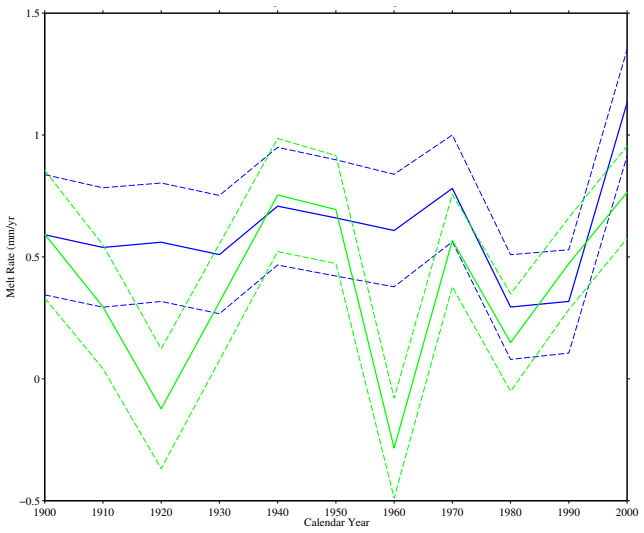

Figure 6.16: Time series of the sum of northern hemisphere (blue) and sum of northern hemisphere (green) melt rate contributions.

the uncertainty in the estimated sum of these contributions is reduced to ±0.12 mm/yr.

Figure 6.16 shows the estimated melt rate contributions to sea level of sources partitioned into two geographic groups, the northern and southern hemisphere. The mean melt rate of the southern hemisphere from 1900 to 2000 is estimated to be 0.4 ± 0.2 mm/yr. The corresponding rate from sources within the northern hemisphere over the same time period is 0.6 ± 0.2 mm/yr. Figure 6.16 indicates that the northern hemisphere estimate is relatively constant until a drop in the rate occurs from 1970 to 1980 followed by a significant rate increase between 1990 and 2000. In contrast, the southern hemisphere contribution is characterized by distinct dips in melt rate, or even ice sheet growth, in 1920, 1960 and 1980.

Figure 6.17 shows estimated time series of the sum of all melt contributions included in this study. The estimated mean rate of land-ice melt contributions to sea level over the 20th century of all melt contributions is 0.99 ± 0.23 mm/yr. As a comparison, the IPCC AR4 estimate total land ice contributions over the period 1961 - 2003 of 0.7 ± 0.2 mm/yr. Our

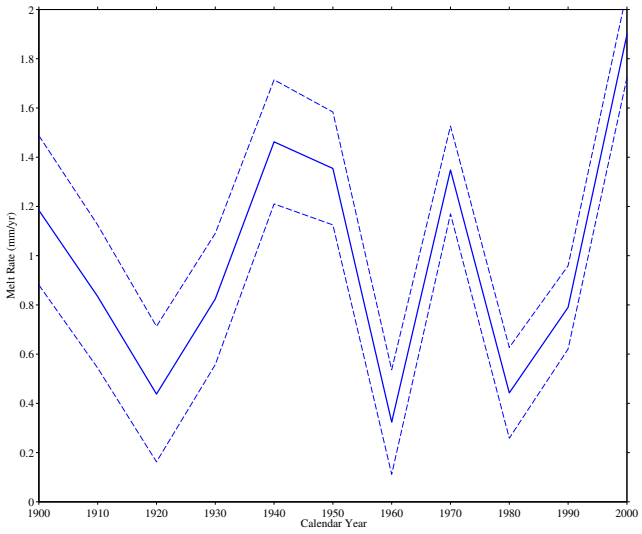

Figure 6.17: Time series of the sum of all melt rate contributions.

estimate for this period is 0.96 ± 0.18 mm/yr.

Figure 6.17 indicates that there was significant variability in the sum of melt contributions over the 20th century. A comparison of Figure 6.17 and Figure 6.16 indicates that most of the temporal variability in the estimate is driven by changes in the melt contributions from the southern hemisphere.

6.3.5 Global Mean Sea Level

Figure 6.18 shows our estimate of the change in global mean sea level (GMSL) over the 20th century. Also included in the figure are the decadal means of GMSL estimates from Church et al. (2011) and Jevrejeva et al. (2008). Our estimated GMSL rate is 1.3 ± 0.2 mm/yr, which is lower than the estimate of 1.7 ± 0.2 mm/yr from 1900 to 2009 by Church et al. (2011).

Both Jevrejeva et al. (2008) and Church et al. (2011) compute the GMSL by averaging subsets of observations or computing the areal average of sea-level change interpolated from

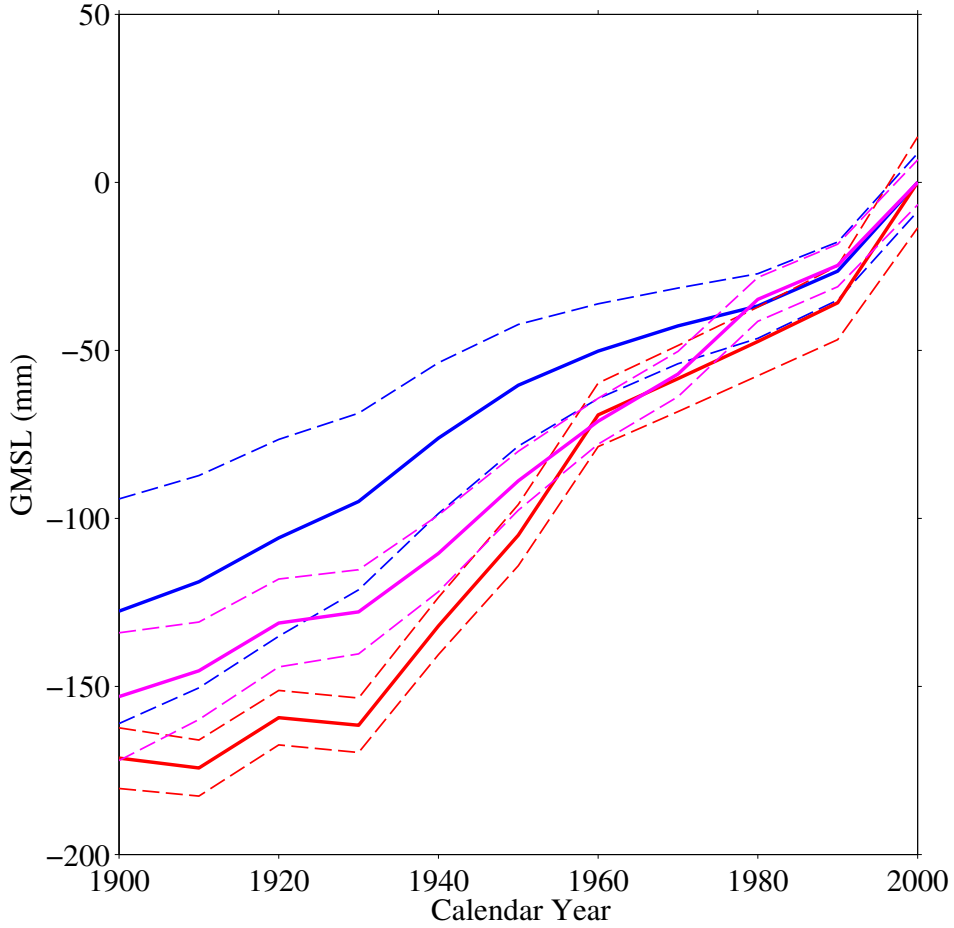

Figure 6.18: Estimate of global mean sea level (GMSL) over the 20th century based on the sum of estimated global melt contributions and the area-weighted average of local contributions including ocean dynamics and non-climatic contributors (blue). Also presented are the decadal means and standard deviations of the Church & White (2011) (magenta) and Jevregeva et al. (2008) (red) GMSL reconstructions.

reconstructions using tide gauges and altimetry observations. However, as we noted in Chapter 2, there is significant geographic variability in sea-level changes. Consequently, the estimation of global trends from analyses that use averages from sparse sampling with tide gauge subsets, or reconstructions that do not account for high-latitude near-field regions of the ice sheets and many glaciers, where sea-level changes due to melt are most significant, may be biased.

To explore the difference between our estimates of GMSL and previous estimates, we first recompute GMSL following the approach of Jevrejeva et al. (2008), though we use the sea level as estimated by the GP regression rather than from the tide gauge records directly. We first interpolate the decadal GP reconstruction results to yearly intervals assuming a linear trend. We then keep only the observations corresponding to those that are available in the PSMSL database. The annual means of regional groups of the available observations as defined by Jevrejeva et al. (2006) are then computed. The GMSL is then computed as the unweighted mean of the regional means. The GMSL computed in this manner from our GP reconstruction is consistent with the annual estimates of Jevrejeva et al. (2008) and Church et al. (2011) (Figure 6.19).

Our GP regression approach makes use of global patterns of sea-level change to infer equivalent eustatic sea-level changes associated with each melting event, or trend associated with modeled patterns of thermostatic-based change. Therefore, even though we are also unable to explicitly observe all regions of sea-level fall, we are able estimate the underlying contributions to produce a truly global estimate of GMSL. The results of Figure 6.18 and Figure 6.19 indicate that the procedures adopted by Jevrejeva et al. (2008), based on regional

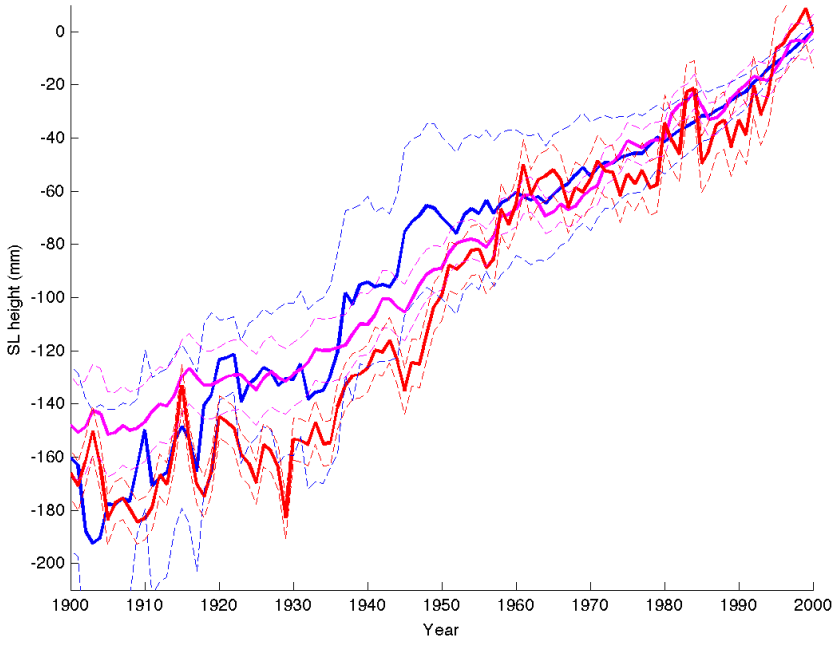

Figure 6.19: Computation of GMSL using the regional averages of GP-estimated sea level at tide gauges for comparison with previous estimates. Also presented are the Church & White (2011) (magenta) and Jevregeva et al. (2012) (red) GMSL reconstructions.

subsets of tide gauge records, introduces bias in the estimate of GMSL in the 20th century.

6.4 Conclusion

To gain understanding of the climate system as it undergoes anthropogenic forced changes, and to be able to estimate future impacts on coastal communities, it is important to understand the mechanisms underlying sea-level changes in the 20th century. We have developed and applied a Gaussian process regression approach to decompose observations of the global sea level field into contributions from ongoing melt, GIA, and local contributions that can include ocean dynamics and non-climatic effects. We find the preferred GIA model corresponds to a lithospheric thickness of 100 km, an upper mantle viscosity of 0.5×10^{21} Pa s and a lower mantle viscosity of 5×10^{21} Pa s which is consistent with a number of independent estimates based on GIA datasets (e.g. Lambeck et al., 1998; Mitrovica and Forte, 2004). The sparsity of observations throughout most of the 20th century limits our ability to uniquely identify individual melt sources but we find that Western Canadian/US glaciers contributed a mean sea level rate of 0.04 ± 0.03 mm/yr from 1900 to 2000, which is in good agreement with previous estimates. Additionally, we find that the GIS contributes a mean sea level rate of 0.20 ± 0.19 mm/yr. Finally, by adding the estimated underlying contributions to sea-level change, rather than computing an areal average of observations or reconstructions, we find a mean GMSL rate over the 20th century of 1.3 ± 0.2 mm/yr, a rate that is $\sim$24% lower than previous estimates.

Chapter 7

Conclusions and future work

The overall goal of this thesis was to refine various estimates of modern and long-term cryospheric mass changes using improved analysis procedures that fully embrace the physics of the controlling processes.

This dissertation has identified an enigma in current estimates of secular changes in the low-degree spherical harmonic figure of Earth's gravitational field over the past 3 million and 25 million years. Current estimates of the degree-2, order-0 component of the geopotential indicate that the mean value of the dynamic ellipticity has remained constant and close to the present-day value throughout the latter part of the Cenozoic. These results appear to justify the standard astronomical tuning of climate records over the same time period. However, an enigma arises in considering the estimates for these two time periods. At time scales of a few million years, the dominant perturbation to the geopotential is the response of the Earth to glacial isostatic adjustment (GIA). Relatively small changes in dynamic ellipticity over this time period imply a very weak mantle that quickly compensates the surface load changes. However, over time periods of tens of millions of years, mantle convection exerts a dominant control on the dynamic ellipticity. In this case, a nearly constant dynamic

ellipticity over this time period implies a high viscosity mantle with sluggish mass transport. These conclusions are clearly contradictory. I proposed four possible resolutions to this enigma: 1) a transient mantle viscosity; 2) changes in tidal dissipation that compensate the GIA and mantle convection signals; 3) estimates of dynamic ellipticity inferences have underestimated the uncertainty; and 4) viscosity models exist for which the perturbations to the dynamic ellipticity from mantle convection and GIA cancel. Clearly, future avenues of research are required to resolve this contradiction, which may lead to further insight into the time dependence of the Earth's rheological structure and the robustness of the age models applied to stratigraphic records.

On modern timescales, the rate of change of the degree-2 zonal component of the geopotential, $\dot{J}_2$, have also been used to infer ice mass changes. However, the $\dot{J}_2$ harmonic is sensitive to other processes such as the 18.6 year tide, mountain glacier mass fluxes, and core-mantle coupling. We have examined, instead, the $\dot{J}_4$ component of the geopotential, which is less sensitive to these processes in order to obtain an independent estimate of net polar ice-mass change over the past two decades. Using two approaches, we estimate a net ice sheet mass flux that is at the upper bound of recent inferences of polar mass flux computed from a comprehensive analysis of regional satellite altimetry, interferometry, and gravimetry data sets.

The spatial pattern, or fingerprint, of sea-level change due to a rapid episode of ice melt is characterized by a significant sea-level fall in the near-field of the ice sheet. Estimates of ice mass loss derived from space-borne gravity instruments, such as GRACE, lack the spatial resolution to sample the ice sheet to the exclusion of portions of the surrounding oceans.

This thesis demonstrates that neglecting the effect of the local water migration can lead to an overestimation of mass changes by up to 9%, though this bias dependent on both the geometry of the melt region, the adopted averaging mask, and the spatial filtering used in the inference. A valuable direction for future work on this topic would be to quantify the magnitude of this bias in other commonly used GRACE-data processing procedures, such as mascon analyses.

I have described an application of Gaussian Process regression to estimate the major sources of sea-level change over the 20th century. While this approach has been used on a regional scale and for forward projections of sea-level change, this is the first application of the methodology to modern inferences of global sea-level change over the 20th century. I estimate the contributions to sea-level from select land-based ice complexes and find general agreement with previous estimates. Furthermore, I compute a new estimate of GMSL of 1.3 ± 0.2 mm/yr which is $\sim$24% smaller than previous estimates and have argued that these earlier analyses were biased by their methodology of grouping and averaging tide gauge records. The GP regression methodology can be improved by considering a more comprehensive characterization of the geometry of processes like GIA, by including, for example, different ice geometries in addition to a suite of rheological models. Moreover, augmenting the observations using data from satellite laser ranging and GPS could help provide tighter and more robust constraints on the contributors to recent GMSL rise and ultimately improve projections of regional and global sea-level changes well into the current century.

Bibliography

Antonov, J., Levitus, S., Boyer, T., 2005. Thermosteric sea level rise, 1955–2003. Geophysical Research Letters 32, 12.

Austermann, J., Mitrovica, J. X., Latychev, K., Milne, G. A., 2013. Barbados-based estimate of ice volume at Last Glacial Maximum affected by subducted plate. Nature Geosci 6 (6), 1–5.

Benjamin, D., Wahr, J., Ray, R. D., Egbert, G. D., Desai, S. D., 2006. Constraints on mantle anelasticity from geodetic observations, and implications for the J_2 anomaly. Geophysical Journal International 165 (1), 3–16.

Berthier, E., Schiefer, E., Clarke, G. K. C., Menounos, B., Rémy, F., 2010. Contribution of Alaskan glaciers to sea-level rise derived from satellite imagery. Nature Geosci 3 (2), 92–95.

Bindoff, N. L., Willebrand, J., Artale, V., Cazenave, A., Gregory, J. M., Gulev, S., Hanawa, K., Le Quere, C., Levitus, S., Nojiri, Y., Shum, C. K., Talley, L., Unnikrishnan, A., 2007. Observations: Oceanic Climate Change and Sea Level. In: Solomon, S., D, Q., Manning, M., Chen, Z., Marquis, M., Averyt, K., Tignor, M., Miller, H. L. (Eds.), Climate Change 2007: The Physical Science Basis. Contribution of Working Group I to the Fourth Assessment Report of the Intergovernmental Panel on Climate Change. Cambridge University Press, Cambridge, UK and NY, USA.

Cazenave, A., Llovel, W., 2010. Contemporary Sea Level Rise. Annual Review of Marine Science 2, 145–173.

Chambat, F., Ricard, Y., Valette, B., 2010. Flattening of the Earth: further from hydrostaticity than previously estimated. Geophysical Journal International 183, 727–732.

Chambers, D. P., Wahr, J., Nerem, R. S., 2004. Preliminary observations of global ocean mass variations with GRACE. Geophysical Research Letters 31 (13), L13310.

Chen, J., Wilson, C., Tapley, B., Blankenship, D., Young, D., 2008. Antarctic regional ice loss rates from GRACE. Earth and Planetary Science Letters 266 (1-2), 140–148.

Cheng, M., Tapley, B., 2004. Variations in the Earth's oblateness during the past 28 years. Journal of Geophysical Research 109 (B9), B09402.

Cheng, M. K., Eanes, R. J., Shum, C. K., Schutz, B. E., Tapley, B. D., 1989. Temporal variations in low degree zonal harmonics from Starlette orbit analysis. Geophysical Research Letters 16 (5), 393–396.

Church, J., White, N. J., 2006. A 20th century acceleration in global sea-level rise. Geophysical Research Letters 33, L01602.

Church, J. A., White, N. J., 2011. Sea-Level Rise from the Late 19th to the Early 21st Century. Surveys in Geophysics 32 (4-5), 585–602.

Church, J. A., White, N. J., Konikow, L. F., Domingues, C. M., Cogley, J. G., Rignot, E., Gregory, J. M., Van Den Broeke, M. R., Monaghan, A. J., Velicogna, I., 2011. Revisiting the Earth's sealevel and energy budgets from 1961 to 2008. Geophysical Research Letters 38 (18).

Clark, J., Farrell, W. E., Peltier, W. R., 1978. Global changes in postglacial sea level: A numerical calculation. Quaternary Research 9, 265–287.

Clark, J., Lingle, C. S., 1977. Future sea-level changes due to West Antarctic ice sheet fluctuations. Nature 269 (5625), 206–209.

Conrad, C. P., Hager, B. H., 1997. Spatial variations in the rate of sea level rise caused by the present-day melting of glaciers and ice sheets. Geophysical Research Letters 24 (12), 1503–1506.

Cox, C. M., Chao, B. F., 2002. Detection of a Large-Scale Mass Redistribution in the Terrestrial System Since 1998. Science 297 (5582), 831–833.

Dalca, A. V., Ferrier, K. L., Mitrovica, J. X., Perron, J. T., Milne, G. A., Creveling, J., 2013. On postglacial sea level–III. Incorporating sediment redistribution. Geophysical Journal International 194 (1), 45–60.

Davis, J. L., Mitrovica, J. X., 1996. Glacial isostatic adjustment and the anomalous tide gauge record of eastern North America. Nature 379 (6563), 331–333.

de Boer, B., van de Wal, R. S. W., Bintanja, R., Lourens, L. J., Tuenter, E., 2010. Cenozoic global ice-volume and temperature simulations with 1-D ice-sheet models forced by benthic δ18O records. Annals of Glaciology 51 (55), 23–33.

Dickey, J. O., Marcus, S. L., de Viron, O., Fukumori, I., 2002. Recent Earth Oblateness Variations: Unraveling Climate and Postglacial Rebound Effects. Science 298 (5600), 1975–1977.

Douglas, B., 1991. Global sea level rise. Journal of Geophysical Research 96, 6981–6992.

Douglas, B., 1997. Global sea rise: a redetermination. Surveys in Geophysics 18, 279–292.

Dziewonski, A. M., Anderson, D. L., 1981. Preliminary reference Earth model. Physics of the Earth and Planetary Interiors 25 (4), 297–356.

Egbert, G. D., Ray, R. D., Bills, B. G., 2004. Numerical modeling of the global semidiurnal tide in the present day and in the last glacial maximum. Journal of Geophysical Research 109, C03003.

Fang, M., Hager, B. H., Herring, T. A., 1996. Surface deformation caused by pressure changes in the fluid core. Geophysical Research Letters 23 (12), 1493–1496.

Fleming, K., Lambeck, K., 2004. Constraints on the Greenland Ice Sheet since the Last Glacial Maximum from sea-level observations and glacial-rebound models. Quaternary Science Reviews 23 (9), 1053–1077.

Forte, A. M., 2007. Constraints on seismic models from other disciplines: implications for mantle dynamics and composition. In: Romanowicz, B., Dziewonski, A. (Eds.), Treatise of Geophysics. Elsevier, Amsterdam, pp. 805–854.

Forte, A. M., Mitrovica, J. X., 1997. A resonance in the Earth's obliquity and precession over the past 20 Myr driven by mantle convection. Nature 390 (6661), 676–680.

Forte, A. M., Quéré, S., Moucha, R., Simmons, N. A., Grand, S. P., Mitrovica, J. X., Rowley, D. B., 2010. Joint seismic–geodynamic-mineral physical modelling of African geodynamics: A reconciliation of deep-mantle convection with surface geophysical constraints. Earth and Planetary Science Letters 295, 329–341.

Gomez, N., Mitrovica, J. X., Tamisiea, M. E., Clark, P. U., 2010. A new projection of sea level change in response to collapse of marine sectors of the Antarctic Ice Sheet. Geophysical Journal International 180 (2), 623–634.

Gregory, J. M., White, N. J., Church, J. A., Bierkens, M. F. P., Box, J. E., van den Broeke, M. R., Cogley, J. G., Fettweis, X., Hanna, E., Huybrechts, P., Konikow, L. F., Leclercq, P. W., Marzeion, B., Oerlemans, J., Tamisiea, M. E., Wada, Y., Wake, L. M., van de Wal, R. S. W., Dec. 2012. Twentieth-Century Global-Mean Sea Level Rise: Is the Whole Greater than the Sum of the Parts? Journal of Climate 26 (13), 121203145300007.

Gurnis, M., 1990. Ridge Spreading, Subduction, and Sea Level Fluctuations. Science 250 (4983), 970–972.

Han, S.-C., Simons, F. J., 2008. Spatiospectral localization of global geopotential fields from the Gravity Recovery and Climate Experiment (GRACE) reveals the coseismic gravity change owing to the 2004 Sumatra-Andaman earthquake. Journal of Geophysical Research 113, B01405.

Hansen, K. S., 1982. Secular effects of oceanic tidal dissipation on the Moon's orbit and the Earth's rotation. Rev. Geophys 20 (3), 457–480.

Hay, C., Morrow, E., Kopp, R., Mitrovica, J. X., 2012. Estimating the sources of global sea level rise with data assimilation techniques. Proceedings of the National Academy of Sciences 110 (S1), 3692–3699.

Hays, J. D., Pitman, W. C., 1973. Lithospheric Plate Motion, Sea Level Changes and Climatic and Ecological Consequences. Nature 246 (5427), 18–22.

Hilgen, F. J., Krijgsman, W., Langereis, C. G., Lourens, L. J., Santarelli, A., Zachariasse, W. J., 1995. Extending the astronomical (polarity) time scale into the Miocene. Earth and Planetary Science Letters 136 (3-4), 495–510.

Hofmann-Wellenhof, B., Moritz, H., 2006. Physical Geodesy, 2nd Edition. Springer-Verlag, Wien.

Holgate, S. J., Matthews, A., Woodworth, P. L., Rickards, L. J., Tamisiea, M. E., Bradshaw, E., Foden, P. R., Gordon, K. M., Jevrejeva, S., Pugh, J., 2013. New Data Systems and Products at the Permanent Service for Mean Sea Level. Journal of Coastal Research 288, 493–504.

Holgate, S. J., Woodworth, P. L., 2004. Evidence for enhanced coastal sea level rise during the 1990s. Geophysical Research Letters 31, L07305.

Hüsing, S. K., Hilgen, F. J., Abdul Aziz, H., Krijgsman, W., 2007. Completing the Neogene geological time scale between 8.5 and 12.5 Ma. Earth and Planetary Science Letters 253 (3-4), 340–358.

Ishii, M., Kimoto, M., 2009. Reevaluation of historical ocean heat content variations with time-varying XBT and MBT depth bias corrections. J Oceanogr 65 (3), 287–299.

Ishii, M., Kimoto, M., Sakamoto, K., Iwasaki, S.-I., 2006. Steric sea level changes estimated from historical ocean subsurface temperature and salinity analyses. J Oceanogr 62 (2), 155–170.

Ivins, E. R., Sammis, C., Yoder, C., 1993. Deep Mantle Viscous Structure with Prior Estimate and Satellite Constraint. J Geophys Res-Sol Ea 98, 4579–4609.

Ivins, E. R., Watkins, M. M., Yuan, D.-N., Dietrich, R., Casassa, G., Rulke, A., 2011. Onland ice loss and glacial isostatic adjustment at the Drake Passage: 2003–2009. Journal of Geophysical Research 116, B02403.

Jacob, T., Wahr, J., Pfeffer, W. T., Swenson, S., 2012. Recent contributions of glaciers and ice caps to sea level rise. Nature 482, 514–518.

James, T. S., Ivins, E. R., 1997. Global geodetic signatures of the Antarctic Ice Sheet. Journal of Geophysical Research 102, 605–633.

Jeans, J. H., 1923. The propagation of earthquake waves. Proceedings of the Royal Society of London. Series A 102 (718), 554–574.

Jevrejeva, S., Grinsted, A., Moore, J. C., Holgate, S. J., 2006. Nonlinear trends and multiyear cycles in sea level records. Journal of Geophysical Research 111, C09012.

Jevrejeva, S., Moore, J. C., Grinsted, A., Woodworth, P. L., 2008. Recent global sea level acceleration started over 200 years ago? Geophysical Research Letters 35 (8), L08715.

Jiang, X., Peltier, W. R., 1996. Ten million year histories of obliquity and precession: The influence of the ice-age cycle. Earth and Planetary Science Letters 139 (1-2), 17–32.

Josberger, E. G., Bidlake, W. R., March, R. S., Kennedy, B. W., 2007. Glacier mass-balance fluctuations in the Pacific Northwest and Alaska, USA. Annals of Glaciology 46 (1), 291–296.

Kaser, G., Cogley, J. G., Dyurgerov, M. B., Meier, M. F., Ohmura, A., 2006. Mass balance of glaciers and ice caps: Consensus estimates for 1961–2004. Geophysical Research Letters 33, L19501.

Kendall, R. A., Latychev, K., Mitrovica, J. X., Davis, J., Tamisiea, M., 2006. Decontaminating tide gauge records for the influence of glacial isostatic adjustment: The potential impact of 3-D Earth structure. Geophysical Research Letters 33 (24), L24318.

Kendall, R. A., Mitrovica, J. X., Milne, G. A., 2005. On post-glacial sea level - II. Numerical formulation and comparative results on spherically symmetric models. Geophysical Journal International 161 (3), 679–706.

Kopp, R. E., 2013. Does the midAtlantic United States sea level acceleration hot spot reflect ocean dynamic variability? Geophysical Research Letters 40, 3981–3985.

Lambeck, K., Smither, C., Johnston, P., 1998. Sea-level change, glacial rebound and mantle viscosity fornorthern Europe. Geophysical Journal International 134 (1), 102–144.

Laskar, J., Joutel, F., Boudin, F., 1993. Orbital, precessional, and insolation quantities for the Earth from -20 Myr to +10 Myr. Astronomy and Astrophysics 270, 522–533.

Laskar, J., Robutel, P., Joutel, F., Gastineau, M., Correia, A., Levrard, B., 2004. A long-term numerical solution for the insolation quantities of the Earth. Astronomy and Astrophysics 428 (1), 261–285.

Latychev, K., Mitrovica, J. X., Tromp, J., Tamisiea, M., Komatitsch, D., Christara, C., 2005. Glacial isostatic adjustment on 3D Earth models: a finitevolume formulation. Geophysical Journal International 161, 421–444.

Levitus, S., Antonov, J. I., Boyer, T. P., Locarnini, R. A., Garcia, H. E., Mishonov, A. V., 2009. Global ocean heat content 1955–2008 in light of recently revealed instrumentation problems. Geophysical Research Letters 36 (7), L07608.

Lisiecki, L., Raymo, M. E., 2005. A Plio-Pleistocene stack of 57 globally distributed benthic δ18O records. Paleoceanography 20, PA1003.

Lithgow-Bertelloni, C., Silver, P. G., 1998. Dynamic topography, plate driving forces and the African superswell. Nature 395, 269–272.

Lombard, A., Cazenave, A., DoMinh, K., Cabanes, C., Nerem, R. S., 2005. Thermosteric sea level rise for the past 50 years; comparison with tide gauges and inference on water mass contribution. Global and Planetary Change 48, 303–312.

Lourens, L., Hilgen, F., Shackleton, N., Laskar, J., Wilson, D., 2004. The Neogene Period. In: Gradstein, F., Ogg, J., Smith, A. (Eds.), A Geologic Time Scale 2004. Cambridge University Press, pp. 409–440.

Lourens, L. J., Wehausen, R., Brumsack, H. J., 2001. Geological constraints on tidal dissipation and dynamical ellipticity of the Earth over the past three million years. Nature 409 (6823), 1029–1033.

Luthcke, S. B., Zwally, H. J., Abdalati, W., Rowlands, D. D., Ray, R. D., Nerem, R. S., Lemoine, F. G., McCarthy, J. J., Chinn, D. S., 2006. Recent Greenland Ice Mass Loss by Drainage System from Satellite Gravity Observations. Science 314 (5803), 1286–1289.

Marcus, S. L., Dickey, J. O., Willis, J. K., Seitz, F., 2009. Earth oblateness changes reveal land ice contribution to interannual sea level variability. Geophysical Research Letters 36, L23608.

Marzeion, B., Jarosch, A. H., Hofer, M., 2012. Past and future sea-level change from the surface mass balance of glaciers. Cryosphere 6 (6), 1295–1322.

Mayo, L. R., March, R. S., 1990. Air temperature and precipitation at Wolverine Glacier, Alaska; Glacier growth in a warmer, wetter climate. Ann. Glaciol 14, 191–194.

Milne, G. A., Mitrovica, J. X., 1998. Postglacial sea-level change on a rotating Earth. Geophysical Journal International 133 (1), 1–19.

Milne, G. A., Mitrovica, J. X., 2008. Searching for eustasy in deglacial sea-level histories. Quaternary Science Reviews 27, 2292–2302.

Mitrovica, J. X., 1996. Haskell [1935] revisited. Journal of Geophysical Research.

Mitrovica, J. X., Beaumont, C., Jarvis, G. T., 1989. Tilting of continental interiors by the dynamical effects of subduction. Tectonics 5, 1079–1094.

Mitrovica, J. X., Davis, J. L., 1995. Presentday postglacial sea level change far from the Late Pleistocene ice sheets: Implications for recent analyses of tide gauge records. Geophysical Research Letters 22 (18), 2529–2532.

Mitrovica, J. X., Forte, A. M., 1995. Pleistocene glaciation and the Earth's precession constant. Geophysical Journal International 121 (1), 21–32.

Mitrovica, J. X., Forte, A. M., 2004. A new inference of mantle viscosity based upon joint inversion of convection and glacial isostatic adjustment data. Earth and Planetary Science Letters 225 (1-2), 177–189.

Mitrovica, J. X., Forte, A. M., Pan, R., 1997. Glaciation-induced variations in the Earth's precession frequency, obliquity and insolation over the last 2.6 Ma. Geophysical Journal International 128 (2), 270–284.

Mitrovica, J. X., Gomez, N., Morrow, E., Hay, C., Latychev, K., Tamisiea, M., 2011. On the robustness of predictions of sea level fingerprints. Geophysical Journal International 187, 729–742.

Mitrovica, J. X., Milne, G. A., 2002. On the origin of late Holocene sea-level highstands within equatorial ocean basins. Quaternary Science Reviews 21, 2179–2190.

Mitrovica, J. X., Pan, R., Forte, A. M., 1994. Late Pleistocene and Holocene ice mass fluctuations and the Earth's precession constant. Earth and Planetary Science Letters 128 (3-4), 489–500.

Mitrovica, J. X., Peltier, W., 1993. Present-day secular variations in the zonal harmonics of Earth's geopotential. Journal of Geophysical Research 98 (B3), 4509–4526.

Mitrovica, J. X., Peltier, W. R., 1991. On Postglacial Geoid Subsidence Over the Equatorial Oceans. J Geophys Res-Sol Ea 96, 20053–20071.

Mitrovica, J. X., Tamisiea, M., Davis, J. L., Milne, G. A., 2001. Recent mass balance of polar ice sheets inferred from patterns of global sea-level change. Nature 409, 1026–1029.

Morrow, E., Mitrovica, J. X., Forte, A. M., Glisović, P., Huybers, P., 2012. An enigma in estimates of the Earth's dynamic ellipticity. Geophysical Journal International, 1129–1134.

Morrow, E., Mitrovica, J. X., Sterenborg, M. G., Harig, C., 2013. A Test of Recent Inferences of Net Polar Ice Mass Balance based on Long-Wavelength Gravity. Journal of Climate 26 (17), 6535–6540.

Moucha, R., Forte, A. M., Mitrovica, J. X., Rowley, D. B., Quéré, S., Simmons, N. A., Grand, S. P., 2008. Dynamic topography and long-term sea-level variations: There is no such thing as a stable continental platform. Earth and Planetary Science Letters 271 (1), 101–108.

Nakada, M., Lambeck, K., 1989. Late Pleistocene and Holocene sealevel change in the Australian region and mantle rheology. Geophysical Journal International 96, 497–517.

Nerem, R., Wahr, J., 2011. Recent changes in the Earth's oblateness driven by Greenland and Antarctic ice mass loss. Geophysical Research Letters 38, L13501.

Pälike, H., Shackleton, N. J., 2000. Constraints on astronomical parameters from the geological record for the last 25 Myr. Earth and Planetary Science Letters 182 (1), 1–14.

Peltier, W., 1974. The impulse response of a Maxwell Earth. Rev. Geophys. Space Phys 12 (4), 649–669.

Peltier, W. R., 2004. Global glacial isostasy and the surface of the ice-age Earth: the ICE-5G (VM2) model and GRACE. Annual Review of Earth and Planetary Sciences 32, 111–149.

Peltier, W. R., Tushingham, A. M., 1989. Global sea level rise and the greenhouse effect: Might they be connected? Science 244, 806–810.

Pelto, M. S., 2006. The current disequilibrium of North Cascade glaciers. Hydrological Processes 20 (4), 769–779.

Plag, H.-P., 2006. Recent relative sea-level trends: an attempt to quantify the forcing factors. Philosophical Transactions of the Royal Society A: Mathematical, Physical and Engineering Sciences 364 (1841), 821–844.

Plag, H.-P., Juttner, H.-U., 2001. Inversion of global tide gauge data for present-day ice load changes. In: Yamanouchi, T. (Ed.), Proceedings of the Second International Symposium on Environmental Resarch in the Arctic and Fifth Ny-Alesund Scientific Seminar. pp. 301–317.

Rasmussen, C. E., Williams, C. K. I., 2006. Gaussian Processes for Machine Learning. MIT Press.

Ricard, Y., Wuming, B., 1991. Inferring the viscosity and the 3-D density structure of the mantle from geoid, topography and plate velocities. Geophysical Journal International 105, 561–571.

Riva, R. E. M., Bamber, J. L., Lavallée, D. A., Wouters, B., 2010. Sea-level fingerprint of continental water and ice mass change from GRACE. Geophysical Research Letters 37, L19605.

Rowlands, D., Luthcke, S., Klosko, S., 2005. Resolving mass flux at high spatial and temporal resolution using GRACE intersatellite measurements. Geophysical Research Letters.

Rowley, D. B., Forte, A. M., Moucha, R., Mitrovica, J. X., Simmons, N. A., Grand, S. P., 2013. Dynamic Topography Change of the Eastern United States Since 3 Million Years Ago. Science 340 (6140), 1560–1563.

Rubincam, D. P., 1984. Postglacial Rebound Observed by Lageos and the Effective Viscosity of the Lower Mantle. Journal of Geophysical Research 89 (B2), 1077–1087.

Sabadini, R., Yuen, D. A., Gasperini, P., 1985. The effects of transient rheology on the interpretation of lower mantle viscosity. Geophysical Research Letters 12 (6), 361–364.

Sabadini, R., Yuen, D. A., Gasperini, P., 1988. Mantle rheology and satellite signatures from present-day glacial forcings. Journal of Geophysical Research 93 (B1), 437.

Shackleton, N. J., Berger, A., Peltier, W. R., 1990. An alternative astronomical calibration of the lower Pleistocene timescale based on ODP Site 677. Transactions of the Royal Society of Edinburgh: Earth Sciences 81, 251–251.

Shackleton, N. J., Crowhurst, S., Weedon, G., Laskar, J., 1999. Astronomical calibration of Oligocene-Miocene time. Philosophical Transactions: Mathematical, Physical and Engineering Sciences 357 (1757), 1907–1929.

Shepherd, A., Ivins, E. R., A, G., Barletta, V. R., Bentley, M. J., Bettadpur, S., Briggs, K. H., Bromwich, D. H., Forsberg, R., Galin, N., Horwath, M., Jacobs, S., Joughin, I., King, M., Lenaerts, J. T. M., Li, J., Ligtenberg, S. R. M., Luckman, A., Luthcke, S. B., McMillan, M., Meister, R., Milne, G. A., Mouginot, J., Muir, A., Nicolas, J. P., Paden, J., Payne, A. J., Pritchard, H., Rignot, E., Rott, H., Sørensen, L. S., Scambos, T. A., Scheuchl, B., Schrama, E. J. O., Smith, B., Sundal, A. V., van Angelen, J. H., van de Berg, W. J., van den Broeke, M. R., Vaughan, D. G., Velicogna, I., Wahr, J., Whitehouse, P. L., Wingham, D. J., Yi, D., Young, D., Zwally, H. J., 2012. A Reconciled Estimate of Ice-Sheet Mass Balance. Science 338 (6111), 1183–1189.

Simmons, N. A., Forte, A. M., Grand, S. P., 2009. Joint seismic, geodynamic and mineral physical constraints on threedimensional mantle heterogeneity: Implications for the relative importance of thermal versus compositional heterogeneity. Geophysical Journal International 177 (3), 1284–1304.

Simons, F. J., Dahlen, F. A., 2006. Spherical Slepian functions and the polar gap in geodesy. Geophysical Journal International 166, 1039–1061.

Spasojevic, S., Gurnis, M., 2012. Sea level and vertical motion of continents from dynamic earth models since the Late Cretaceous. Bulletin 96 (11), 2037–2064.

Steinberger, B., Calderwood, A. R., 2006. Models of large-scale viscous flow in the Earth's mantle with constraints from mineral physics and surface observations. Geophysical Journal International 167 (3), 1461–1481.

Sterenborg, M. G., Morrow, E., Mitrovica, J. X., 2013. Bias in GRACE estimates of ice mass change due to accompanying sea-level change. Journal of Geodesy 87, 387–392.

Swenson, S., Wahr, J., 2002. Methods for inferring regional surface-mass anomalies from Gravity Recovery and Climate Experiment (GRACE) measurements of time-variable gravity. Journal of Geophysical Research 107 (B9), 2193.

Swenson, S., Wahr, J., 2006. Post-processing removal of correlated errors in GRACE data. Geophysical Research Letters 33, L08402.

Tamisiea, M., Hill, E., Ponte, R., Davis, J. L., Velicogna, I., Vinogradova, N., 2010. Impact of self-attraction and loading on the annual cycle in sea level. J. geophys. Res 115, C07004.

Tamisiea, M., Mitrovica, J. X., Davis, J. L., 2007. GRACE gravity data constrain ancient ice geometries and continental dynamics over Laurentia. Science 316, 881–883.

Tamisiea, M. E., Mitrovica, J. X., Milne, G. A., Davis, J. L., 2001. Global geoid and sea level changes due to present-day ice mass fluctuations. Journal of Geophysical Research 106 (B12), 30849–30,863.

Tapley, B., Bettadpur, S., Ries, J. C., Thompson, P., Watkins, M., 2004. GRACE measurements of mass variability in the Earth system. Science 305 (5683), 503–505.

Taylor, K. E., Stouffer, R. J., Meehl, G. A., 2012. An Overview of CMIP5 and the Experiment Design. Bulletin of the American Meteorological Society 93 (4), 485–498.

Trupin, A. S., Panfili, R. P., 1997. Mass balance of polar ice from long wavelength features of the Earth's gravitational field. Surveys in Geophysics 18 (2/3), 313–326.

van Andel, T. J., 1994. New Views on an Old Planet: A History of Global Change, 2nd Edition. Cambridge University Press, New York.

Velicogna, I., Wahr, J., 2006a. Acceleration of Greenland ice mass loss in spring 2004. Nature 443 (7109), 329–331.

Velicogna, I., Wahr, J., 2006b. Measurements of Time-Variable Gravity Show Mass Loss in Antarctica. Science 311 (5768), 1754–1756.

Wahr, J., Swenson, S., Velicogna, I., 2006. Accuracy of GRACE mass estimates. Geophysical Research Letters 33, L06401.

Wahr, J., Swenson, S., Zlotnicki, V., Velicogna, I., 2004. Time-variable gravity from GRACE: First results. Geophysical Research Letters 31, L11501.

Whitehouse, P. L., Bentley, M. J., Milne, G. A., King, M., Thomas, I. D., 2012. A new glacial isostatic adjustment model for Antarctica: calibrated and tested using observations of relative sealevel change and presentday uplift rates. Geophysical Journal International 190, 1464–1482.

Woodward, R., 1888. On the form of position of mean sea level. US Geological Survey Bulletin 48, 87–170.

Woodworth, P. L., Tsimplis, M. N., Flather, R. A., Shennan, I., 1999. A review of the trends observed in British Isles mean sea level data measured by tide gauges. Geophysical Journal International 136 (3), 651–670.

Yoder, C., Williams, J., Dickey, J., Schutz, B., Eanes, R., Tapley, B., 1983. Secular variation of Earth's gravitational harmonic J_2 coefficient from Lageos and nontidal acceleration of Earth rotation. Nature 303 (5920), 757–762.